doi.org/10.26434/chemrxiv.9101405.v1

Mechanistic Insights into Fe Catalyzed α-C-H Oxidations of Tertiary Amines

Christopher J. Legacy, Frederick T. Greenaway, Marion Emmert

Submitted date: 28/07/2019 • Posted date: 29/07/2019

Citation information: Legacy, Christopher J.; Greenaway, Frederick T.; Emmert, Marion (2019): Mechanistic Insights into Fe Catalyzed α-C-H Oxidations of Tertiary Amines. ChemRxiv. Preprint.

We report detailed mechanistic investigations of an iron-based catalyst system, which allows the α-C-H oxidation of a wide variety of amines, including acyclic tertiary aliphatic amines, to afford dealkylated or amide products. In contrast to other catalysts that affect α-C-H oxidations of tertiary amines, the system under investigation employs exclusively peroxy esters as oxidants. More common oxidants (e.g. tBuOOH) previously reported to affect amine oxidations via free radical pathways do not provide amine α-C-H oxidation products in combination with the herein described catalyst system. Motivated by this difference in reactivity to more common free radical systems, the investigations described herein employ initial rate kinetics, kinetic profiling, Eyring studies, kinetic isotope effect studies, Hammett studies, ligand coordination studies, and EPR studies to shed light on the Fe catalyst system. The obtained data suggest that the catalytic mechanism proceeds through C-H abstraction at a coordinated substrate molecule. This rate-determining step occurs either at an Fe(IV) oxo pathway or a 2-electron pathway at a Fe(II) intermediate with bound oxidant. We further show via kinetic profiling and EPR studies that catalyst activation follows a radical pathway, which is initiated by hydrolysis of PhCO3 tBu to tBuOOH in the reaction mixture. Overall, the obtained mechanistic data support a non-classical, Fe catalyzed pathway that requires substrate binding, thus inducing selectivity for α-C-H functionalization.

File list (3)

Mechanistic Insights into Fe Catalyzed α-C-H Oxidations of Tertiary Amines

Christopher J. Legacy,[a] Frederick T. Greenaway,[b] Marion H. Emmert[a,c]*

[a]Department of Chemistry and Biochemistry, Worcester Polytechnic Institute, 100 Institute Road, Worcester, MA 01609, USA

[b]EPR studies. Gustaf H. Carlson School of Chemistry, Clark University, 950 Main Street, Worcester, MA 01610, USA

[c]Current Address: Department of Process Research & Development, Discovery Process Chemistry, MRL, Merck & Co., Inc., 770 Sumneytown Pike, West Point, PA 19486, USA

ABSTRACT: We report detailed mechanistic investigations of an iron-based catalyst system, which allows the α-C-H oxidation of a wide variety of amines, including acyclic tertiary aliphatic amines, to afford dealkylated or amide products. In contrast to other catalysts that affect α-C-H oxidations of tertiary amines, the system under investigation employs exclusively peroxy esters as oxidants. More common oxidants (e.g. ^{t}BuOOH) previously reported to affect amine oxidations via free radical pathways do not provide amine α-C-H oxidation products in combination with the herein described catalyst system. Motivated by this difference in reactivity to more common free radical systems, the investigations described herein employ initial rate kinetics, kinetic profiling, Eyring studies, kinetic isotope effect studies, Hammett studies, ligand coordination studies, and EPR studies to shed light on the Fe catalyst system. The obtained data suggest that the catalytic mechanism proceeds through C-H abstraction at a coordinated substrate molecule. This rate-determining step occurs either at an Fe(IV) oxo pathway or a 2-electron pathway at a Fe(II) intermediate with bound oxidant. We further show via kinetic profiling and EPR studies that catalyst activation follows a radical pathway, which is initiated by hydrolysis of $PhCO_3{}^tBu$ to ^{t}BuOOH in the reaction mixture. Overall, the obtained mechanistic data support a non-classical, Fe catalyzed pathway that requires substrate binding, thus inducing selectivity for α-C-H functionalization.

Introduction

C-H oxidations of organic molecules frequently occur in biosynthetic pathways[1] as well as in drug metabolism.[2] Many of these reactions are catalyzed by enzymes bearing Fe cofactors. Examples are the cytochrome P_{450} family exhibiting Fe-porphyrin cofactors[2-4] or non-heme dioxygenases, hydroxylases, and halogenases.[5] The majority of these systems catalyze oxidations via Fe(IV) oxo intermediates, which attack aliphatic C-H bonds of a substrate in a radical rebound fashion, cleaving the C-H bond via a hydrogen abstraction mechanism.[5,2,6-9] For enzyme-catalyzed amine α-C-H oxidations, an alternative mechanistic possibility to Fe oxo pathways has been proposed, based on model compound studies.[10] This mechanism proceeds through single electron and proton transfers, forming iminium or imine products via radical intermediates.

The mechanistic framework of *synthetic* systems that functionally mimic the metabolic pathways of amine α-C-H oxidations in combination with O_2, H_2O_2, or ^{t}BuOOH as oxidants have long been under discussion, with proposed pathways proceeding via free or solvent-caged radicals, hemiaminals, peroxyhemiaminals, and/or metal-coordinated iminium ions.[11-18] Recently, a seminal publication by Doyle and coworkers has shown that the majority of the catalysts employing ^{t}BuOOH as oxidant likely promote oxidations via free radical pathways and hemiaminal intermediates, regardless of the used metal catalyst.[19] This study was performed with aniline-type substrates and the investigated catalysts included both precious metal systems ($Rh_2(cap)_4$, $RuCl_3$) and base-metal catalysts (CuBr, $FeCl_3$, $Co(OAc)_2$). Importantly, the presence of O_2 influenced the kinetic isotope effects observed, suggesting that reaction pathways may differ depending on the used oxidant. Unfortunately, the question of whether the mechanistic insights reported by Doyle and coworkers are transferrable to α-C-H functionalizations of *aliphatic* amines has not been resolved yet, as many catalysts active in aniline α-C-H oxidations are unreactive towards tertiary aliphatic amines.[20]

Motivated by the absence of such mechanistic information regarding the α-C-H oxidations of aliphatic amines, we set out to establish mechanistic hypotheses supported by experimental data for a Fe-based catalyst system previously developed in our lab (see Scheme 1).

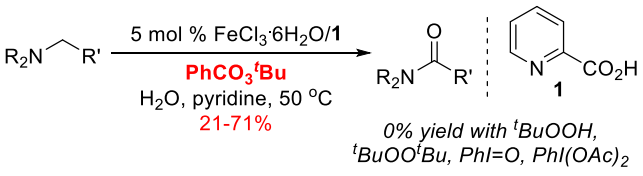

Scheme 1. Optimized Conditions for Fe Catalyzed α-C-H oxidation of Tertiary Aliphatic Amines.

This reaction affects oxidations of aromatic *and* aliphatic amines and is selective for α-C-H functionalizations of amines, even in complex molecule settings such as active pharmaceutical ingredients.[20] Surprisingly, many common oxidants

previously used in Fe oxidation catalysis do not affect this reaction, with the exception of peroxyesters that afford between 21% and 71% yield. Yields are strongly dependent on the steric bulk of the amine substrate. In contrast to other protocols proceeding via free radical pathways,[21] the established reaction conditions are selective for oxidation of C-H bonds of *acyclic* substrates, while cyclic α-C-H bonds are not attacked

Based on the studies detailed in this manuscript, we propose that α-C-H cleavage proceeds through a radical rebound or concerted mechanism instead of a free radical mechanism often proposed with simple Fe catalysts such as in Fenton-type chemistries.[22] Interestingly, the experimental values for Eyring parameters and kinetic isotope effect (KIE) are more akin to values typically observed with ß-hydride elimination (formal hydride shift) and concerted metalation deprotonation (involvement of a heteroatom of the oxidant). Such two-electron processes are most often invoked for C-H cleavage processes in precious metal catalysts (e.g. Pd, Ir[23,24]). This mechanistic proposal provides insight into the need for peroxyester oxidants, the role of each reaction component under the empirically established optimal catalytic conditions, and the sources of side products observed in the reaction mixture. Overall, the mechanistic pathway provides a rationale for the selectivity of amine α-C-H oxidation with the established Fe catalyst system.

Results and Discussion

A. General Mechanistic Framework for Fe Catalyzed Amine to Amide Conversion. Our laboratory has previously[20] reported several key mechanistic features of the Fe catalyzed α-C-H oxidation of amines (see Scheme 2: (1) The concentration of H_2O had been found to be crucial for high conversion, with loadings of less than 5 equiv. and more than 15 equiv. significantly reducing amide yields. (2) In reactions with large amounts of H_2O added, the major side product is dealkylated amine **4**; lowering the oxidant ($PhCO_3{}^tBu$) loading leads to formation of up to 64% of **4**. Furthermore, aldehyde side products can be observed. (3) Reactions performed in the presence of $H_2{}^{18}O$ as additive revealed that the oxygen atom incorporated in the amide product stems from H_2O (and not O_2 or $PhCO_3{}^tBu$). (4) Experiments performed in the presence of KCN led to α-C-H cyanation instead of α-C-H oxygenation, suggesting that iminium compounds **3** are potential intermediates or side products in the reaction pathway.

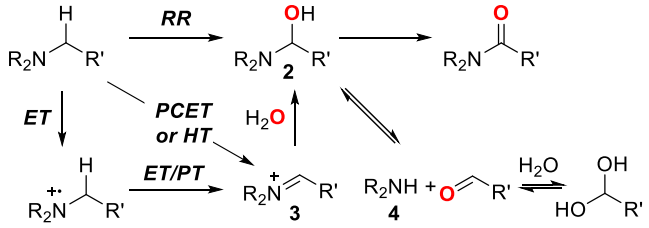

Scheme 2. General Reaction Framework. RR = radical rebound; PCET = proton-coupled electron transfer; HT = hydride transfer; ET = electron transfer; PT = proton transfer.

(5) Finally, reacting $HNPr_2$ and EtCHO under analogous reaction conditions to amine α-C-H oxidation conditions also resulted in formation of the corresponding amide.Collectively, these findings supported the proposal of a mechanistic framework for amine α-C-H oxidation as formulated in Scheme 2 in analogy to aniline oxidation pathways affected by Fe-heme compounds.[10]

In the proposed mechanistic pathway, the initial C-H bond cleavage may proceed through a radical rebound mechanism (RR, Scheme 2, top), providing direct access to hemiaminal **2**. Alternatively, a proton-coupled electron transfer (PCET) or hydride transfer (HT; Scheme 2, middle) or a sequence of electron and proton transfers (ET/PT, bottom) may form the iminium intermediate **3**, which in turn is attacked by H_2O to provide hemiaminal **2**. In the presence of large amounts of H_2O in the reaction solution, dealkylation of amine substrate to afford **4** is likely driven by formation of the aldehyde hydrate; alternatively, a second α-C-H oxidation of hemiaminal **2** would result in formation of the amide product. These preliminary mechanistic investigations did not provide any insight into the first, most crucial part of amine α-C-H oxygenation: the process of α-C-H bond breaking and the role of the catalyst in this process. As such, our subsequent studies aimed to elucidate this question.

B. Initial Rate Kinetics. We first sought to establish an experimental kinetic rate law, using the method of initial rates. We reasoned that this approach would provide a suitable framework for further mechanistic studies, eventually leading to rational optimization of the amine α-C-H oxidation protocol and new catalyst developments. Due to the paramagnetic properties of the Fe catalyst used in amine α-C-H oxidation, the use of NMR techniques to follow the kinetic profile of the reactions was deemed unsuitable. Instead, *in-situ* FTIR was employed and the disappearing C=O band of the oxidant ($PhCO_3{}^tBu$) was observed to provide well-characterized kinetic profiles.

We first explored the role of the added ligand **1** for catalysis. To this end, the oxidant $PhCO_3{}^tBu$ was added to pyridine as solvent and an *in-situ* FTIR signal was established. This signal (represented by the green line in Scheme 3) showed initially a curve without any slope, signifying the absence of reactivity. Next, substrate (NPr_3), H_2O, and $FeCl_3{\cdot}6H_2O$ were sequentially added into the mixture. With each addition, the IR signal for $PhCO_3{}^tBu$ decreased due to dilution, but remained flat, indicative of a constant concentration of the oxidant.

Finally, 2-picolinic acid (**1**) was added to the mixture, resulting in kinetic traces with increasing/decreasing slopes (green: $PhCO_3{}^tBu$; blue: reaction product $PhCO_2H$; Scheme 3). Overall, these data suggest that ligand **1** is necessary for catalytic turnover and that α-C-H oxidation does not occur in its absence. Importantly, the form of the kinetic traces characterizes a catalytic reaction with an initiation period. Therefore, all initial rate studies discussed below measured the maximum reaction rate (maximum slope) of the kinetic curve.

Initiation of the catalytic reaction by addition of **1** as detailed above further suggests that the empirically optimized ratio of Fe/**1** (1:1)[20] should also correspond to the highest observed reaction rate, if only one molecule of **1** is bound in Fe in the catalytically active species. This hypothesis was tested by measuring the initial rate with varying amounts of ligand **1** (2.5 to 10 mol %; Scheme 4). As expected, the highest initial rate was observed at a Fe/**1** ratio of 1:1, while higher and lower ratios resulted in decreased initial rates. This demonstrates that the conditions providing the highest yields are also the kinetically fastest conditions, suggesting that the active catalyst does not change throughout the course of the reaction.

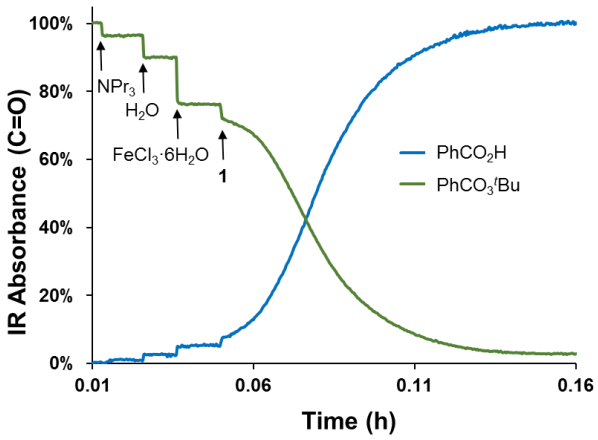

Scheme 3. *In-situ* FTIR Reaction Profiles of Oxidant ($PhCO_3{}^tBu$) and Reaction Product ($PhCO_2H$) Demonstrating Importance of Ligand 1 for Catalysis. Conditions: 50 °C, pyridine (50 eq.), NPr_3 (1 eq.), H_2O (9 eq.), $FeCl_3{\cdot}6H_2O$ (5.0 mol %), 1 (5.0 mol %), $PhCO_3{}^tBu$ (3 eq.).

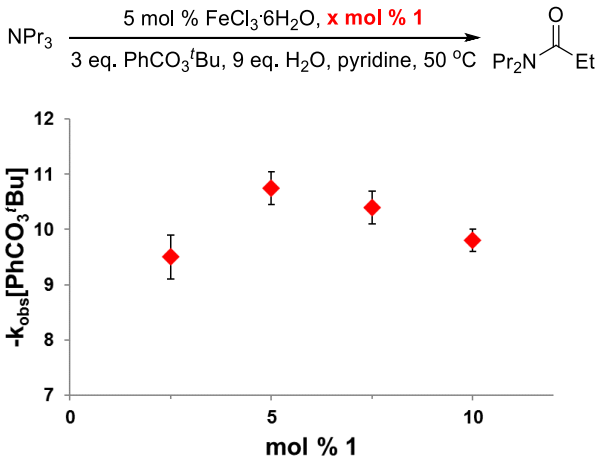

Scheme 4. Dependence of Initial Rate on Ligand (1) Loading at Fe Loading of 5.0 mol %.

Next, we explored the influence of X-type ligands. We reasoned that the presence of these ligands can be expected to influence catalytic activity, if they remain coordinated to the Fe center. To examine this question, we measured the initial rates of the reaction with a series of Fe(III) [$Fe(OTf)_3$, $FeCl_3$, $Fe(NO_3)_3$, $Fe_2(SO_4)_3$, $Fe(acac)_3$] under otherwise unchanged conditions. Scheme 5 shows a plot of the resulting initial rates plotted versus the pK_a of the corresponding acid of the X-type ligands. Notably, the initial rates do not change significantly, implying that X-type ligands are not coordinated to the Fe center in the catalytically active species.

We then turned our attention to establishing the kinetic orders of the different components of the catalytic system; the respective data are shown in Schemes 5 to 8. At low (catalytically relevant) concentrations of Fe/**1** (<5 mol %), a nearly linear relationship was observed, suggesting that the reaction is first order in [Fe/**1**] under these conditions. Towards higher catalyst loadings, the measured initial rates go through a maximum. This implies that off-cycle Fe species exist that are favored under these conditions. Such off-cycle species may be polymeric or dimeric $[Fe/\mathbf{1}]_n$ compounds, similar to compounds that have previously been characterized in analogous Fe/**1** mixtures.[18] Kinetic orders in [$PhCO_3{}^tBu$] and [NPr_3] were determined in an analogous fashion. In both cases, the observed rates showed a first-order dependence, as characterized by a linear increase of rate with substrate or oxidant concentrations (see Schemes 7 and 8). At higher (not catalytically relevant) $PhCO_3{}^tBu$ and NPr_3 loadings, saturation kinetics are observed (see SI).

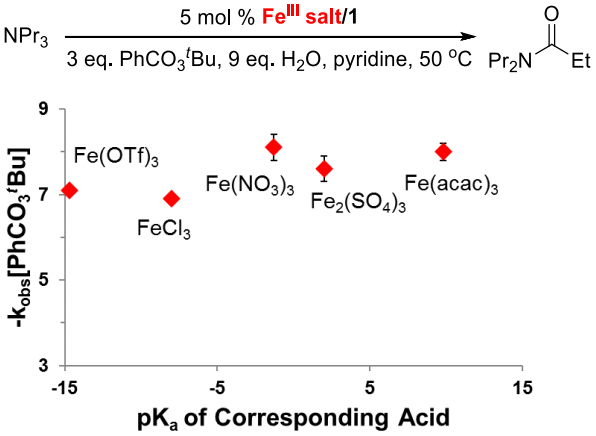

Scheme 5. Dependence of Initial Rate on X-Type Ligand.

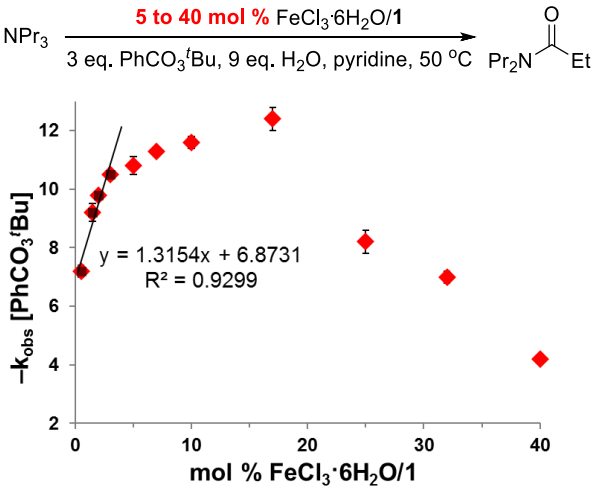

Scheme 6. Initial Rate Versus Catalyst Loading.

We then investigated if C-H bond cleavage may be occurring in the rds (Scheme 9) by independently measuring the initial rates of oxidation with NEt_3 and NEt_3-D_{15} as substrates. The obtained ratio $\mathbf{k_H/k_D}$ was determined to be 1.7 ± 0.1, indicative of a primary kinetic isotope effect and consistent with rate-determining C-H cleavage. Interestingly, similar values of KIEs have been observed for rate-determining ß-hydride elimination by Ru catalysts.[25] Furthermore, similar ranges of isotope effects have been observed in reactions between Pd complexes and benzene/C_6D_6, which have been proposed to bind benzene before C-H cleavage.[26] Comparing these values is consistent with a mechanism in which the amine substrate binds to the Fe catalyst before C-H scission.

Next, the kinetic orders in [H_2O] and [pyridine] were determined; both components of the reaction system have empirically been shown to be crucial for reactivity (Schemes 10 and

11).[20] Interestingly, a negative 2nd order dependence on the H_2O loading is observed at low [H_2O] and saturation kinetics are observed at higher [H_2O]. Furthermore, a 0th order dependence on [pyridine] was observed, seemingly contradictory to the experimental observation that the absence of pyridine results in very low (EtOAc solvent) or no reactivity (all other tested solvents).

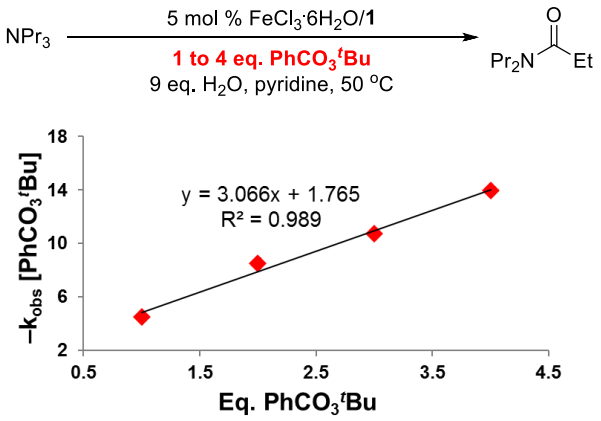

Scheme 7. Initial Rate Versus Oxidant Loading.

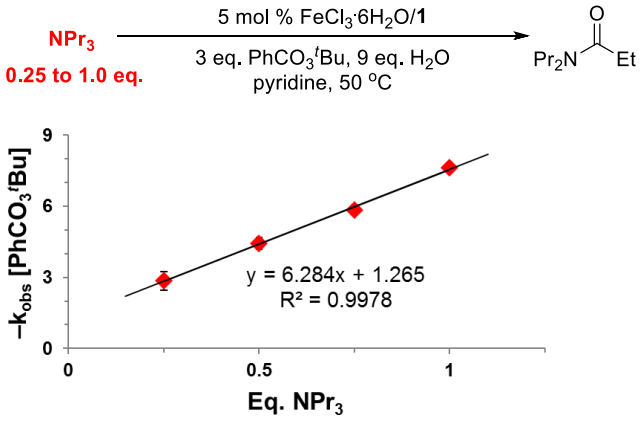

Scheme 8. Initial Rate Versus Amine Substrate Loading.

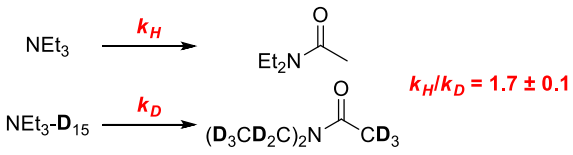

Scheme 9. Kinetic Isotope Effect Study: Initial Rate for NEt_3 and NEt_3-D_{15}. Conditions: 50 °C, pyridine (50 eq.), NEt_3 or NEt_3-D_{15} (1 eq.), H_2O (9 eq.), $FeCl_3$·$6H_2O$ (5.0 mol %), **1** (5.0 mol %), $PhCO_3{}^tBu$ (3 eq.).

Therefore, we hypothesized that the number of coordinated pyridine ligands on Fe does not change between the resting state and the transition state structure, which is in agreement with a 0th order dependence on [pyridine]. To test this hypothesis, we performed the reaction in different substituted pyridines as solvents (50 eq. each), reasoning that coordination of pyridine-type ligands to Fe should result in a significant influence of the ligand electronics on the catalytic rate. Such a dependence was indeed observed (Scheme 12). Interestingly, both electron-withdrawing and electron-donating substituents on pyridine result in slower initial reaction rates that pyridine, indicating a change in rds for pyridines with electron-withdrawing and electron-donating substituents.

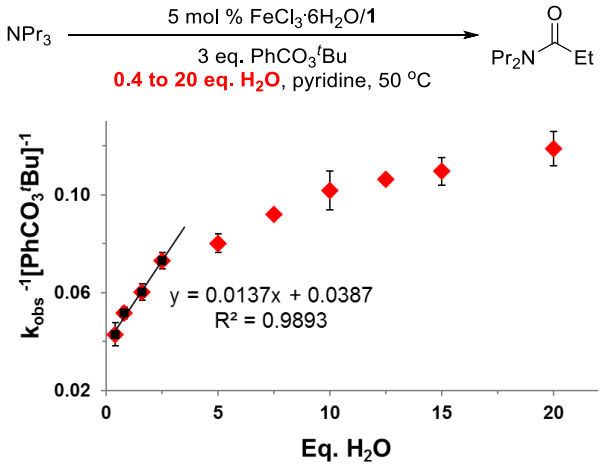

Scheme 10. Inverse Negative Initial Rate Versus H_2O Loading.

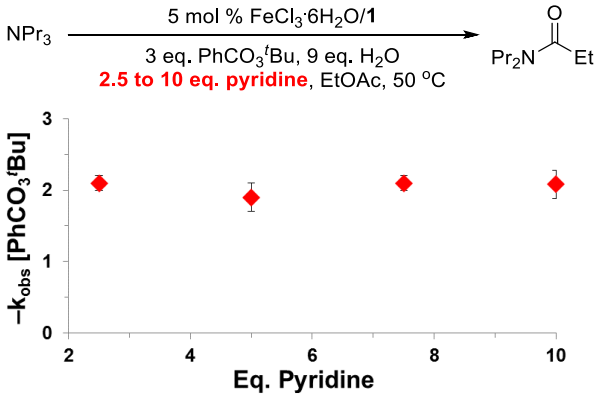

Scheme 11. Initial Rate Versus Pyridine Loading. Conditions: Conditions: 50 °C, EtOAc (50 eq.), NPr_3 (1 eq.), H_2O (9 eq.), $FeCl_3$·$6H_2O$ (5.0 mol %), **1** (5.0 mol %), $PhCO_3{}^tBu$ (3 eq.), pyridine (2.5 to 10 eq.).

Finally, we aimed to document the kinetic orders for $PhCO_2H$ and $PhCO_2^-$, as $PhCO_2H$ is a product of the reaction, which may react with the substrate in an acid-base reaction, and thus influence reaction rates. Indeed, plotting the initial rates obtained with different loadings of $PhCO_2H$ showed a negative 1st order dependence of the rate on [$PhCO_2H$] (Scheme 13). However, all attempts to introduce $PhCO_2^-$ to the reaction resulted in the precipitation of alkali benzoates in solution or a rapid, non-catalyzed background reaction (NBu_4PhCO_2) with the oxidant. Both conditions prevent the acquisition of valid kinetic data.

C. Further Insight into the Rate-Determining Step: Eyring Study and Oxidant Model Substrate. To further investigate the nature of the rds, the initial rate of the reaction was measured as a function of temperature (Scheme 14) and Eyring analysis was performed to determine the activation parameters

($\Delta H^{\ddagger}$ = 14.1 kcal/mol; $\Delta S^{\ddagger}$ = -10.8 cal K^{-1} mol^{-1}; for details, see the SI). The obtained value for the activation entropy $\Delta S^{\ddagger}$ is in agreement with a highly ordered transition state structure and is similar to values observed in concerted C-H bond cleavage processes.[27,28]

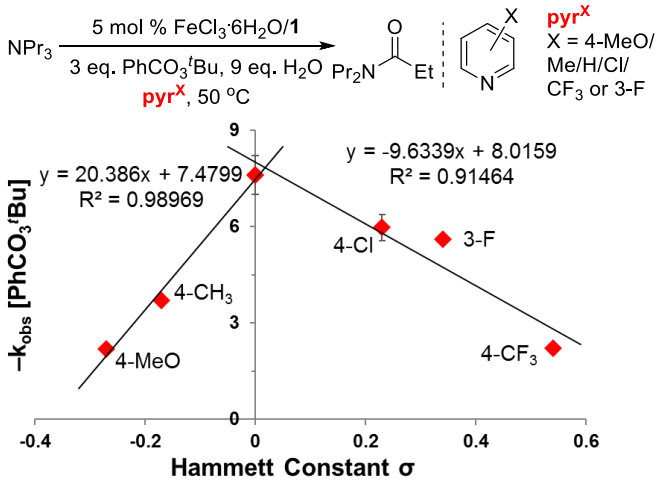

Scheme 12. Hammett Studies with Different Pyridines as Solvent.

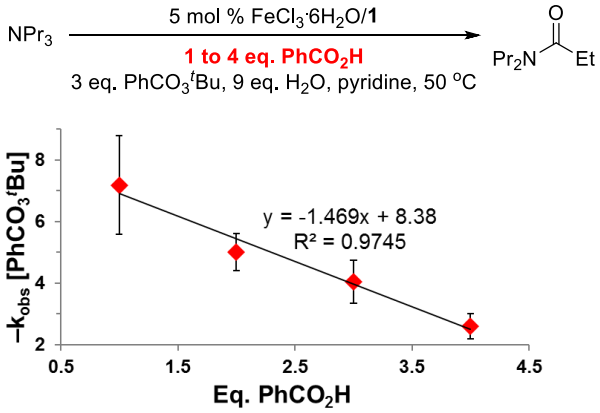

Scheme 13. Initial Rate Versus $PhCO_2H$ Loading

Furthermore, both activation parameters are in a similar range as activation parameters measured for rate-determining H atom transfer from substrates with weak C-H bonds to an Fe-oxo model compound ($\Delta H^{\ddagger}$ = 12.7 kcal/mol; $\Delta S^{\ddagger}$ = -9 cal K^{-1} mol^{-1}), albeit in combination with a significantly larger kinetic isotope effect (KIE = 5.7 for xanthene/9,10-d_2-xanthene).[29] Generally, many metal-oxo initiated C-H bond abstractions similar to cytochrome P_{450} (radical rebound) mechanisms show similar negative values for the activation entropy.[27,30] In contrast, homolytic O-O bond cleavage of peroxyesters[31] or reactions proceeding via dissociation of substrate from the metal catalyst prior to C-H bond cleavage[32] are typically associated with more positive activation entropies, corresponding to a less ordered transition state structure.

To probe the nature of oxidant participation in amine α-C-H oxidation, a modified peroxyester **6** (Scheme 15) was employed as oxidant. **6** and related compounds are known to allow differentiation between pathways that undergo homolytic and heterolytic O-O bond cleavage.[33-36] As outlined in Scheme 15, homolytic cleavage of the O-O bond would result in formation of acetone and a benzylic radical; interestingly, acetone was found only as a minor product (7%).

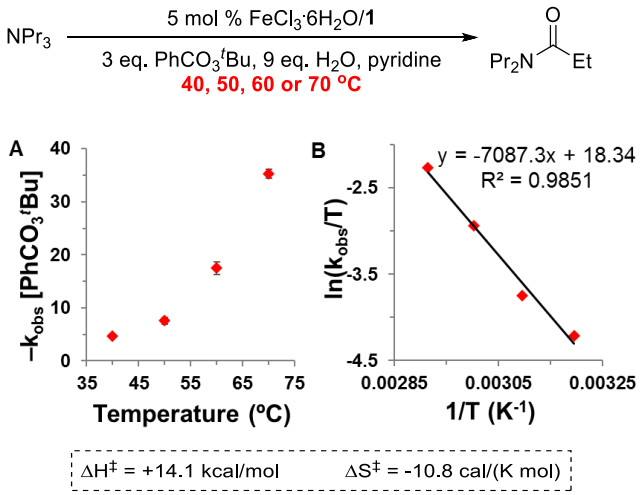

Scheme 14. Eyring Study and Resulting Thermodynamic Activation Parameters.

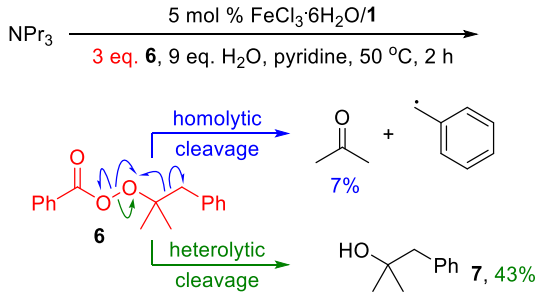

Scheme 15. Oxidation of NPr_3 with Oxidant Model Substrate. Conditions: $FeCl_3·6H_2O$ (5.0 mol %), **1** (5.0 mol %), pyridine (2 mL), H_2O (9.0 eq.), **6** (3.0 eq.), NPr_3 (1.0 eq.); yields obtained after 75% conversion of **6**. No amide product was obtained, but products of dealkylation were observed in the reaction mixture.

The major product, alcohol **7**, was obtained in 43% yield, suggesting that heterolytic O-O bond cleavage is the major reaction pathway under the established reaction conditions. This is particularly interesting, as heterolytic cleavage of the O-O bond suggests a two electron or metal-oxo pathway, which stands in contrast to free radical pathways often proposed and documented for simple Fe catalysts in the presence of other peroxy oxidants.[17,37-39]

D. Coordination Studies. To provide more insight into the resting state structure and allow future design of more reactive and selective catalyst structures, we initiated coordination studies geared towards establishing the ligand environment around the Fe catalyst precursor.

First, we sought to confirm pyridine binding (as suggested by the Hammett studies) to the Fe center. This was achieved by titrating aliquots of a solution of $FeCl_3·6H_2O$ into an aqueous solution containing pyridine. The FTIR signal representing free,

non-coordinated pyridine proportionally diminished with the addition of the first two aliquots, and then disappeared with the addition of a third aliquot (Scheme 16). This result, supported by data obtained via ESI-MS analysis (see SI), indicates a pyridine: Fe binding stoichiometry of 3:1. Interestingly, the FTIR bands representing coordinated pyridine (light green spectrum labeled 1.0-1.5 eq. Fe; Scheme 16B) are very broad in comparison to the non-coordinated pyridine signals, possibly showcasing the fluxional nature of ligand coordination.

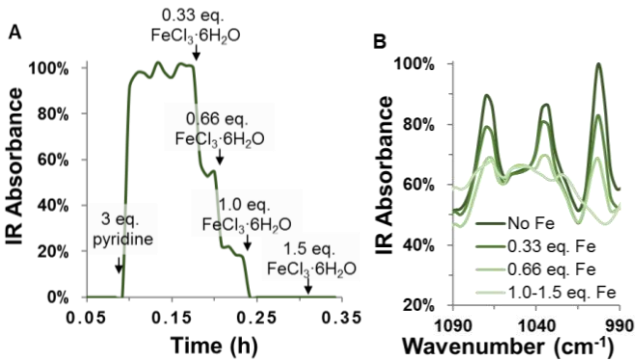

Scheme 16. (A) *In-situ* FTIR Analysis Result of Titration of $FeCl_3·6H_2O$ into Aqueous Pyridine Solution. (B) Corresponding *in-situ* FTIR Spectra.

We next investigated binding of picolinic acid (**1**) to Fe. When aliquots corresponding to 0.5 eq. of **1** were sequentially added to a solution of 1.0 eq. $FeCl_3·6H_2O$ in pyridine (Scheme 17A), *in situ* FTIR analysis showed binding with a maximum stoichiometry of 2:1 (**1**:Fe); addition of higher amounts of **1** led to the observation of a signal for non-coordinated ligand **1** (yellow trace in Scheme 17). Notably, two distinct spectra for Fe complexes of **1** were observed prior to detection of non-coordinated **1**. Both spectra are characterized by the shift of the C=O signal from 1730 cm^{-1} (free ligand **1**) to 1690 cm^{-1}. The first spectrum (orange trace in Scheme 17) occurs exclusively at low concentrations of **1** and constitutes the major species in solution until 1.5 eq. of **1** and disappears in the presence of 2.0 eq. of **1**. This implies that the first spectrum (orange trace) corresponds to a Fe complex [Fe(**1**)L_n] with only one molecule of **1** coordinated to the metal center. The second spectrum (purple trace in Scheme 17) characterizes a complex [Fe(**1**)$_2L_n$] with two molecules of **1** as ligands. These data establish that the majority of Fe is present as [Fe(**1**)L_n] at the catalytically relevant 1:1 ratio of $FeCl_3·6H_2O$ and **1**.

Finally, oxidant, substrate, and product binding to [Fe(**1**)L_n] were investigated. Interestingly, no significant binding to [Fe(**1**)L_n] was observed for $PhCO_3{}^tBu$ and *N*,*N*-dipropyl propenamide (see SI for details). In contrast, NPr_3 binding to [Fe(**1**)L_n] was clearly observed, as shown in Scheme 18. Upon addition of up to 1 eq. NPr_3 to a solution of [Fe(**1**)L_n] in pyridine, a new species was detected, characterized by a C=O band at 1680 cm^{-1} and several peaks in the fingerprint region of the FTIR spectrum (1320 to 950 cm^{-1}, green trace in Scheme 18). This complex converts to a second species (red trace) upon addition of more NPr_3; however, the first complex can still be detected until addition of 3.0 eq. of NPr_3 is completed. The second complex (red trace) exhibits FTIR bands in the fingerprint region that are similar to the first species but shows characteristic new bands at 1660 and 1350 cm^{-1} (Scheme 18B). Further addition of NPr_3 beyond 3.0 eq. does not result in detection of another species with distinct FTIR signals.

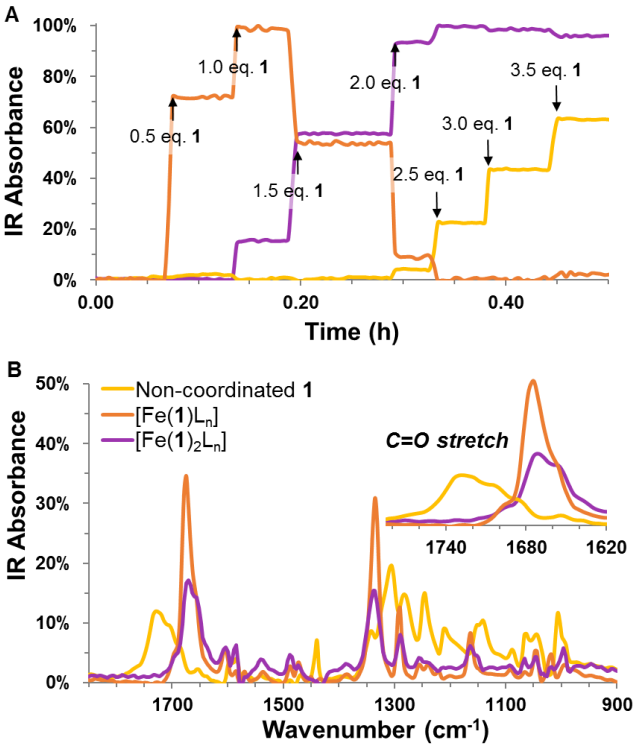

Scheme 17. (A) Titration of 1 into $FeCl_3·6H_2O$ in pyridine. (B) Comparison of observed FTIR spectra representing different [Fe(1)$_n$L$_m$] species and free picolinic acid (1). Color coding relates the disappearance and appearance of different spectra throughout the titration experiment.

Due to the stoichiometry required to form each species, we propose that the first signal (green trace) corresponds to a complex [Fe(**1**)(NPr_3)L_n], while the second (red) trace characterizes [Fe(**1**)(NPr_3)$_2L_n$] with two amine substrates as ligands. We therefore propose that up to 2 eq. of NPr_3 can coordinate to Fe under catalytic conditions, which are characterized by a 20-fold excess of substrate to Fe catalyst. Interestingly, the data shown in Scheme 18A imply different binding constants for the first and second equivalent of amine: The maximum amount of [Fe(**1**)(NPr_3)L_n] is observed with only 1 eq. of NPr_3 added, while addition of 2 more equivalents of NPr_3 is required to completely convert [Fe(**1**)(NPr_3)L_n] to [Fe(**1**)(NPr_3)$_2L_n$].

E. Investigation of Catalyst Initiation via Reaction Progress Kinetic Analysis. One feature of the kinetic profiles observed in all kinetic studies discussed above is a notable initiation period. Literature precedent[40] suggests generally two mechanistic causes for an initiation period: (i) Promotion of catalysis by reaction products or (ii) an initial, non-catalyzed reaction, which assembles the catalytically active species.

To test if the reaction at hand is promoted by its products, a kinetic trace obtained under standard conditions (black trace in Scheme 19) was compared to kinetic traces observed upon addition of 5 mol % of different reaction products ($Pr_2NC(=O)Et$, $HNPr_2$, ^tBuOH, $PhCO_2H$; amine dealkylation products such as $HNPr_2$ are typically observed in trace amounts in all tested

reactions[20]). No significant effect on either the maximum rate or the length of the initiation period was observed, as shown by the near overlap of the corresponding kinetic traces in Scheme 19. This suggests that reaction products do not promote catalysis.

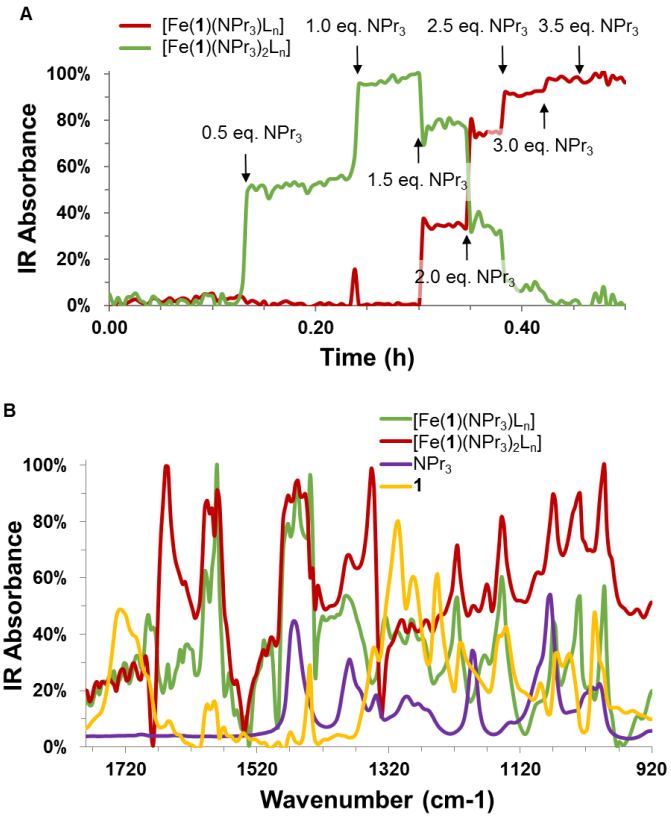

Scheme 18. (A) Titration of NPr_3 into solution of $[Fe(1)L_n]$ in pyridine. (B) Comparison of FTIR Spectra of Formed Fe Complexes, non-coordinated NPr_3, and non-coordinated 1.

Having ruled out the possibility of self-promotion by reaction products, we then sought to gain insight into potential off-cycle reactivity that may lead to assembly of the catalytically active species. We hypothesized that different concentrations of reagents that take part in the non-catalyzed initiation reaction should result in differing initiation period lengths. Therefore, we postulated that comparing reaction profiles obtained at different concentrations of reagents would identify reagents involved in catalyst activation. To this end, kinetic reaction profiles obtained at different reagent and catalyst concentrations were plotted as reaction rate vs. time and conversion vs. time plots (Schemes 20 to 23). This analysis shows that initiation periods are shortened at *higher* [oxidant] and [substrate] and at *lower* [H_2O] and [$PhCO_2H$]. These observations suggest that these four reagents are involved in the initiation (or catalyst activation) reaction.

In contrast, no clear trend was observed with different loadings of Fe/**1** (see SI), implying that the Fe catalyst concentration has no significant influence on the rate of the initiation reaction. This is in agreement with the previously stated postulate that the initiation reaction is a non-catalyzed reaction aiding in assembly of the catalytically active species.

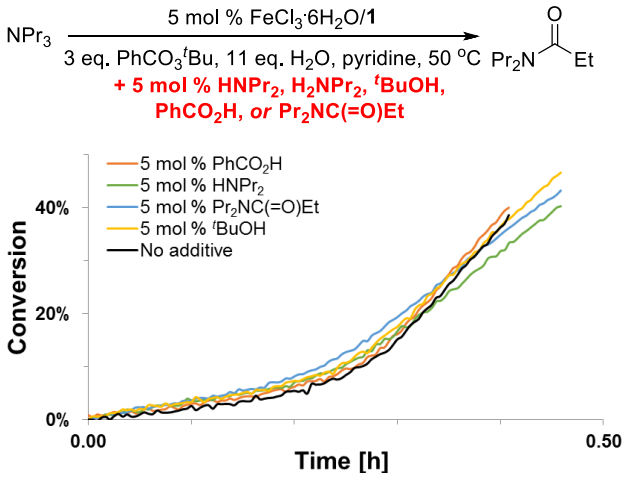

Scheme 19. Effect of Product Addition on Length of Initiation Period.

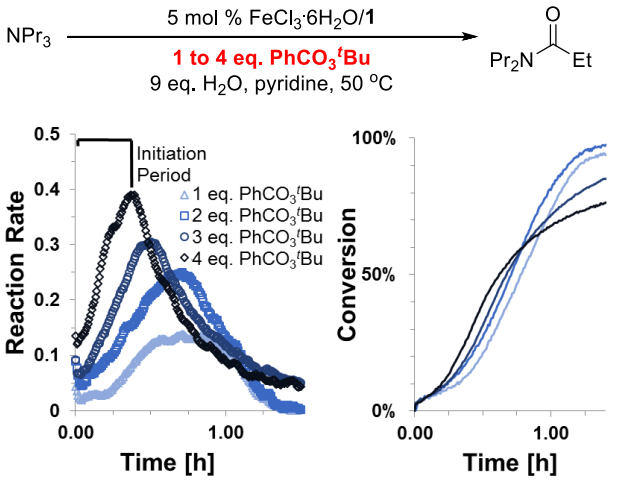

Scheme 20. Effect of Oxidant Loading on Length of Initiation Period.

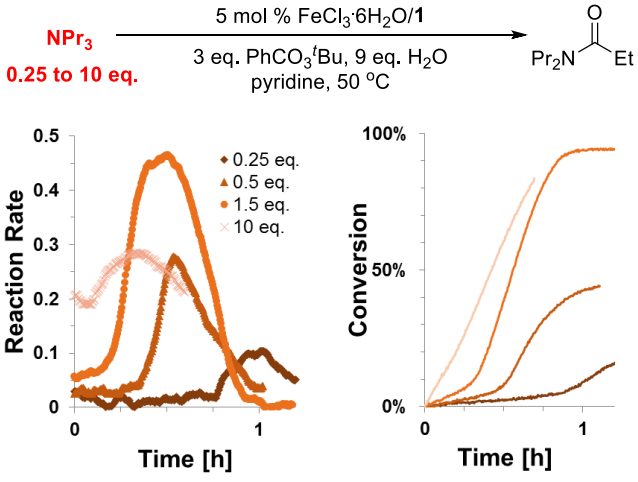

Scheme 21. Effect of Amine Substrate Loading on Length of Initiation Period.

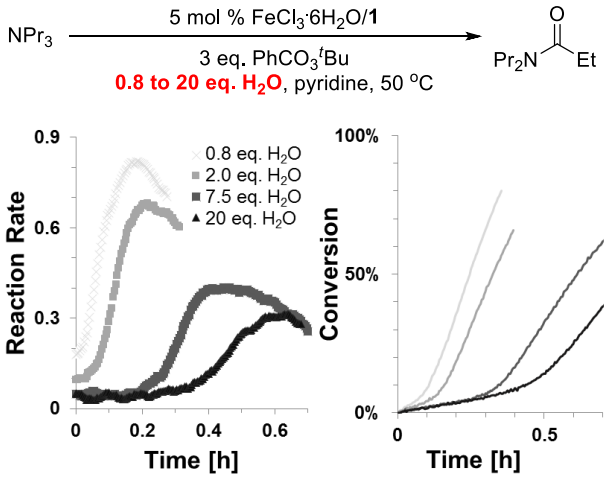

Scheme 22. Effect of H_2O Loading on Length of Initiation Period.

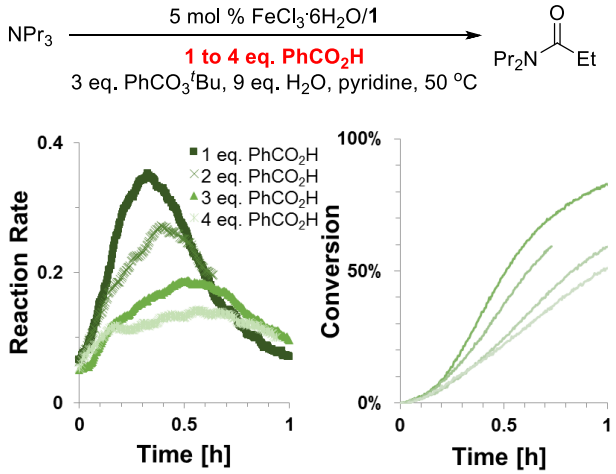

Scheme 23. Effect of $PhCO_2H$ Loading on Length of Initiation Period.

Based on these data, we hypothesized that hydrolysis of the peroxyester $PhCO_3{}^tBu$ to form $PhCO_2^-$ and ^{t}BuOOH is the non-catalyzed reaction occurring during the initiation period (Scheme 24). ^{t}BuOOH can go on to form ^{t}BuO· radicals in the presence of pyridine, as previously described in the literature,[41-43] thereby forming at least small amounts of bipyridines (**11**). This is consistent with the observation of small amounts of **11** by GCMS analysis in all amine α-C-H oxidation reactions (see SI).

To further test the hypothesis of catalyst activation by reaction between ^{t}BuOOH formed via hydrolysis and the Fe(III) catalyst precursor, we added 5 mol % of ^{t}BuOOH to the reaction mixture before adding amine substrate. Gratifyingly, the kinetic trace obtained completely lacked an initiation period and the reaction initiated with a maximum rate (see Scheme 25). This suggests that formation of ^{t}BuOOH via hydrolysis of the oxidant $PhCO_3{}^tBu$ is indeed responsible for the initiation reaction. A proposed pathway how ^{t}BuOOH may lead to catalyst initiation is discussed vide infra.

F. EPR Studies. To gain insight into the presence of radical species and possible oxidation states of Fe in the reaction mixture, EPR studies were performed (for complete details, see the SI). EPR studies at room temperature were designed to elucidate the proposed presence of radicals in the reaction mixture. In these studies, no radicals were observed in the absence of added $FeCl_3$, either via direct observation or in the presence of the spin trap phenyl-*tert*-butylnitrone.

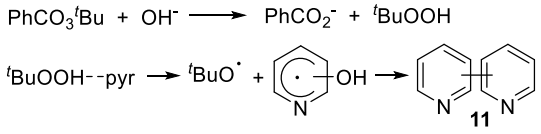

Scheme 24. Proposed Reaction Leading to Catalyst Activation via Formation of ^{t}BuOOH and Side Reactivity of ^{t}BuOOH.

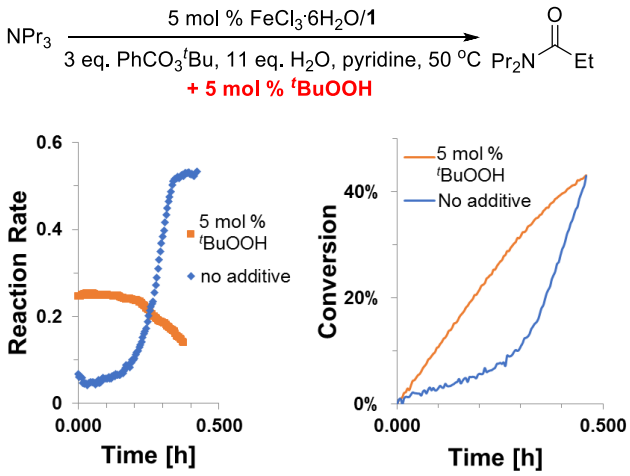

Scheme 25. Effect of ^{t}BuOOH Addition on Length of Initiation Period.

In a mixture of $FeCl_3$, **1**, pyridine, and water (mimicking the catalytic reaction mixture), addition of either ^{t}BuOOH or $PhCO_3{}^tBu$ resulted in formation of O-centered radicals, but in different amounts and selectivity (Scheme 26A). With ^{t}BuOOH, the major radical detected was ^{t}BuOO•, while only small amounts of ^{t}BuO• were detected upon addition of $PhCO_3{}^tBu$. This suggests that ^{t}BuOO• may be the product of the catalyst activation pathway. Furthermore, the data imply that small amounts of $PhCO_3{}^tBu$ can undergo homolytic O-O bond scission in the presence of Fe(III), even though the majority of turnover in C-H oxidation stems from heterolytic O-O bond cleavage, as evidenced by the oxidant model study described further above.

EPR studies to elucidate the spin state of the Fe center were performed of solutions frozen in liquid nitrogen immediately after preparation. EPR clearly shows the binding of ligand **1** upon addition of **1** to a $FeCl_3$ solution in pyridine/H_2O, with a new high-spin signal (S = 5/2). Addition of NPr_3 to this solution resulted in a low-spin Fe species (S = 1/2) with a very broad signal at g = 2. Both of these findings are in agreement with ligand binding to Fe(III) as proposed by FTIR titration (see above). Interestingly, when $PhCO_3{}^tBu$ is added to the resulting mixture, no EPR signal is observed, suggesting the formation of an EPR silent species as the resting state of the reaction.

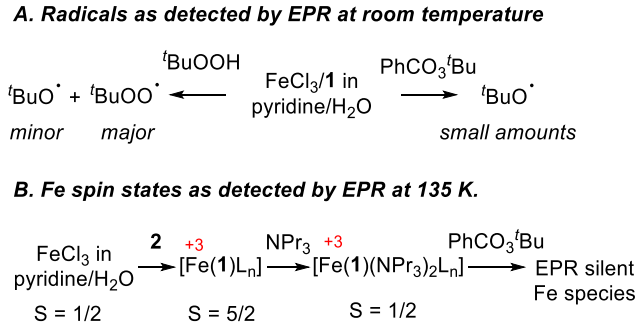

Scheme 26. Summary of Results from EPR Studies.

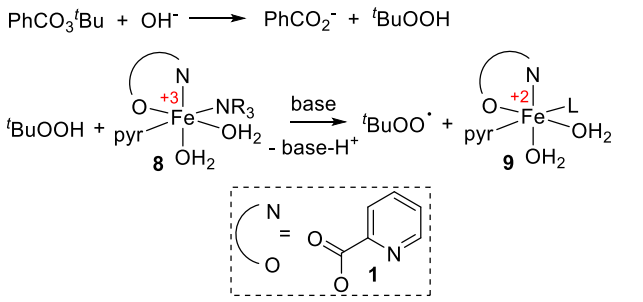

Scheme 27. Catalyst Activation and Proposed Resting State Structure 9.

G. Discussion of Mechanistic Proposals Based on Experimental Data. Based on the experimental mechanistic data obtained, we propose (i) a mechanistic pathway for catalyst activation and (ii) two catalytic cycles for catalyst turnover.

First, catalyst activation is clearly achieved by the interaction of the Fe(III) catalyst precursor **8** and ^{t}BuOOH. As evidenced by EPR studies, the formation of tBuOO• likely occurs in this reaction, suggesting a reduction from Fe(III) to Fe(II) in a reaction step precedented in Fenton chemistry.[22] In combination with the ligand coordination studies, this leads to a proposed resting state structure **9** as shown in Scheme 27.

Based on this resting state structure, two different catalytic cycles (Scheme 28A/B) can be proposed that fulfill the empirical rate law (Scheme 28C), the requirement for heterolytic O-O bond cleavage, ^{18}O labeling being introduced to the product from ^{18}O-labeled water,[20] and C-H bond scission in the rds. Both catalytic cycles (A and B) start with similar resting states **9** and **9a**, with the only difference being one molecule of water being associated with the resting state in mechanism B. Due to the catalytic relevance of ligand **1**, we propose that it remains coordinated to Fe throughout the complete catalytic cycle. Coordination of pyridine, two H_2O ligands, and one molecule of a spectator ligand complete the resting state structures. Due to the significantly lower reaction rates at high [Fe/**1**], we propose that each resting state is in equilibrium with an off-cycle, oligomeric or polymeric species $[Fe(\mathbf{1})L_x]_n$. The key difference between mechanisms A and B lies in (i) the Fe species affecting the C-H scission and (ii) oxidation state changes throughout the catalytic cycle.

Mechanism A is characterized by a series of coordination/dissociation steps between resting state **9** and rds, with the rds proceeding through a hybrid between β-hydride elimination and concerted metalation/deprotonation. The oxidant O-O bond is cleaved in the rds concurrently with the C-H bond, while the oxidant also acts as an internal base to aid in β-hydride elimination of the amine, resulting in an iminium salt as product. During the complete cycle A, Fe remains in the oxidation state +2.

Mechanism B also proceeds through a series of coordination/dissociation steps between the resting state **9a** and the rds, in addition to a two electron-oxidation of Fe(+2) to Fe(+4). This oxidation proceeds upon heterolytic O-O bond cleavage of $PhCO_3{}^t$Bu, in agreement with the model oxidant studies discussed above. The rds in mechanism B is formulated analogous to typical radical-rebound mechanisms at Fe-oxo species, consisting of a homolytic C-H bond cleavage at Fe(+4) intermediate **13**, followed by a fast rebound step to directly produce the bound hemiaminal intermediate.

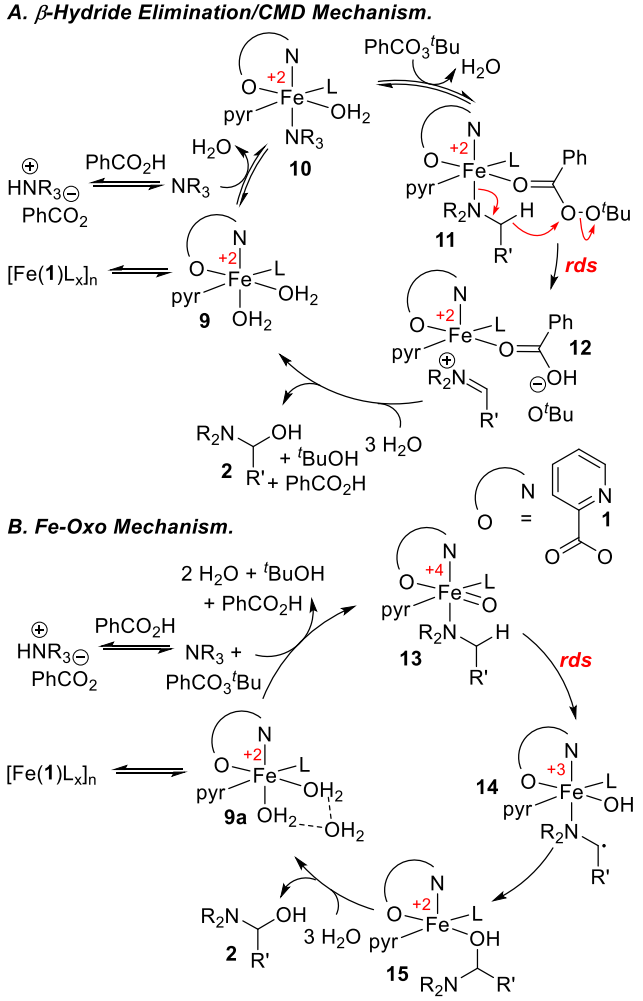

Scheme 28. Proposed Catalytic Cycles Based on Experimental Mechanistic Studies.

Summary and Conclusions

Overall, the results of the mechanistic studies can be graphically summarized in detailed proposed mechanisms as shown in Scheme 28. Several general conclusions can be drawn from the two proposed mechanisms: (1) Both pyridine and ligand **1** do not dissociate from the catalytically active species throughout both cycles. This suggests a path forward in the journey

towards more efficient catalysts (and away from pyridine in solvent-quantities): The design of a ligand in which **1** is covalently associated with a pyridine moiety. (2) Kinetic profiling and EPR studies allowed the proposal of ^{t}BuOO· as the reagent providing access to the catalytically active species **9**. This suggests that one-electron reduction is required to access the catalytically active species, which in turn might simply be achieved by the use of Fe(+2) catalyst precursor species. (3) The two presented mechanisms consistent with the experimental data do not suggest a role for free radicals in the reaction mechanism outside of the catalyst activation pathway. This fundamentally distinguishes the investigated catalyst system from the systems investigated previously by Doyle and coworkers.[19] The presented work further provides an explanation for why α-C-H oxidation of a wide variety of tertiary aliphatic amines is possible: coordination to Fe activated the substrate to undergo C-H cleavage. In contrast, previous systems proceeding through free radical mechanisms are restricted to more activated substrates (secondary amines, benzylic/aniline-type substrates). (4) Remaining questions regarding the mechanism (e.g. distinguishing between the two proposed mechanisms; the specifics of oxidant/Fe interactions; or the source of the catalyst system's unique selectivity for acyclic amines) will likely require further in-depth spectroscopic and DFT studies.

ASSOCIATED CONTENT

Supporting Information. Detailed procedures for kinetic and coordination studies, examples of kinetic traces, ESI-MS and GCMS analyses. This material is available free of charge via the Internet at http://pubs.acs.org.

AUTHOR INFORMATION

Corresponding Author

* mhemmert@wpi.edu; marion.emmert@merck.com

Author Contributions

The manuscript was written through contributions of all authors. All authors have given approval to the final version of the manuscript.

ACKNOWLEDGMENT

We thankfully acknowledge R. Grimm (WPI) for assistance with ESI-MS measurements, D. Hebrault and M. Burns (both Mettler-Toledo) for assistance with acquiring *in-situ* FTIR analyses, and M. Frenette (UQAM) for helpful discussions. We acknowledge Worcester Polytechnic Institute for financial support of this work.

REFERENCES

(1) Chen, K.; Baran, P. S., *Nature* **2009,** *459*, 824-828.

(2) Genovino, J.; Sames, D.; Hamann, L. G.; Touré, B. B., *Angew. Chem. Int. Ed.* **2016,** *55*, 14218-14238.

(3) Oscarson, M., *Drug Metab. Dispos.* **2001,** *29*, 91-95.

(4) Walsh, A. A.; Szklarz, G. D.; Scott, E. E., *J. Biol. Chem.* **2013,** *288*, 12932-12943.

(5) Nam, W., *Acc. Chem. Res.* **2007,** *40*, 522-531.

(6) Schlichting, I.; Berendzen, J.; Chu, K.; Stock, A. M.; Maves, S. A.; Benson, D. E.; Sweet, R. M.; Ringe, D.; Petsko, G. A.; Sligar, S. G., *Science* **2000,** *287*, 1615-1622.

(7) Chen, K.; Que, L., *J. Am. Chem. Soc.* **2001,** *123*, 6327-6337.

(8) Groves, J. T., *Nature Chem.* **2014,** *6*, 89-91.

(9) Huang, X.; Groves, J. T., *J. Biol. Inorg. Chem.* **2017,** *22*, 185-207.

(10) Chiavarino, B.; Cipollini, R.; Crestoni, M. E.; Fornarini, S.; Lanucara, F.; Lapi, A., *J. Am. Chem. Soc.* **2008,** *130*, 3208-3217.

(11) Li, Z.; Bohle, D. S.; Li, C.-J., *Proc. Natl. Acad. Sci.* **2006,** *103*, 8928-8933.

(12) Catino, A. J.; Nichols, J. M.; Nettles, B. J.; Doyle, M. P., *J. Am. Chem. Soc.* **2006,** *128*, 5648-5649.

(13) Boess, E.; Schmitz, C.; Klussmann, M., *J. Am. Chem. Soc.* **2012,** *134*, 5317-5325.

(14) Boivin, J.; Gaudin, D.; Labrecque, D.; Jankowski, K., *Tetrahedron Lett.* **1990,** *31*, 2281-2282.

(15) Barton, D. H. R.; Boivin, J.; Gaudin, D.; Jankowski, K., *Tetrahedron Lett.* **1989,** *30*, 1381-1382.

(16) Barton, D. H. R.; Doller, D., *Acc. Chem. Res.* **1992,** *25*, 504-512.

(17) Perkins, M. J., *Chem. Soc. Rev.* **1996,** *25* (4), 229-236.

(18) Kiani, S.; Tapper, A.; Staples, R. J.; Stavropoulos, P., *J. Am. Chem. Soc.* **2000,** *122*, 7503-7517.

(19) Ratnikov, M. O.; Doyle, M. P., *J. Am. Chem. Soc.* **2013,** *135*, 1549-1557.

(20) Legacy, C. J.; Wang, A.; O'Day, B. J.; Emmert, M. H., *Angew. Chem. Int. Ed.* **2015,** *54*, 14907-14910.

(21) Yilmaz, O.; Oderinde, M. S.; Emmert, M. H., *J. Org. Chem.* **2018**, *83*, 11089-11100.

(22) (a) Sawyer, D. T.; Sobkowiak, A.; Matsushita, T., *Acc. Chem Res.* **1996,** *29*, 409-416; (b) MacFaul, P. A.; Wayner, D. D. M.; Ingold, K. U., *Acc. Chem. Res.* **1998,** *31*, 159-162; Goldstein, S.; Meyerstein, D., *Acc. Chem. Res.* **1999,** *32*, 547-550.

(23) Davies, D. L.; Donald, S. M.; Macgregor, S. A., *J. Am. Chem. Soc.* **2005,** *127*, 13754-13755.

(24) Boutadla, Y.; Davies, D. L.; Macgregor, S. A.; Poblador-Bahamonde, A. I., *Dalton Trans.* **2009**, 5820-5831.

(25) Thalen, L. K.; Zhao, D.; Sortais, J. B.; Paetzold, J.; Hoben, C.; Backvall, J. E., *Chem. Eur. J.* **2009,** *15*, 3403-3410.

(26) Zhong, H. A.; Labinger, J. A.; Bercaw, J. E., *J. Am. Chem. Soc.* **2002,** *124*, 1378-1399.

(27) Gardner, K.; Mayer, J., *Science* **1995,** *269*, 1849-1851.

(28) Roiban, G. D.; Serrano, E.; Soler, T.; Aullon, G.; Grosu, I.; Cativiela, C.; Martinez, M.; Urriolabeitia, E. P., *Inorg. Chem.* **2011,** *50*, 8132-8143.

(29) Cho, K.; Leeladee, P.; McGown, A. J.; DeBeer, S.; Goldberg, D. P., *J. Am. Chem. Soc.* **2012,** *134*, 7392-7399.

(30) Cook, G. K.; Mayer, J. M., *J. Am. Chem. Soc.* **1995,** *117*, 7139-7156.

(31) Kim, S. S.; Baek, I. S.; Tuchkin, A.; Go, K. M., *J. Org. Chem.* **2001,** *66* , 4006-4011.

(32) Jones, W. D.; Feher, F. J., *Acc. Chem. Res.* **2002,** *22*, 91-100.

(33) Hedaya, E.; Winstein, S., *J. Am. Chem. Soc.* **1967,** *89*, 1661-1672.

(34) Foster, T. L.; Caradonna, J. P., *J. Am. Chem. Soc.* **2003,** *125*, 3678-3679.

(35) Rowe, G. T.; Rybak-Akimova, E. V.; Caradonna, J. P., *Chem. Eur. J.* **2008,** *14*, 8303-8311.

(36) Makhlynets, O. V.; Rybak-Akimova, E. V., *Chem. Eur. J.* **2010,** *16*, 13995-14006.

(37) Sawyer, D. T.; Sobkowiak, A.; Matsushita, T., *Acc. Chem. Res.* **1996,** *29*, 409-416.

(38) MacFaul, P. A.; Wayner, D. D. M.; Ingold, K. U., *Acc. Chem. Res.***1998,** *31*, 159-162.

(39) Goldstein, S.; Meyerstein, D., *Acc. Chem. Res.* **1999,** *32*, 547-550.

(40) Blackmond, D. G., *J. Am. Chem. Soc.***2015,** *137*, 10852-10866.

(41) Zolotova, N. V.; Denisov, E. T., *Bull. Acad. Sci. USSR, Div. Chem. Sci.* **1966,** *15*, 736-738.

(42) Steenken, S.; O'Neill, P., *J. Phys. Chem.* **1978,** *82* (3), 372-374.

(43) Maillard-Dupuy, C.; Guillard, C.; Courbon, H.; Pichat, P., *Environ. Sci. Technol.* **1994,** *28*, 2176-2183.

Supporting Information

Mechanistic Insights into Fe Catalyzed α-C-H Oxidations of Tertiary Amines

Christopher J. Legacy,[a] Frederick T. Greenaway,[b] Marion H. Emmert[a,c]*

[a]Department of Chemistry and Biochemistry, Worcester Polytechnic Institute, 100 Institute Road, Worcester, MA 01609, USA

[b]EPR studies.
Gustaf H. Carlson School of Chemistry, Clark University, 950 Main Street, Worcester, MA 01610, USA

[c]Current Address: Department of Process Research & Development, MRL, Merck & Co., Inc., 770 Sumneytown Pike, West Point, PA 19486, USA

Table of Contents

Materials and Methods

All reagents and solvents were used as received unless noted otherwise. Stirbars used in catalytic reactions were cleaned with aqua regia for at least 12 h under gentle stirring, rinsed with copious amounts of water, and dried in an oven at 120 °C prior to use. Standard solutions were prepared using volumetric flasks. All liquid reagents were dispensed by difference using gas-tight Hamilton syringes. Yields are reported as average yields of at least 2 experiments. The reported error is the standard deviation of at least two replicate trials. Unless noted otherwise, no efforts were made to exclude atmospheric air or moisture.

ESI-MS investigations were carried out on a Thermo Quest Finnigan LCQ DECA mass spectrometer using Tune Plus (v. 2.0) software

GC-MS analyses were carried out on an Agilent 7890B instrument using a 19091S-433 (HP-5MS; 30 m, 0.25 mm i.d., 0.25 μm df) column.

in-situ IR measurements were performed on a Mettler Toledo ReactIR15 instrument (serial number: R15-20251) using a 6.3 mm AgX DiComp probe and iC IR software.

Quantitative ^{1}H NMR measurements were performed using an adjusted method (15 s relaxation time, NS = 32) with 1,3-dinitrobenzene as internal standard.

X-band EPR experiments were carried out using a Bruker EMX instrument operating at 9.7 GHz with 100 kHz modulation. Spectra were acquired for liquid (room temperature, ca 20°C) and frozen solutions (ca 135K) in pyridine (15mL) as solvent with 9 equiv of water (406μL). Room temperature studies were carried out using a flat quartz aqueous cell (Wilmad LabGlass) while low temperature studies were carried out using 3mm i.d. thin wall quartz sample tubes (Wilmad).

2-Methyl-1-phenylpropan-2-yl benzoperoxoate was synthesized independently according to the literature.[1]

GCMS Spectrum of Reaction Mixture from NPr_3 C_α-H Oxidation Reaction

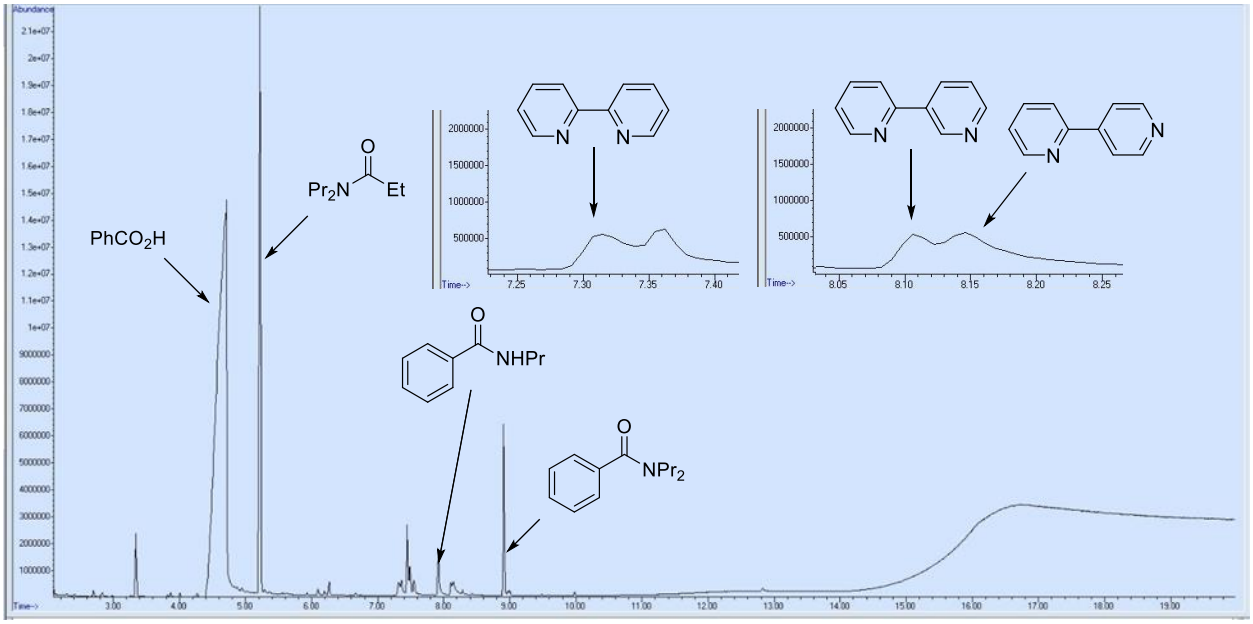

Figure S1. GCMS Chromatogram and Peak Assignments for Crude Tri(*n*-propyl)amine Oxidation Mixture.

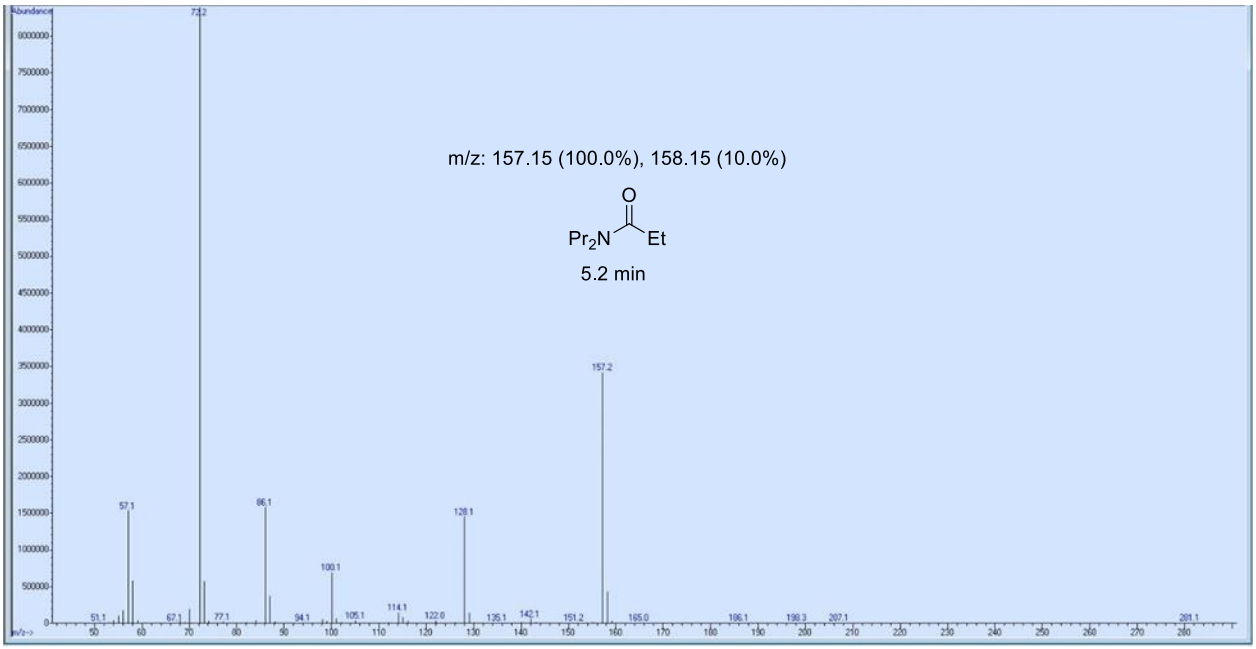

Figure S2. MS Spectrum derived from peak at 5.2 min.

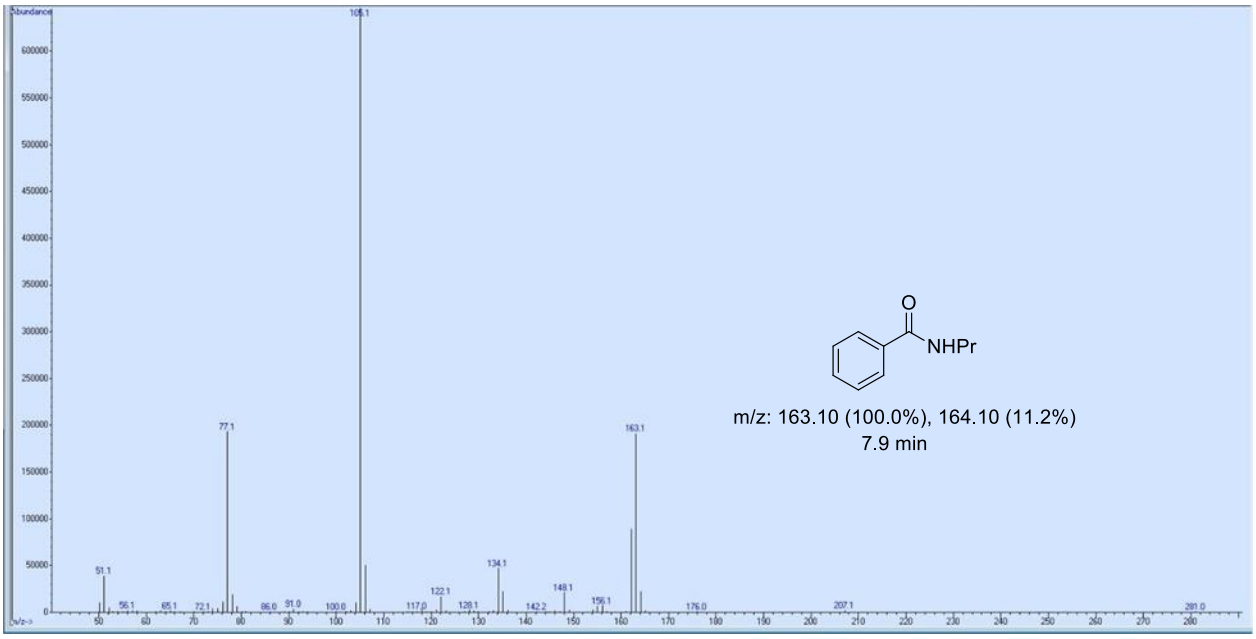

Figure S3. MS Spectrum derived from peak at 7.9 min.

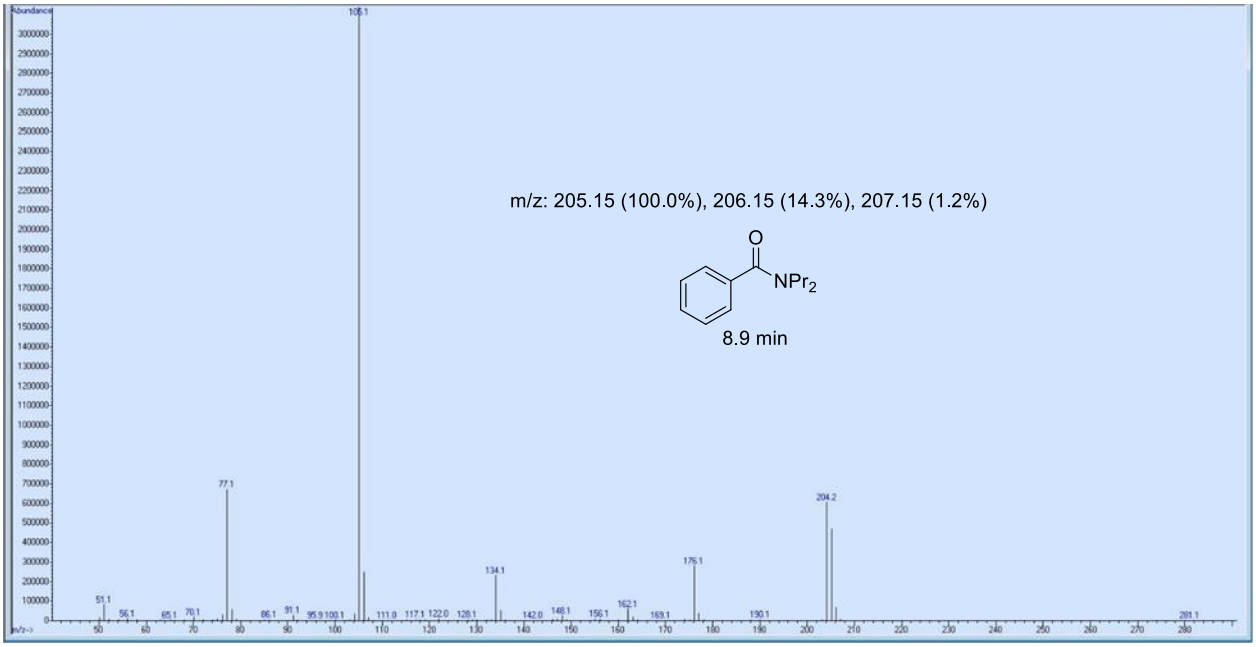

Figure S4. MS Spectrum derived from peak at 8.9 min.

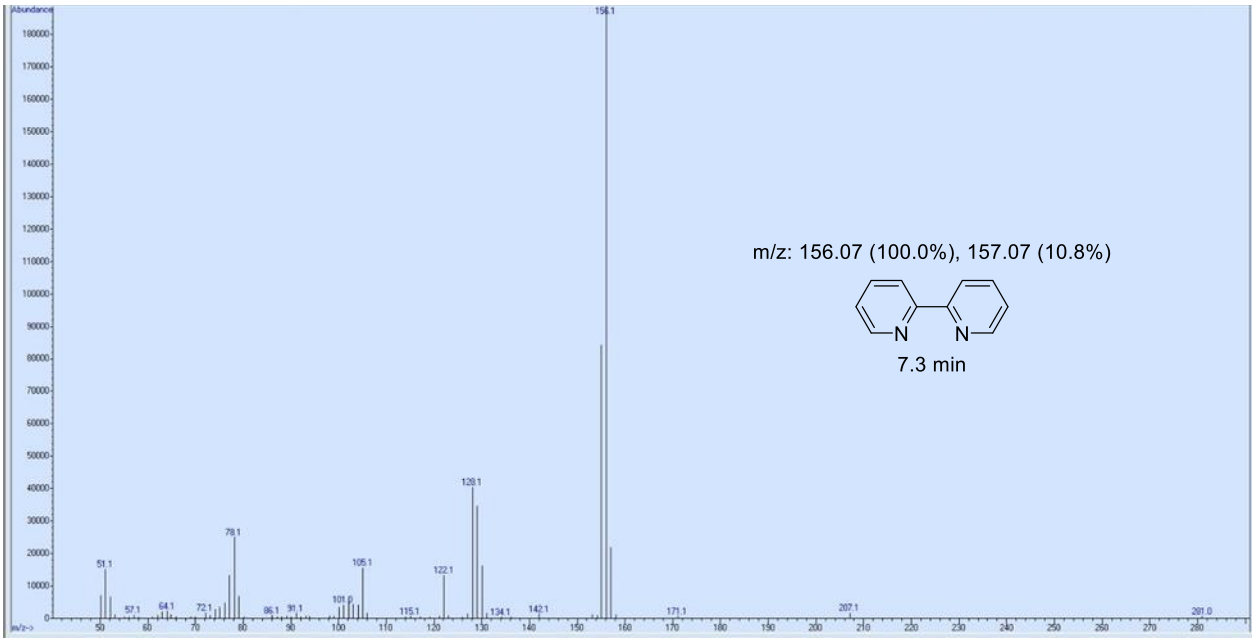

Figure S5. MS Spectrum derived from peak at 7.3 min.

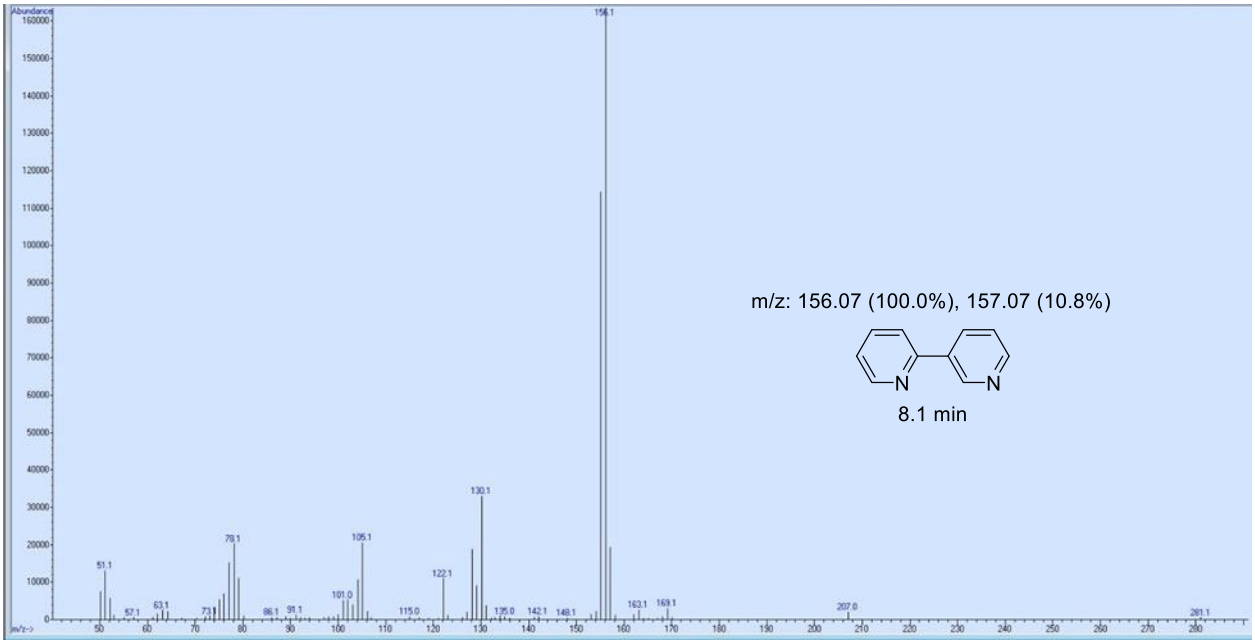

Figure S6 MS Spectrum derived from peak at 8.1 min.

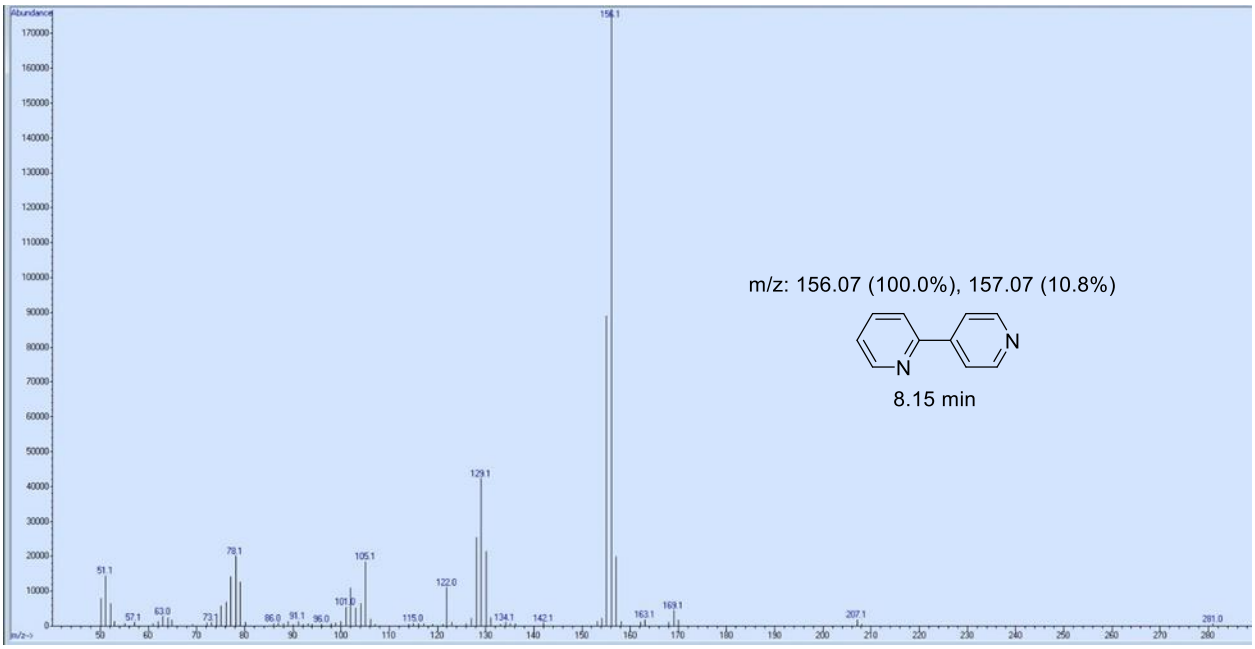

Figure S7. MS Spectrum derived from peak at 8.15 min.

Representative Procedure for Method of Initial Rates

To a 20 mL scintillation vial equipped with a Teflon-coated stirbar, $FeCl_3 \cdot 6H_2O$ (34 mg, 125 μmol, 5.0 mol %), picolinic acid (15 mg, 125 μmol, 5.0 mol %), pyridine (15 mL) and then deionized water (406 μL, 406 mg, 22.5 mmol, 9 eq.) was added. Three drops of mineral oil were placed in the bottom of a vial heating block well to improve heat transfer between the block and the reaction vial. The reaction vial was pressed into the vial well and twisted to maximize oil contact. The reaction was vigorously stirred (1500 rpm) to maximize heat transfer. The ReactIR 15 probe (see Materials and Methods) was then inserted into the open-top reaction vial and IR analysis was initiated. IR scans were taken at 15 s intervals. NPr_3 and $PhCO_3{}^tBu$, along with the solution, were preheated to 50 °C on the heating block. Reaction temperature was monitored using the IR probe. Once thermal equilibrium was reached at 50 °C, $PhCO_3{}^tBu$ (1.4 mL, 1.5 g, 7.5 mmol) was transferred to the reaction vial using a volumetric syringe. The concentration of $PhCO_3{}^tBu$ was monitored by selecting the IR band at ν =1757 cm^{-1} (C=O stretch). This IR band was unobscured by other bands in the spectrum; solvent subtraction was not performed. Once a steady signal was reached, preheated NPr_3 (476 μL, 358 mg, 2.5 mmol) was quickly added to the reaction. IR analysis was conducted to generate the spectra and reaction process traces.

As a typical analysis of the raw data obtained in such a fashion, IR absorbance at ν =1757 cm^{-1} (C=O stretch of $PhCO_3{}^tBu$) was plotted against reaction time and the maximum negative slope (corresponding to the maximum reaction rate, Eq. 1) was determined, using Excel. These reaction rates (slopes) were then plotted against equivalents of analyte reagent to obtain initial rates of each analyte.

$$\text{rate} = -\frac{d[R]}{dt} = \frac{d[P]}{dt} \qquad (Eq.1)$$

Equation 1: Relationship of Rate to Concentration of Reactants and Products.

In order to establish a correlation between product formation and the consumption of $PhCO_3{}^tBu$, the representative reaction described above was conducted, and samples were taken every 15 minutes for GC analysis (Figure S8). The rate of product formation corresponded to the observed rate of $PhCO_3{}^tBu$ consumption during the initial rate period (up to ~0.5 h), which demonstrates the viability of *in-situ* FTIR measurement of $PhCO_3{}^tBu$ decay to gain insight into amine oxidation. At later reaction times, a delay in product formation vs. $PhCO_3{}^tBu$ consumption is observed, which is consistent with the observation of an intermediate in the reaction. Our previous work[2] suggests that the observed intermediate is a hemiaminal. In combination, these data suggest that the first amine alpha-oxidation is fast, while formation of the amide from the hemiaminal is a slower reaction.

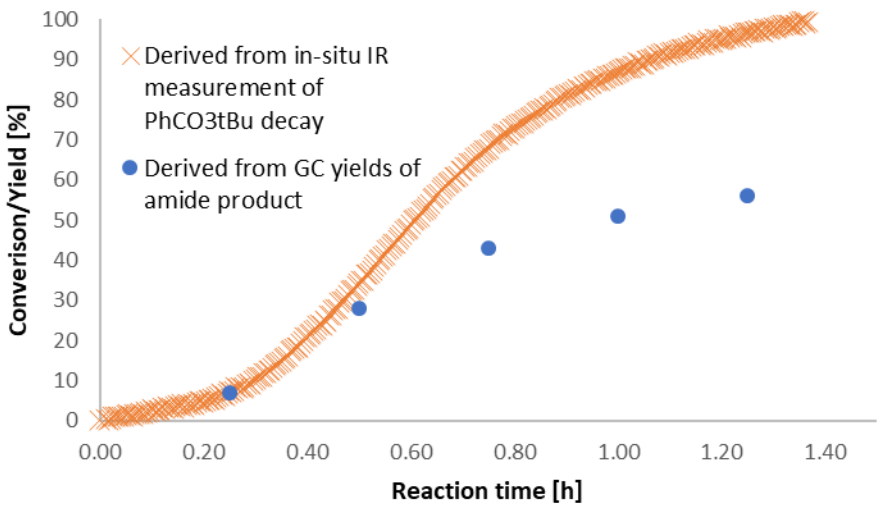

Figure S8: Conversion obtained from decrease of $PhCO_3{}^tBu$ in-situ IR signal (orange crosses) and reaction yield as measured by calibrated GC yield of amide product (blue dots) versus time.

Optimization of 2-Picolinic Acid Loading

By analogy with the general procedure for method of initial rates, $FeCl_3 \cdot 6H_2O$ (34 mg, 125 μmol, 5.0 mol %), picolinic acid (Table S1), pyridine (15 mL) and then deionized H_2O (406 μL, 406 mg, 22.5 mmol, 9 eq.) were added to a 20 mL scintillation vial equipped with a microstirbar. The reaction mixture was heated to 50 °C on a pre-heated vial plate and vigorously stirred (1500 rpm). The ReactIR15 probe (see Materials and Methods) was inserted into the reaction vial and IR analysis was initiated. Subsequently, preheated $PhCO_3{}^tBu$ (1.4 mL, 1.5 g, 7.5 mmol) and then NPr_3 (476 μL, 358 mg, 2.5 mmol) were added to the reaction.

IR analysis was conducted to generate the kinetic traces shown below (Figure S9). $-k_{obs}[PhCO_3{}^tBu]$ was determined by determining the maximum slope of the reaction trace after the initiation period. The studies were repeated at least twice and the average values of $-k_{obs}[PhCO_3{}^tBu]$ as well as the obtained standard deviations are tabulated in Table S1.

Table S1. Dependence of Maximum Reaction Rate on Loading of 2-Picolinic Acid at 5 mol % $FeCl_3$ Loading.

Entry	mol % 2-picolinic acid	$-k_{obs}[PhCO_3{}^tBu]$
1	2.5	9.5 ± 0.4
2	5.0	10.8 ± 0.3
3	7.5	10.4 ± 0.3
4	10	9.8 ± 0.2

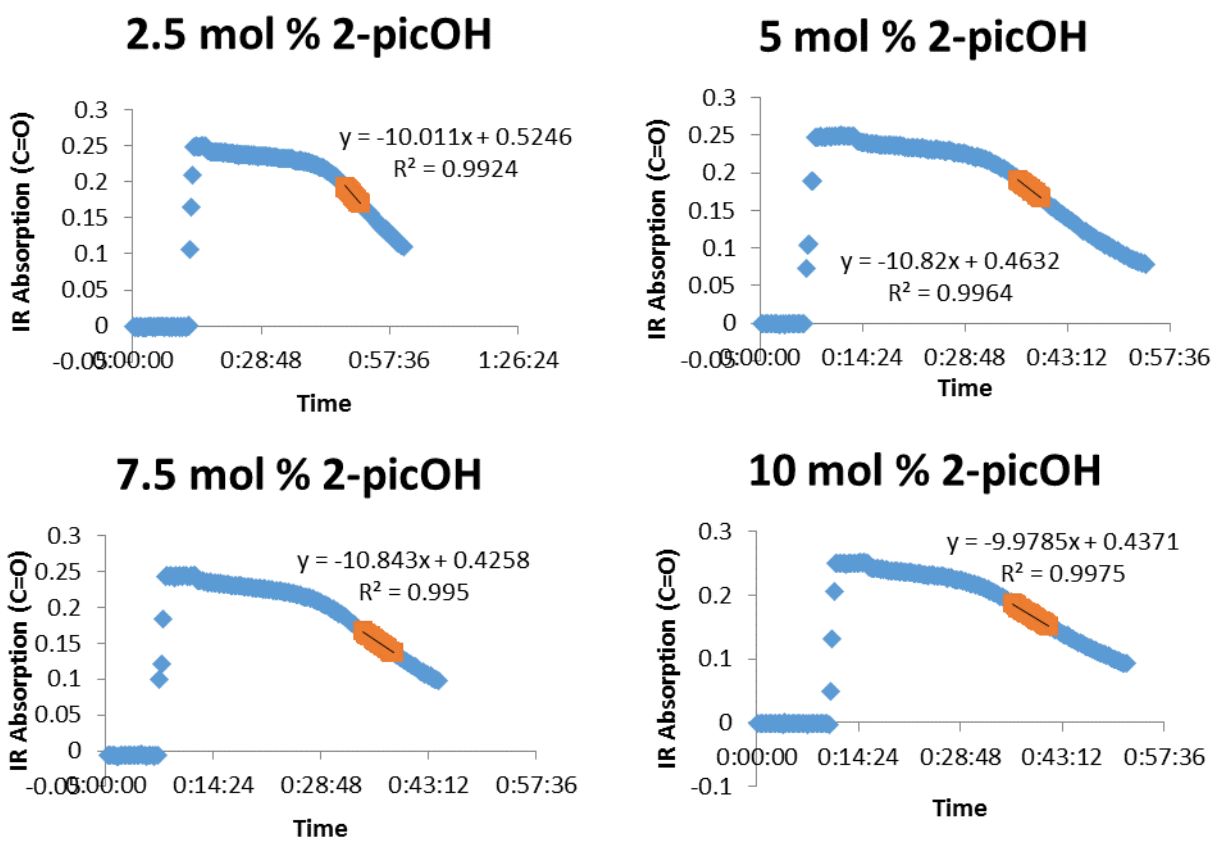

Figure S9. Decrease of [$PhCO_3{}^tBu$] versus Time for Different 2-Picolinic Acid Loadings (Fe Loading 5.0 mol %).

Initial Rates with Different Fe(III) Salts

By analogy with the general procedure for method of initial rates, Fe salts (5.0 mol % [Fe], see Table S2), picolinic acid (15 mg, 125 μmol, 5.0 mol %), pyridine (15 mL) and then deionized H_2O (406 μL, 406 mg, 22.5 mmol, 9 eq.) were added to a 20 mL scintillation vial equipped with a microstirbar. The reaction mixture was heated to 50 °C on a pre-heated vial plate and vigorously stirred (1500 rpm). The ReactIR15 probe was inserted into the reaction vial and IR analysis was initiated. Subsequently, preheated $PhCO_3{}^tBu$ (1.4 mL, 1.5 g, 7.5 mmol) and then preheated NPr_3 (476 μL, 358 mg, 2.5 mmol) were added to the reaction.

IR analysis was conducted to generate the kinetic traces shown below (Figure S11). $-k_{obs}$ $[PhCO_3{}^tBu]$ was determined by determining the maximum slope of the reaction trace after the initiation period. The studies were repeated at least twice and the average values of $-k_{obs}$ $[PhCO_3{}^tBu]$ as well as the obtained standard deviations are tabulated in Table S2.

Table S2. Dependence of Maximum Reaction Rate on Identity of Fe(III) Salt.

Entry	Fe Salt	pK_a of corresponding acid of X-type ligand in H_2O	$-k_{obs}$ $[PhCO_3{}^tBu]$
1	$Fe(OTf)_3$	-14.7	7.6 ± 0..3
2	$FeCl_3$	-8	8.1 ± 0.3
3	$Fe(NO_3)_3$	-1.3	8.0 ± 0.2
4	$Fe_2(SO_4)_3$	1.99	6.9 ± 0.1
5	$Fe(acac)_3$	9.8	7.1 ± 0.1

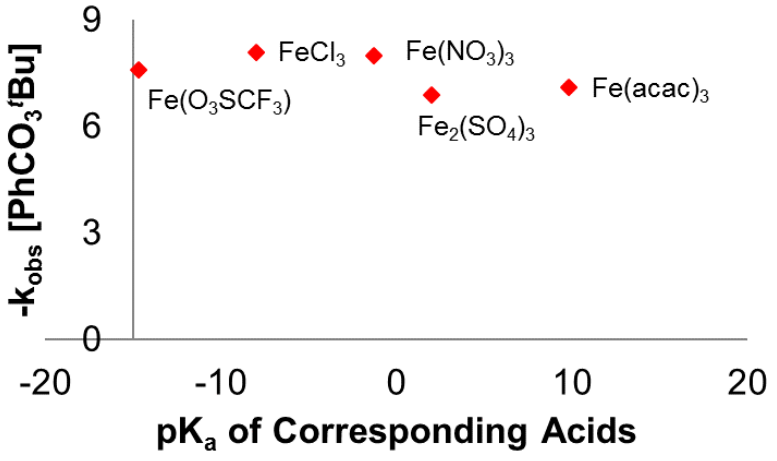

Figure S10. Maximum Reaction Rate versus pKa of Corresponding Acid for different X-type Ligands.

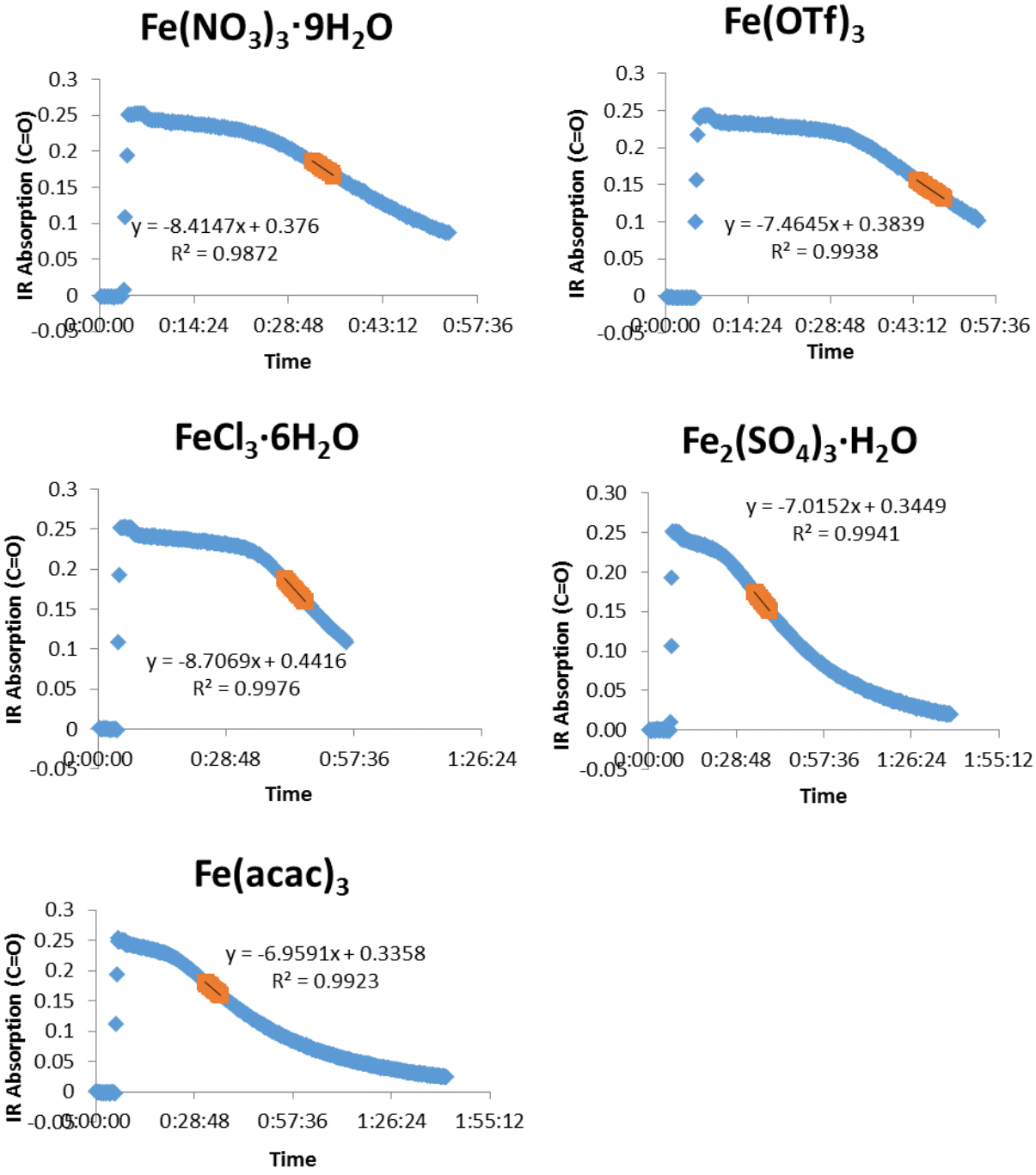

Figure S11. Decrease of [PhCO$_3$^{t}Bu] versus Time for Different Fe(III) Catalyst Precursors.

Kinetic Order in NPr_3

By analogy with the general procedure for method of initial rates, $FeCl_3 \cdot 6H_2O$ (34 mg, 125 μmol, 5.0 mol %), picolinic acid (15 mg, 125 μmol, 5.0 mol %), pyridine (15 mL) and then deionized H_2O (406 μL, 406 mg, 22.5 mmol, 9 eq.) were added to a 20 mL scintillation vial equipped with a microstirbar. The reaction mixture was heated to 50 °C on a pre-heated vial plate and vigorously stirred (1500 rpm). The ReactIR15 probe was inserted into the reaction vial and IR analysis was initiated. Subsequently, preheated $PhCO_3{}^tBu$ (1.4 mL, 1.5 g, 7.5 mmol) and then preheated NPr_3 (Table S3) were added to the reaction.

IR analysis was conducted to generate the kinetic traces shown below (Figure S12). $-k_{obs}[PhCO_3{}^tBu]$ was determined by determining the maximum slope of the reaction trace after the initiation period. The studies were repeated at least twice and the average values of $-k_{obs}[PhCO_3{}^tBu]$ as well as the obtained standard deviations are tabulated in Table S3.

Table S3. Dependence of Maximum Reaction Rate on NPr_3 Loading.

Entry	Eq. NPr_3	$-k_{obs}[PhCO_3{}^tBu]$
1	0.25	2.86 ± 0.4
2	0.5	4.44 ± 0.3
3	0.75	5.84 ± 0.1
4	1	7.63 ± 0.1
5	5	8.06
6	10	7.00

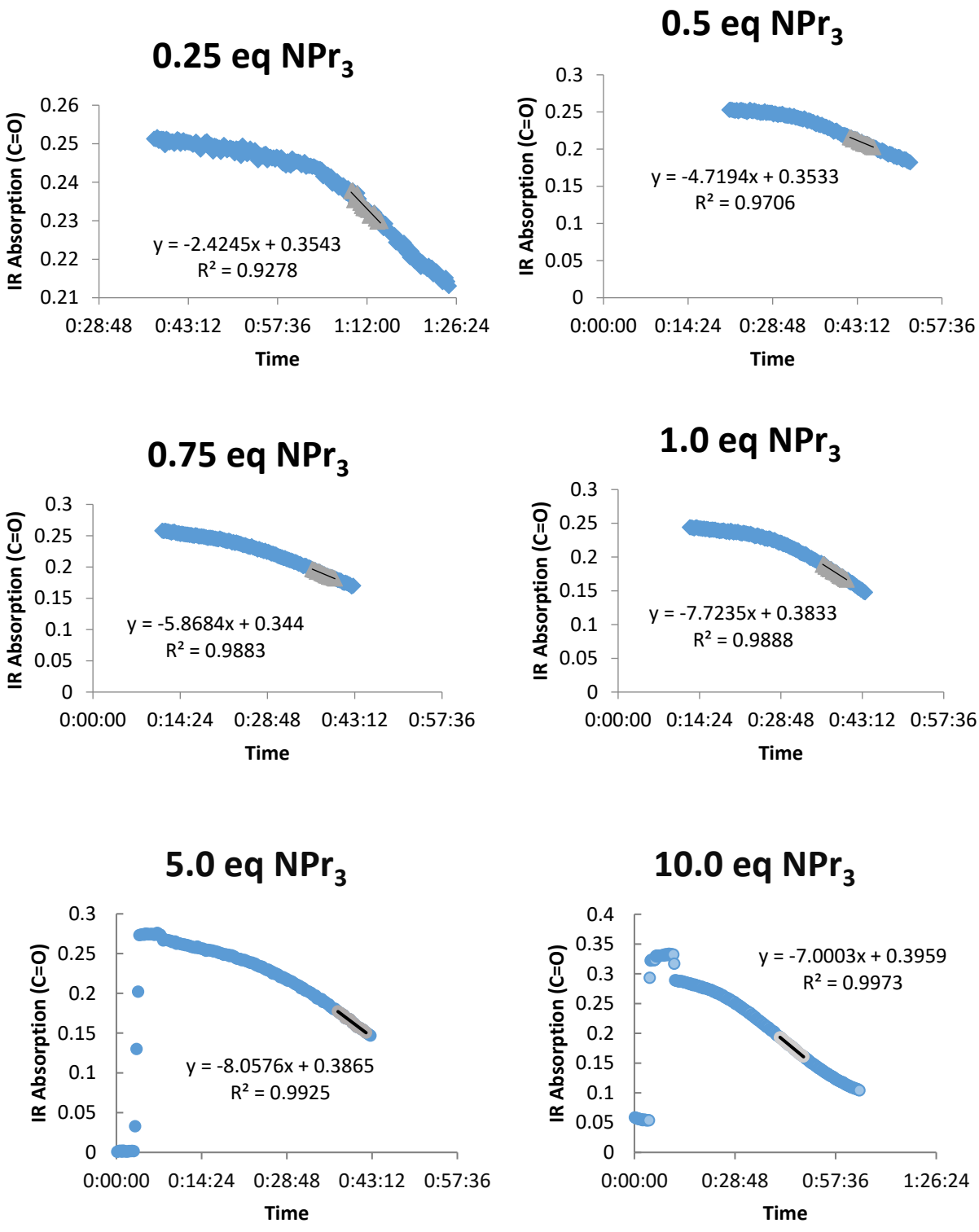

Figure S12. Decrease of [$PhCO_3{}^tBu$] versus Time for Different [NPr_3].

Kinetic Order in $PhCO_3{}^tBu$

By analogy with the general procedure for method of initial rates, $FeCl_3 \cdot 6H_2O$ (34 mg, 125 μmol, 5.0 mol %), picolinic acid (15 mg, 125 μmol, 5.0 mol %), pyridine (15 mL) and then deionized H_2O (406 μL, 406 mg, 22.5 mmol, 9 eq.) were added to a 20 mL scintillation vial equipped with a microstirbar. The reaction mixture was heated to 50 °C on a pre-heated vial plate and vigorously stirred (1500 rpm). The ReactIR15 probe (see Materials and Methods) was inserted into the reaction vial and IR analysis was initiated. Subsequently, preheated $PhCO_3{}^tBu$ (see Table S4) and then NPr_3 (476 μL, 358 mg, 2.5 mmol) were added to the reaction.

IR analysis was conducted for 4 h to generate kinetic traces shown below (Figure S13). $-k_{obs}$ $[PhCO_3{}^tBu]$ was determined by determining the maximum slope of the reaction trace after the initiation period. The studies were repeated at least twice and the average values of $-k_{obs}$ $[PhCO_3{}^tBu]$ as well as the obtained standard deviations are tabulated in Table S4.

Table S4. Dependence of Maximum Reaction Rate on $PhCO_3{}^tBu$ Loading.

Entry	Eq. $PhCO_3{}^tBu$	$-k_{obs}$ $[PhCO_3{}^tBu]$
1	1.0	4.5 ± 0.1
2	2.0	8.5 ± 0.4
3	3.0	10.75 ± 0.3
4	4.0	14.0 ± 0.2
5	8.0	14.0
6	15.0	14.3

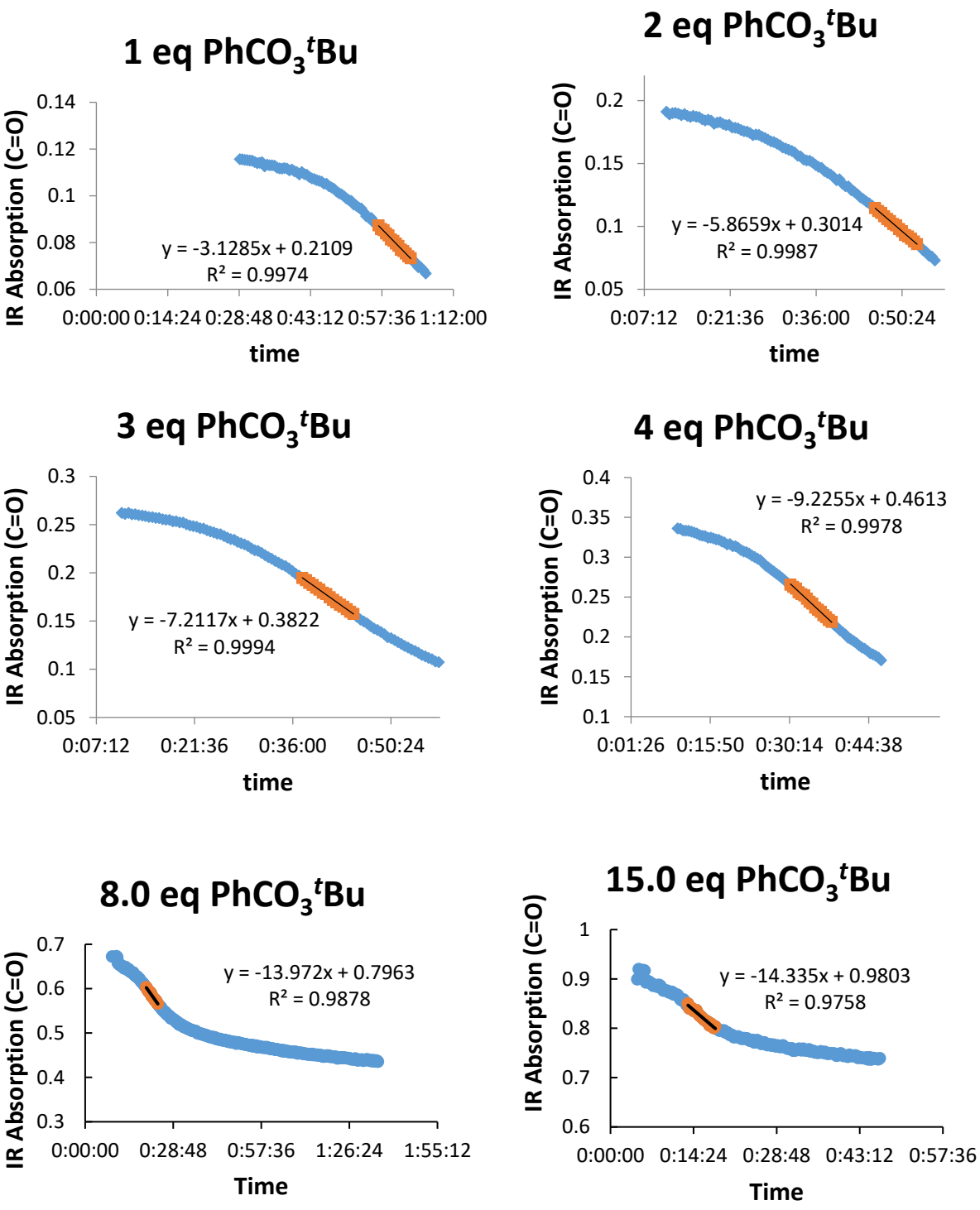

Figure S13. Decrease of [$PhCO_3{}^tBu$] versus Time for Different [$PhCO_3{}^tBu$].

Kinetic Order in H_2O

By analogy with the general procedure for method of initial rates, $FeCl_3 \cdot 6H_2O$ (34 mg, 125 μmol, 5.0 mol %), picolinic acid (15 mg, 125 μmol, 5.0 mol %), pyridine (15 mL) and then deionized H_2O (Table S5) were added to a 20 mL scintillation vial equipped with a microstirbar. The reaction mixture was heated to 50 °C on a pre-heated vial plate and vigorously stirred (1500 rpm). The ReactIR15 probe (see Materials and Methods) was inserted into the reaction vial and IR analysis was initiated. Subsequently, preheated $PhCO_3{}^tBu$ (1.4 mL, 1.5 g, 7.5 mmol) and then NPr_3 (476 μL, 358 mg, 2.5 mmol) were added to the reaction.

IR analysis was conducted to generate kinetic traces, of which several are shown below (Figure S14). $-k_{obs}$ $[PhCO_3{}^tBu]$ was determined by determining the maximum slope of the reaction trace after the initiation period. The studies were repeated at least twice and the average values of $-k_{obs}$ $[PhCO_3{}^tBu]$ as well as the obtained standard deviations are tabulated in Table S5.

Table S5. Dependence of Maximum Reaction Rate on H_2O Loading.

Entry	Eq. H_2O	$-k_{obs}$ $[PhCO_3{}^tBu]$
1	0.4	23.3 ± 0.5
2	0.8	19.4 ± 0.3
3	1.25	16.8 ± 0.2
4	1.6	16.6 ± 0.1
5	2.0	16.2 ± 0.4
6	2.5	13.7 ± 1.3
7	5.0	12.5 ± 0.4
8	7.5	10.9 ± 1.2
9	10.0	9.8 ± 0.1
10	12.5	9.4 ± 0.1
11	15.0	9.1 ± 0.6
12	20.0	7.2 ± 0.2

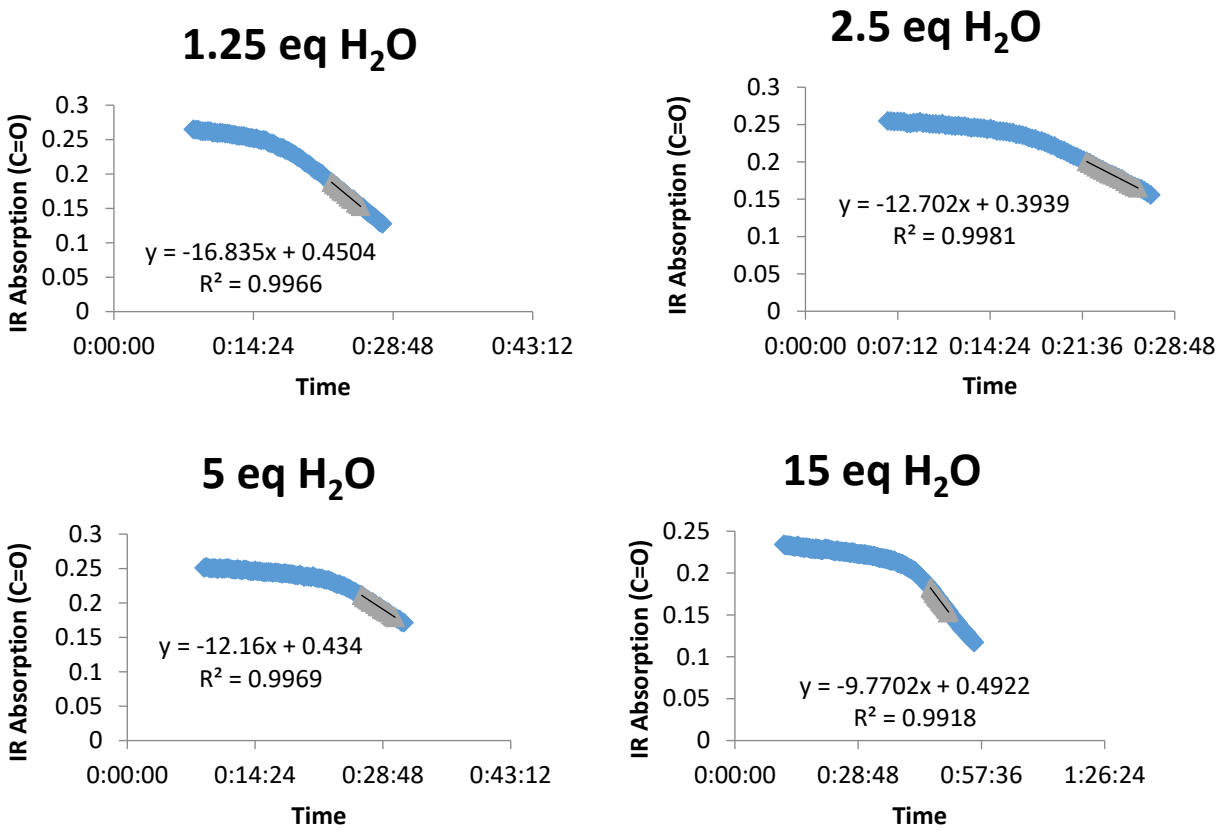

Figure S14. Examples of Decrease of [$PhCO_3{}^tBu$] versus Time for Selected [H_2O].

Kinetic Order in $FeCl_3 \cdot 6H_2O$/Picolinic Acid (1:1)

By analogy with the general procedure for method of initial rates, $FeCl_3 \cdot 6H_2O$ (Table S6), picolinic acid (Table S6), pyridine (15 mL) and then deionized H_2O (406 μL, 406 mg, 22.5 mmol, 9 eq.) were added to a 20 mL scintillation vial equipped with a microstirbar. The reaction mixture was heated to 50 °C on a pre-heated vial plate and vigorously stirred (1500 rpm). The ReactIR15 probe (see Materials and Methods) was inserted into the reaction vial and IR analysis was initiated. Subsequently, preheated $PhCO_3{}^tBu$ (1.4 mL, 1.5 g, 7.5 mmol) and then preheatedNPr_3 (476 μL, 358 mg, 2.5 mmol) were added to the reaction.

IR analysis was conducted to generate reaction process traces, of which several are shown below (Figure S15). $-k_{obs}[PhCO_3{}^tBu]$ was determined by determining the maximum slope of the reaction trace after the initiation period. The studies were repeated at least twice and the average values of $-k_{obs}[PhCO_3{}^tBu]$ as well as the obtained standard deviations are tabulated in Table S6.

Table S6. Dependence of Maximum Reaction Rate on $FeCl_3$/2-picolinic acid Loading.

Entry	mol % $FeCl_3$/2-picolinic acid (1:1)	$-k_{obs}[PhCO_3{}^tBu]$
1	0.5	7.2 ± 0.2
2	1.5	9.2 ± 0.3
3	2	9.8 ± 0.1
4	3	10.5 ± 0.1
5	5	10.8 ± 0.3
6	7	11.3 ± 0.1
7	10	11.6 ±0.2
8	17	12.4 ± 0.4
9	25	8.2 ± 0.4
10	32	7.0 ± 0.2
11	40	4.2 ± 0.1

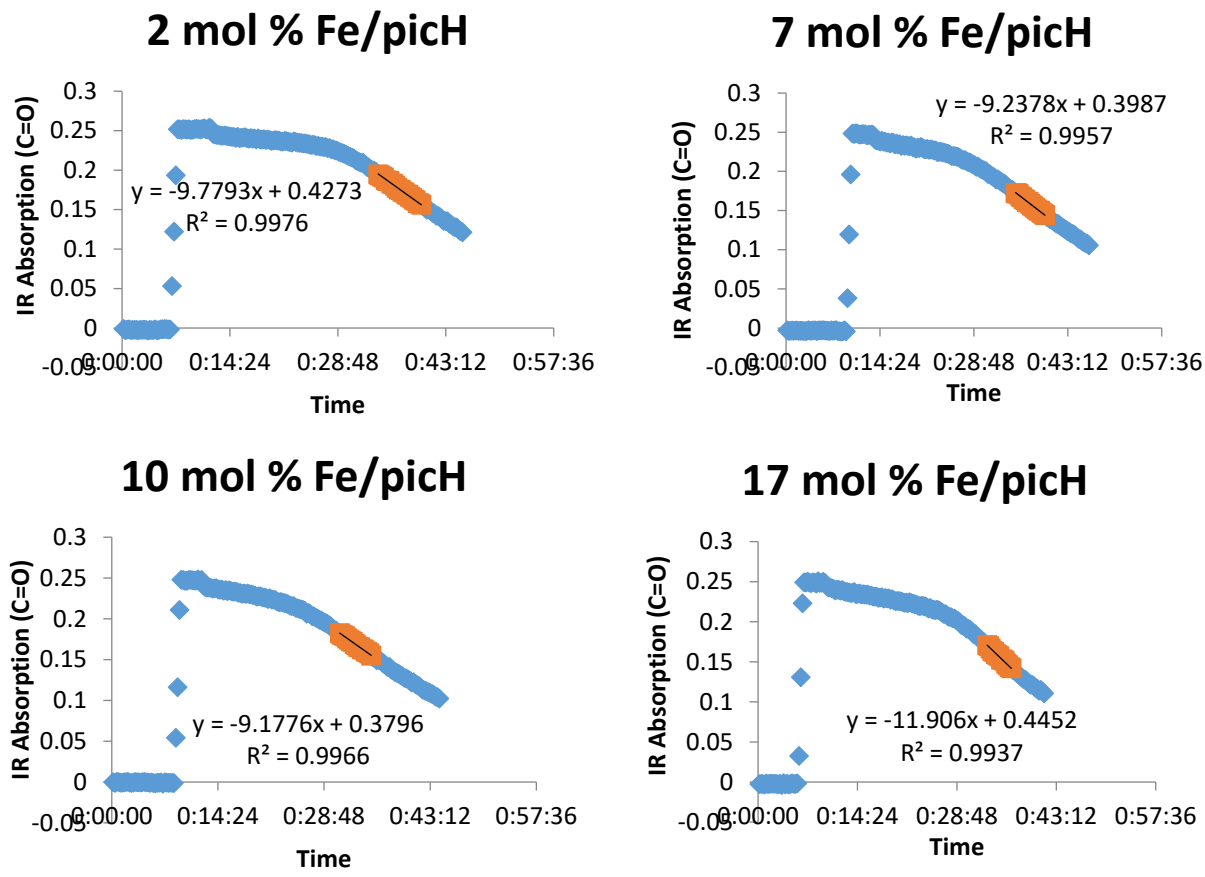

Figure S15. Examples of Decrease of [$PhCO_3{}^tBu$] versus Time for Selected [$FeCl_3$/2-picolinic acid] (1:1).

Kinetic Order in $PhCO_2H$

By analogy with the general procedure for method of initial rates, $FeCl_3 \cdot 6H_2O$ (34 mg, 125 μmol, 5.0 mol %), picolinic acid (15 mg, 125 μmol, 5.0 mol %), $PhCO_2H$ (Table S7), pyridine (15 mL) and then deionized H_2O (406 μL, 406 mg, 22.5 mmol, 9 eq.) were added to a 20 mL scintillation vial equipped with a microstirbar. The reaction mixture was heated to 50 °C on a pre-heated vial plate and vigorously stirred (1500 rpm). The ReactIR15 probe (see Materials and Methods) was inserted into the reaction vial and IR analysis was initiated. Subsequently, preheated $PhCO_3{}^tBu$ (1.4 mL, 1.5 g, 7.5 mmol) and then preheated NPr_3 (476 μL, 358 mg, 2.5 mmol) were added to the reaction.

IR analysis was conducted to generate the reaction process traces shown below (Figure S16). $-k_{obs}$ $[PhCO_3{}^tBu]$ was determined by determining the maximum slope of the reaction trace after the initiation period. The studies were repeated at least twice and the average values of $-k_{obs}$ $[PhCO_3{}^tBu]$ as well as the obtained standard deviations are tabulated in Table S7.

Table S7. Dependence of Maximum Reaction Rate on $PhCO_2H$ Addition.

Entry	Eq. $PhCO_2H$	$-k_{obs}$ $[PhCO_3{}^tBu]$
1	1.0	7.2 ± 1.6
2	2.0	5.0 ± 0.6
3	3.0	4.1 ± 0.7
4	4.0	2.6 ± 0.4

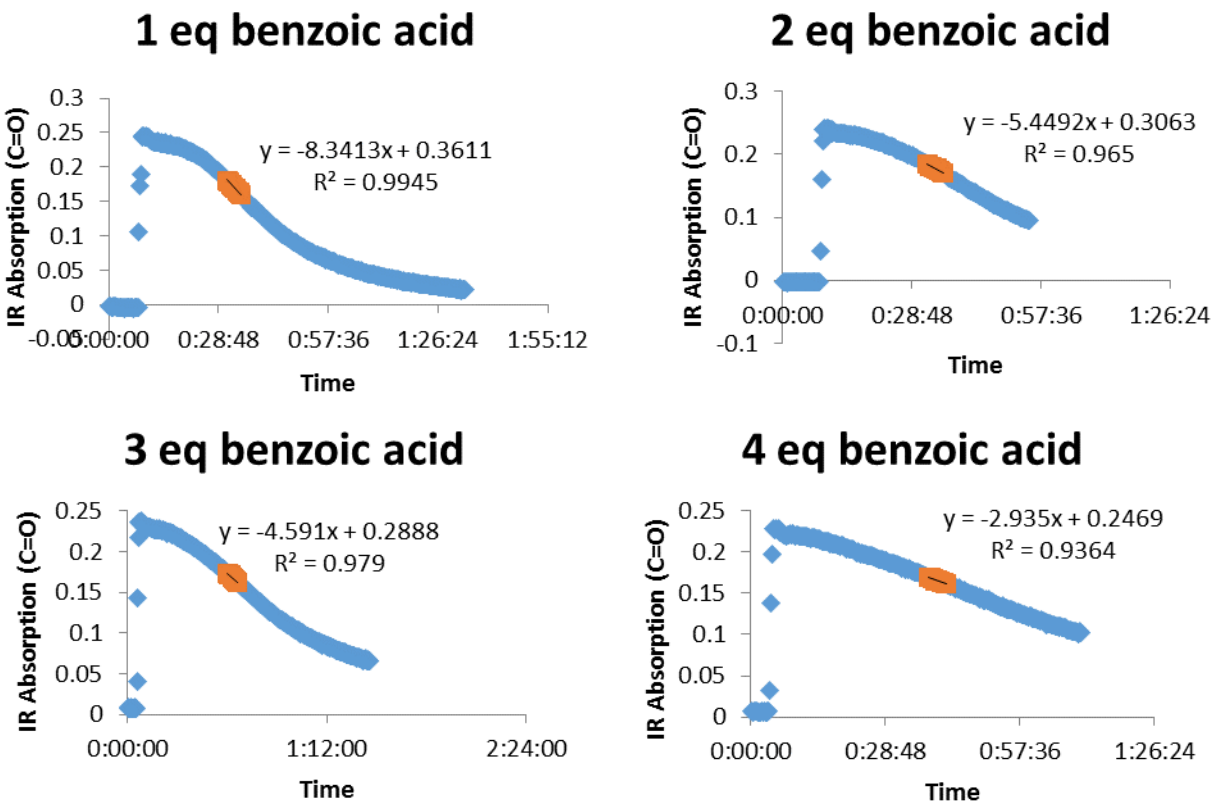

Figure S16. Decrease of [$PhCO_3{}^tBu$] versus Time for Selected $PhCO_2H$ Loadings.

Kinetic Order in ^{t}BuOH

By analogy with the general procedure for method of initial rates, $FeCl_3 \cdot 6H_2O$ (34 mg, 125 μmol, 5.0 mol %), picolinic acid (15 mg, 125 μmol, 5.0 mol %), pyridine (15 mL), deionized H_2O (406 μL, 406 mg, 22.5 mmol, 9 eq.) and then ^{t}BuOH (Table S8) were added to a 20 mL scintillation vial equipped with a microstirbar. The reaction mixture was heated to 50 °C on a pre-heated vial plate and vigorously stirred (1500 rpm). The ReactIR15 probe (see Materials and Methods) was inserted into the reaction vial and IR analysis was initiated. Subsequently, preheated $PhCO_3{}^tBu$ (1.4 mL, 1.5 g, 7.5 mmol) and then NPr_3 (476 μL, 358 mg, 2.5 mmol) were added to the reaction.

IR analysis was conducted to generate the reaction process traces shown below (Figure S17). $-k_{obs}$ [$PhCO_3{}^tBu$] was determined by determining the maximum slope of the reaction trace after the initiation period. The studies were repeated at least twice and the average values of $-k_{obs}$ [$PhCO_3{}^tBu$] as well as the obtained standard deviations are tabulated in Table S8.

Table S8. Dependence of Maximum Reaction Rate on ^{t}BuOH Addition.

Entry	Eq. ^{t}BuOH	$-k_{obs}$ [$PhCO_3{}^tBu$]
1	1.0	7.3 ± 1.2
2	2.0	7.2 ± 1.4
3	3.0	7.1 ± 1.5
4	4.0	6.9 ± 0.3

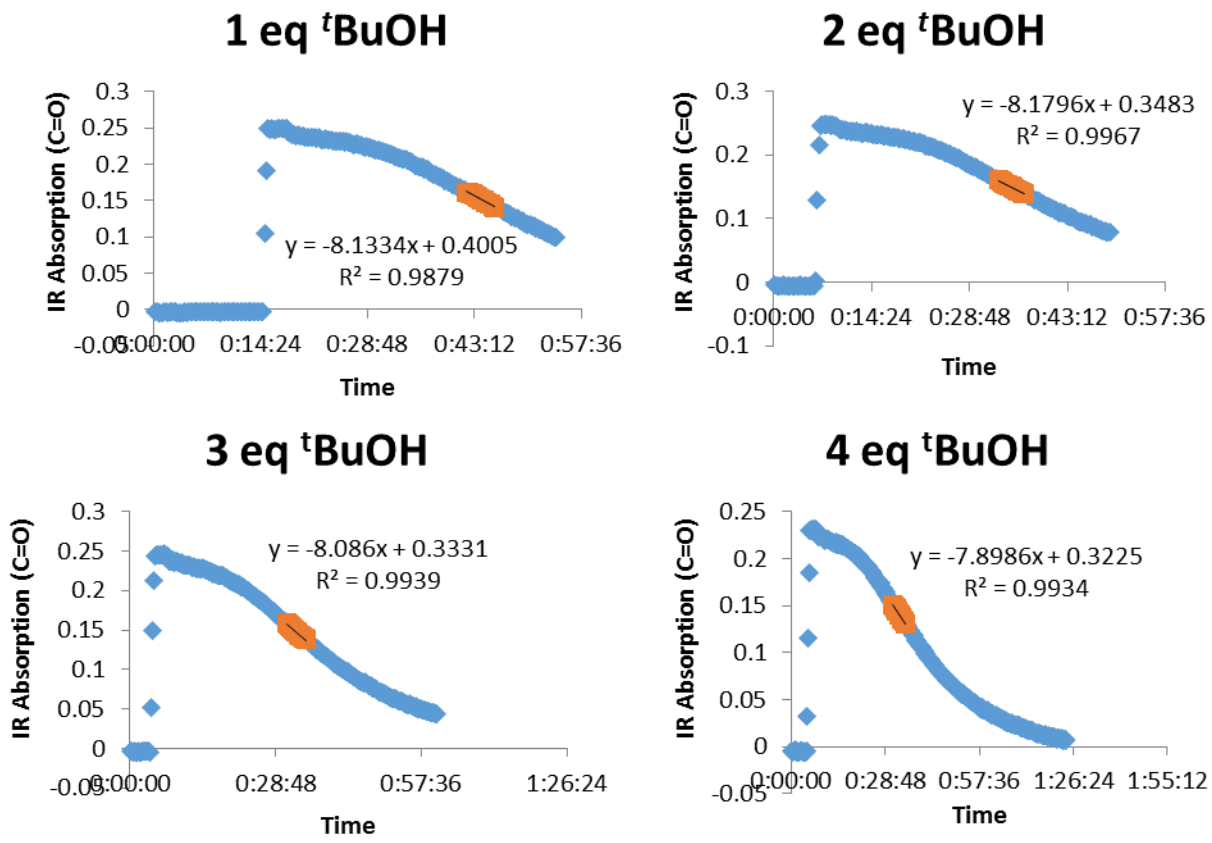

Figure S17. Decrease of [PhCO$_3$^{t}Bu] versus Time for Selected ^{t}BuOH Loadings.

Kinetic Order in Pyridine

By analogy with the general procedure for method of initial rates, $FeCl_3 \cdot 6H_2O$ (34 mg, 125 μmol, 5.0 mol %), picolinic acid (15 mg, 125 μmol, 5.0 mol %), EtOAc (15 mL), deionized H_2O (406 μL, 406 mg, 22.5 mmol, 9 eq.) and then pyridine (Table S9) were added to a 20 mL scintillation vial equipped with a microstirbar. The reaction mixture was heated to 50 °C on a pre-heated vial plate and vigorously stirred (1500 rpm). The ReactIR15 probe (see Materials and Methods) was inserted into the reaction vial and IR analysis was initiated. Subsequently, preheated $PhCO_3{}^tBu$ (1.4 mL, 1.5 g, 7.5 mmol) and then NPr_3 (476 μL, 358 mg, 2.5 mmol) were added to the reaction.

IR analysis was conducted to generate the reaction process traces shown below (Figure S18). $-k_{obs}$ [$PhCO_3{}^tBu$] was determined by determining the maximum slope of the reaction trace after the initiation period. The studies were repeated at least twice and the average values of $-k_{obs}$ [$PhCO_3{}^tBu$] as well as the obtained standard deviations are tabulated in Table S9.

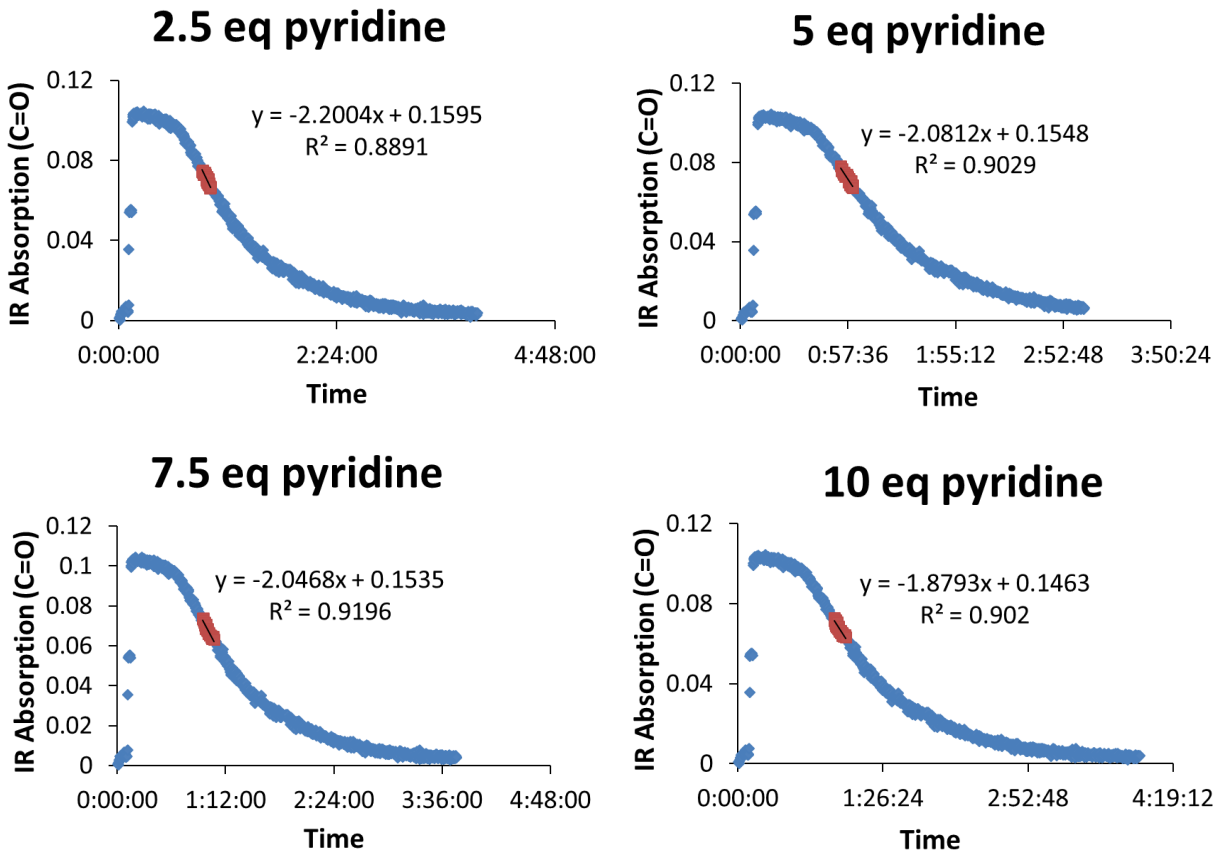

Figure S18. Decrease of [$PhCO_3{}^tBu$] versus Time for Selected Pyridine Loadings.

Table S9. Dependence of Maximum Reaction Rate on pyridine Addition.

Entry	Eq. Pyridine	$-k_{obs}$ [$PhCO_3{}^tBu$]
1	2.5	2.1 ± 0.1
2	5.0	1.9 ± 0.2
3	7.5	2.1 ± 0.2
4	10.0	2.0 ± 0.1

Kinetic Isotope Effect

By analogy with the general procedure for method of initial rates, $FeCl_3 \cdot 6H_2O$ (17 mg, 62.5 μmol, 5.0 mol %), picolinic acid (8 mg, 62.5 μmol, 5.0 mol %), pyridine (8 mL), and then deionized H_2O (203 μL, 203 mg, 11.3 mmol, 9 eq.) were added to a 20 mL scintillation vial equipped with a microstirbar. The reaction mixture was heated to 50 °C on a pre-heated vial plate and vigorously stirred (1500 rpm). The ReactIR15 probe (see Materials and Methods) was inserted into the reaction vial and IR analysis was initiated. Subsequently, preheated $PhCO_3{}^tBu$ (700 μL, 728 mg, 3.8 mmol) and then preheated substrate (Table S10) were added to the reaction.

IR analysis was conducted to generate the reaction process traces shown below (Figure S19). $-k_{obs}$ $[PhCO_3{}^tBu]$ was determined by determining the maximum slope of the reaction trace after the initiation period. The studies were repeated at least twice and the average values of $-k_{obs}$ $[PhCO_3{}^tBu]$ as well as the obtained standard deviations are tabulated in Table S10.

Table S10. Maximum Reaction Rates for NEt_3 and D_{15}-NEt_3.

Entry	Substrate	Loading	$-k_{obs}$ $[PhCO_3{}^tBu]$
1	NEt_3	174 μL, 126 mg, 1.25 mmol, 5 mol %	14.2 ± 0.1
2	NEt_3-D_{15}	175 μL, 145 mg, 1.25 mmol, 5 mol %	8.2 ± 0.1

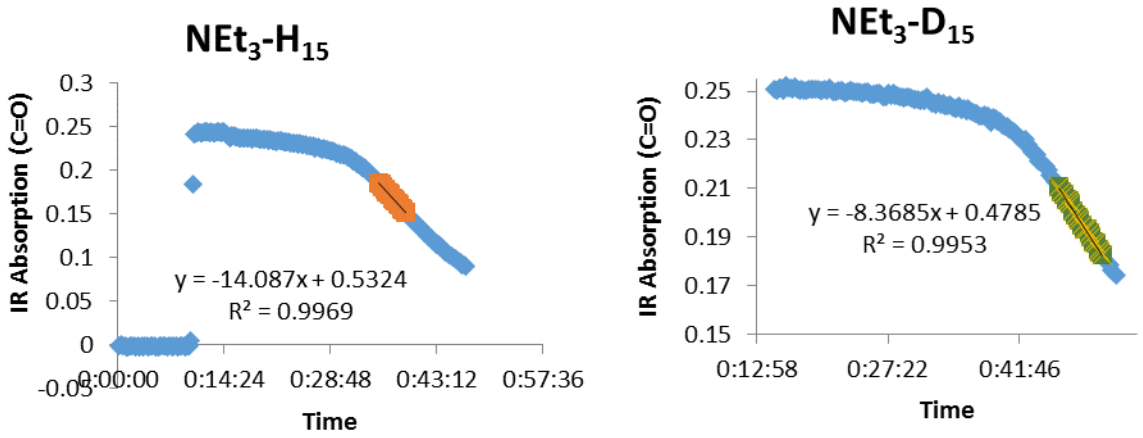

Figure S19. Decrease of $[PhCO_3{}^tBu]$ versus Time for NEt_3 and NEt_3-D_{15}.

Dependence of Initiation Period Length on Order of Reagent Addition

By analogy with the general procedure for method of initial rates, $FeCl_3 \cdot 6H_2O$ (34 mg, 125 μmol, 5.0 mol %), picolinic acid (15 mg, 125 μmol, 5.0 mol %), pyridine (15 mL), and then deionized H_2O (406 μL, 406 mg, 22.5 mmol, 9 eq.) were added to a 20 mL scintillation vial equipped with a microstirbar. The reaction mixture was heated to 50 °C on a pre-heated vial plate and vigorously stirred (1500 rpm). The ReactIR15 probe (see Materials and Methods) was inserted into the reaction vial and IR analysis was initiated. Subsequently, preheated NPr_3 (476 μL, 358 mg, 2.5 mmol) and then $PhCO_3{}^tBu$ (1.4 mL, 1.5 g, 7.5 mmol) were added to the reaction (Table S11, Entry 2). Alternatively, the originally used order of reagent addition was used: first preheated $PhCO_3{}^tBu$ (1.4 mL, 1.5 g, 7.5 mmol) and then preheated NPr_3 (476 μL, 358 mg, 2.5 mmol; see entry 1, Table S11).

IR analysis was conducted to generate the reaction process traces shown below; temperature was recorded in addition to IR absorption (Figure S20). $-k_{obs}$ [$PhCO_3{}^tBu$] was determined by determining the maximum slope of the reaction trace after the initiation period. The studies were repeated at least twice and the average values of $-k_{obs}$ [$PhCO_3{}^tBu$] as well as the obtained standard deviations are tabulated in Table S11.

Table S11. Maximum Reaction Rates for Different Sequences of Oxidant/Substrate Addition.

Entry	Addition Order	$-k_{obs}$ [$PhCO_3{}^tBu$]
1	1.) $PhCO_3{}^tBu$; 2.) NPr_3	7.6 ± 0.1
2	1.) NPr_3; 2.) $PhCO_3{}^tBu$	99.0 ± 0.1

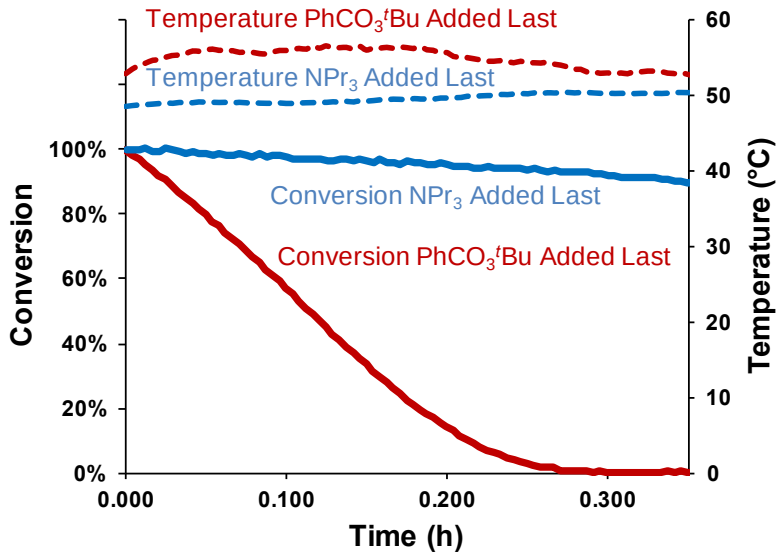

Figure S20. Decrease of [$PhCO_3{}^tBu$] versus Time and Development of Reaction Temperature versus Time for Different Sequences of Oxidation/Substrate Addition.

Procedure for Eyring Study

By analogy with the general procedure for method of initial rates, $FeCl_3 \cdot 6H_2O$ (34 mg, 125 μmol, 5.0 mol %), picolinic acid (15 mg, 125 μmol, 5.0 mol %), pyridine (15 mL), and then deionized H_2O (406 μL, 406 mg, 22.5 mmol, 9 eq.) were added to a 20 mL scintillation vial equipped with a microstirbar. The reaction mixture was heated (Table S12) on a pre-heated vial plate and vigorously stirred (1500 rpm). The ReactIR15 probe (see Materials and Methods) was inserted into the reaction vial and IR analysis was initiated. Subsequently, preheated $PhCO_3{}^tBu$ (1.4 mL, 1.5 g, 7.5 mmol) and then preheated NPr_3 (476 μL, 358 mg, 2.5 mmol) were added to the reaction.

IR analysis was conducted to generate the reaction process traces shown below; temperature was recorded in addition to IR absorption (Figure S21). $-k_{obs}$ $[PhCO_3{}^tBu]$ was determined by determining the maximum slope of the reaction trace after the initiation period. The studies were repeated at least twice and the average values of $-k_{obs}$ $[PhCO_3{}^tBu]$ as well as the obtained standard deviations are tabulated in Table S12.

Based on the obtained data, an Eyring plot (Figure S22) was constructed, plotting $\ln(k_{obs}/T)$ against 1/T. The slope and intercept were used to calculate the activation enthalpy of the reaction ($\Delta H^{\ddagger}$ = +14.1 kcal/mol) and the activation entropy ($\Delta S^{\ddagger}$ = -10.8 cal/(K mol)).

Table S12. Maximum Initial Reaction Rates in Dependence on Reaction Temperature.

Entry	Temp (ºC)	$-k_{obs}$ $[PhCO_3{}^tBu]$
1	40	4.6 ± 0.1
2	50	7.6 ± 0.1
3	60	17.5 ± 0.1
4	70	35.3 ± 0.1

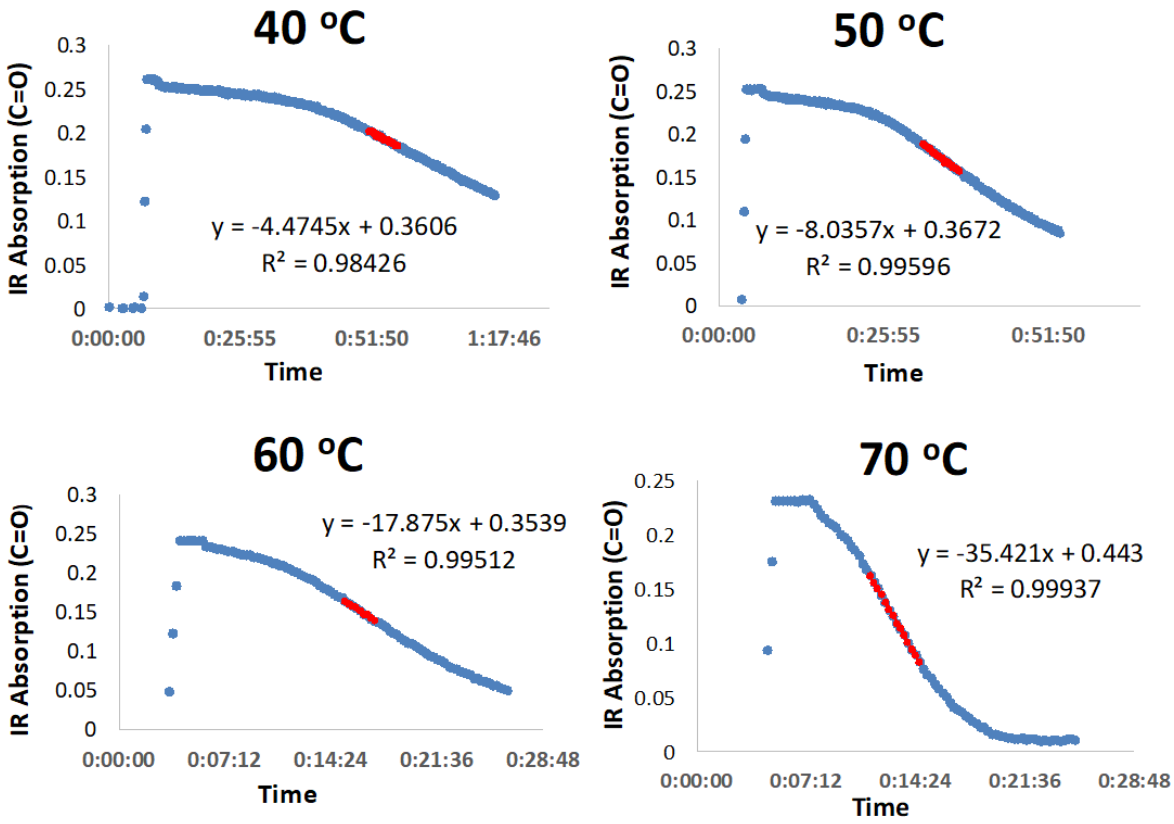

Figure S21. Decrease of [$PhCO_3{}^tBu$] versus Time for NPr_3 Oxidation at Different Temperatures.

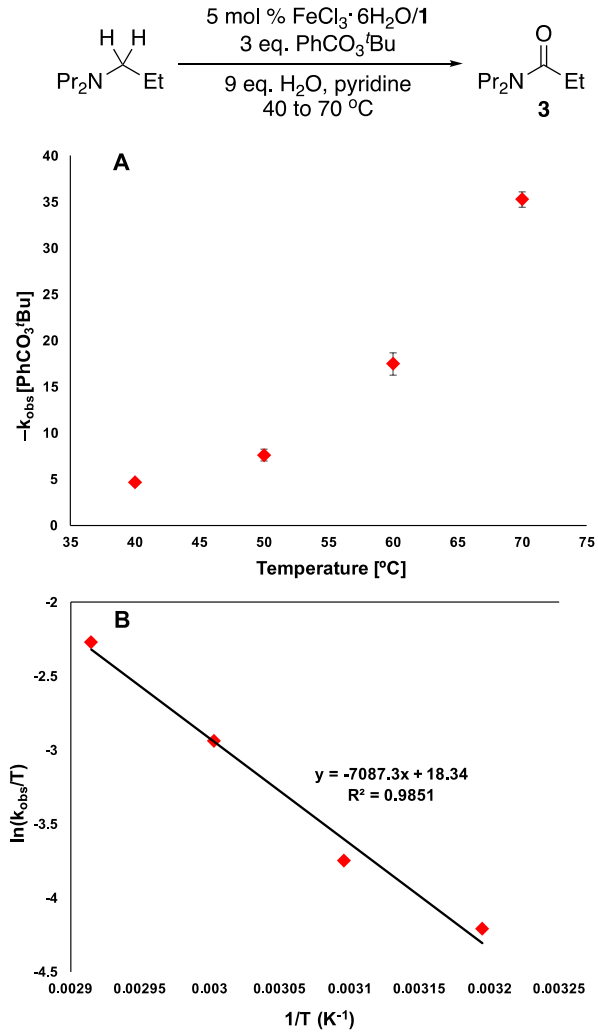

$$\ln\frac{k}{T} = -\frac{\Delta H^{\ddagger}}{R}\cdot\frac{1}{T} + \ln\frac{k_B}{h} + \frac{\Delta S^{\ddagger}}{R}$$

Figure S22. Plot of Initial Rate -k_{obs}[$PhCO_3{}^tBu$] vs. T (top), Resulting Eyring Plot of ln(k_{obs}/T) vs. 1/T (middle), and Eyring Equation (bottom).

Procedure for Hammett Study

By analogy with the general procedure for method of initial rates, $FeCl_3 \cdot 6H_2O$ (34 mg, 125 μmol, 5.0 mol %), picolinic acid (15 mg, 125 μmol, 5.0 mol %), pyridine (15 mL, see Table S13), and then deionized H_2O (406 μL, 406 mg, 22.5 mmol, 9 eq.) were added to a 20 mL scintillation vial equipped with a microstirbar. The reaction mixture was heated on a pre-heated vial plate and vigorously stirred (1500 rpm). The ReactIR15 probe (see Materials and Methods) was inserted into the reaction vial and IR analysis was initiated. Subsequently, preheated $PhCO_3{}^tBu$ (1.4 mL, 1.5 g, 7.5 mmol) and then preheated NPr_3 (476 μL, 358 mg, 2.5 mmol) were added to the reaction.

IR analysis was conducted to generate the reaction process traces shown below. $-k_{obs}$ $[PhCO_3{}^tBu]$ was determined by determining the maximum slope of the reaction trace after the initiation period. The studies were repeated at least twice and the average values of $-k_{obs}$ $[PhCO_3{}^tBu]$ as well as the obtained standard deviations are tabulated in Table S13.

Table S13. Maximum Initial Reaction Rates in Dependence on Pyridine-Type Solvent.

Entry	Solvent	Hammett Constant [3]	$-k_{obs}$ $[PhCO_3{}^tBu]$
1	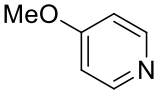	-0.27 (σ_p)	2.2 ± 0.1
2	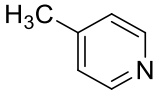	-0.17 (σ_p)	3.7 ± 0.1
3		0.0 (σ_p)	7.6 ± 0.6
4	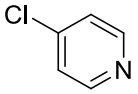	+0.23 (σ_p)	6.0 ± 0.1
5	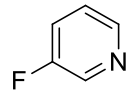	+0.34 (σ_m)	5.6 ± 0.4
6	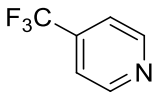	+0.54 (σ_p)	2.2 ± 0.7

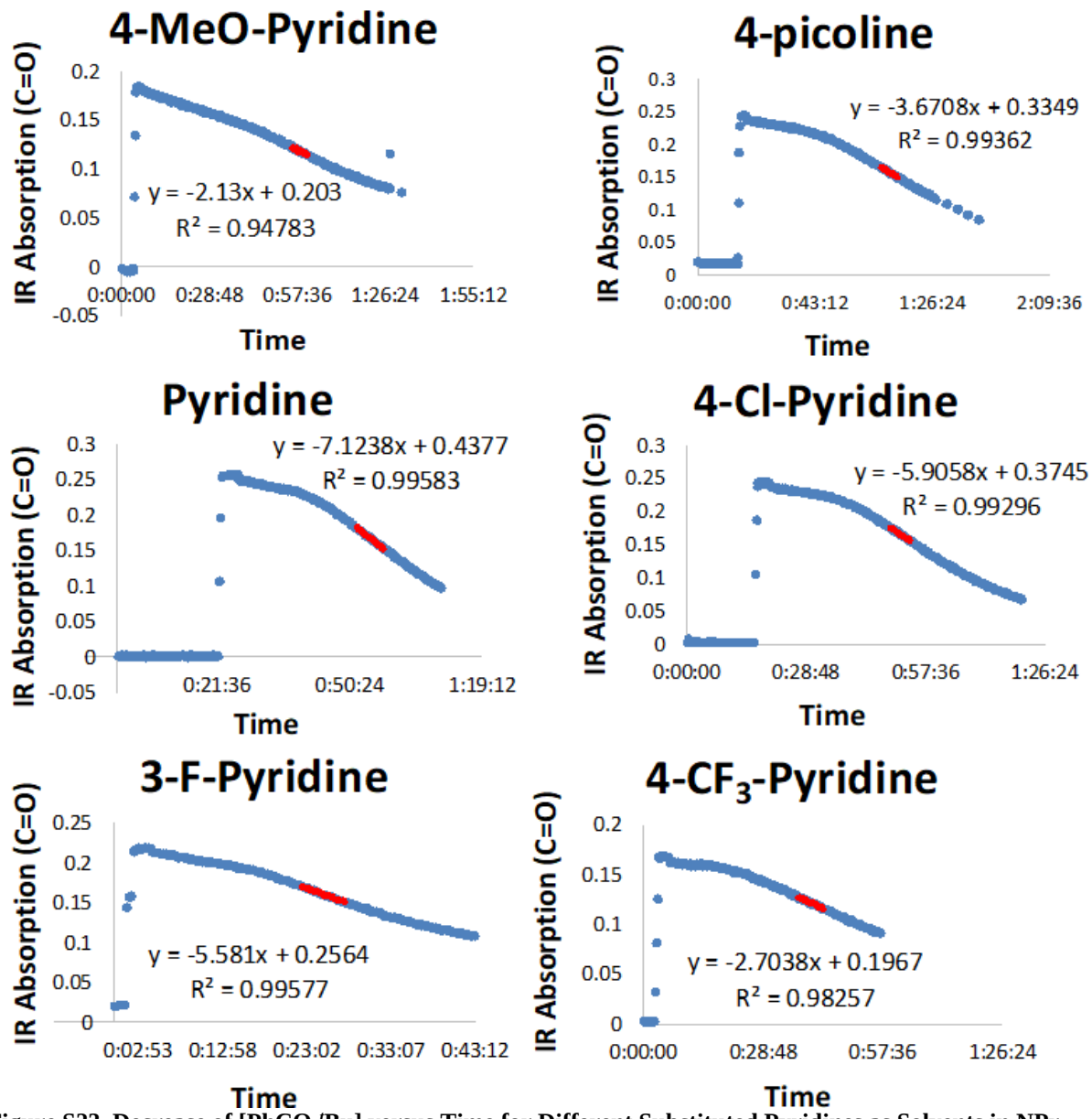

Figure S23. Decrease of [$PhCO_3{}^tBu$] versus Time for Different Substituted Pyridines as Solvents in NPr_3 Oxidation.

Procedures for Fe Coordination Studies

Reaction of 2-Picolinic Acid With $FeCl_3 \cdot 6H_2O$ in Pyridine

To a 20 mL scintillation vial equipped with a Teflon-coated stirbar, $FeCl_3 \cdot 6H_2O$ (270 mg, 1.0 mmol) and 12 mL pyridine were added. The solution was vigorously stirred (1500 rpm) at 25 °C. The ReactIR15 probe (see Materials and Methods) was inserted into the reaction vial and IR analysis was initiated. Subsequently, 250 μL aliquots (equivalent to 0.5 mmol, 0.5 equiv. 2-picolinic acid) of a standard solution of 2-picolinic acid (2.46 g, 20.0 mmol) in 10 mL pyridine were sequentially added in approximately 3 min. intervals (up to 4.5 equivalents). The spectra were generated using the ConcIRT function of the iC IR software (Figure S24).

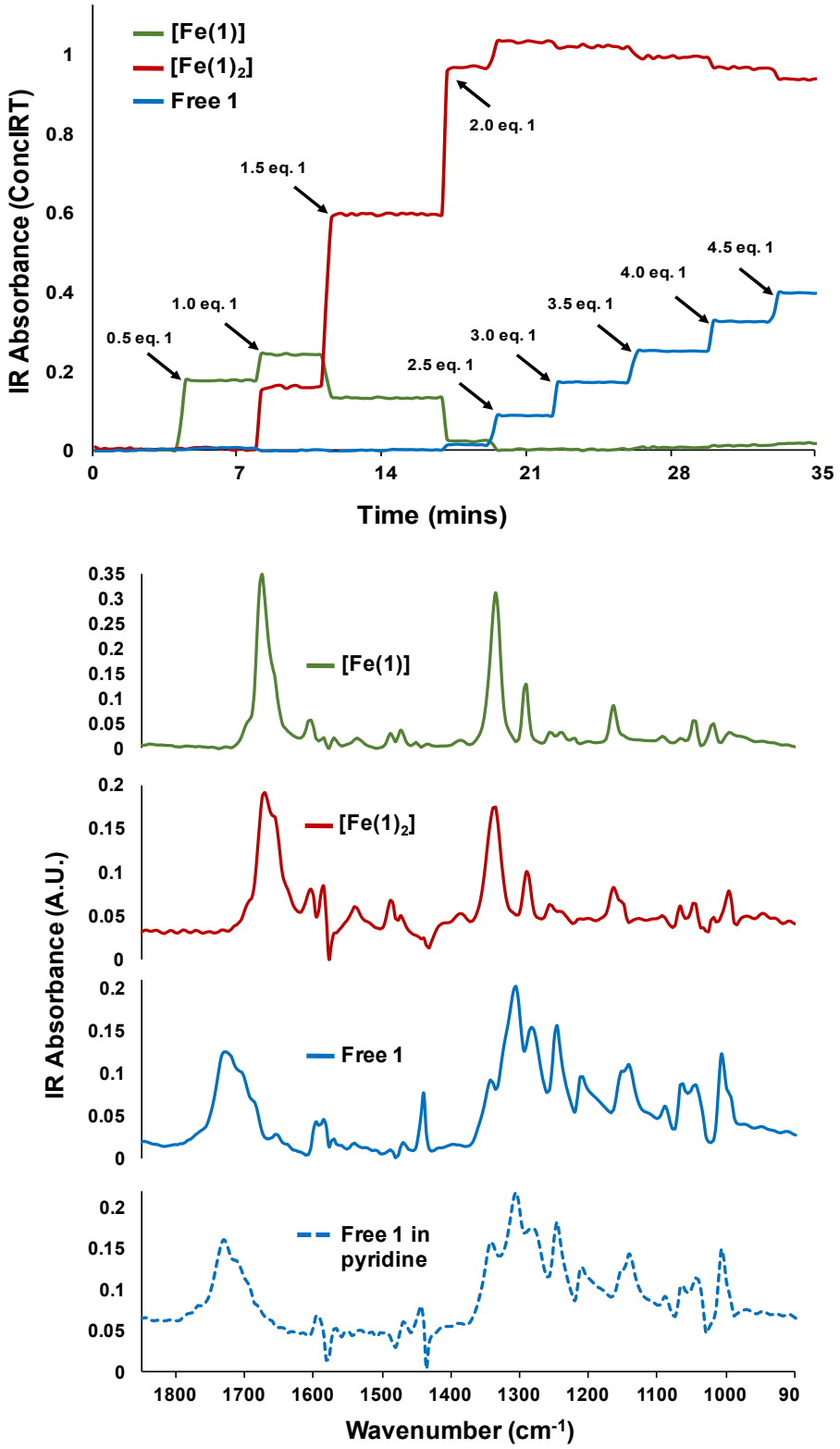

Figure S24: *in-situ* FTIR spectra (bottom) and Progression of Spectra Appearance for the Titration of Picolinic Acid into $FeCl_3$ in Pyridine.

Background Reaction of Hydrochloric Acid With $FeCl_3 \cdot 6H_2O$ in Pyridine

To a 20 mL scintillation vial equipped with a Teflon-coated stirbar, $FeCl_3 \cdot 6H_2O$ (270 mg, 1.0 mmol) and 12 mL pyridine were added and vigorously stirred (1500 rpm) at 25 °C. The ReactIR15 probe (see Materials and Methods) was inserted into the reaction vial and IR analysis was initiated. Subsequently, 15 μL aliquots of hydrochloric acid (37% w/w, 18 mg, 0.5 mmol) were sequentially added (up to 2 equiv.) in approximately 3 min. intervals (see Figure S25). Finally, 2 equiv. aliquots of picolinic acid (**1**; 246 mg, 2.00 mmol) were added (up to 4 equiv). The spectra were generated using the ConcIRT function of the iC IR software.

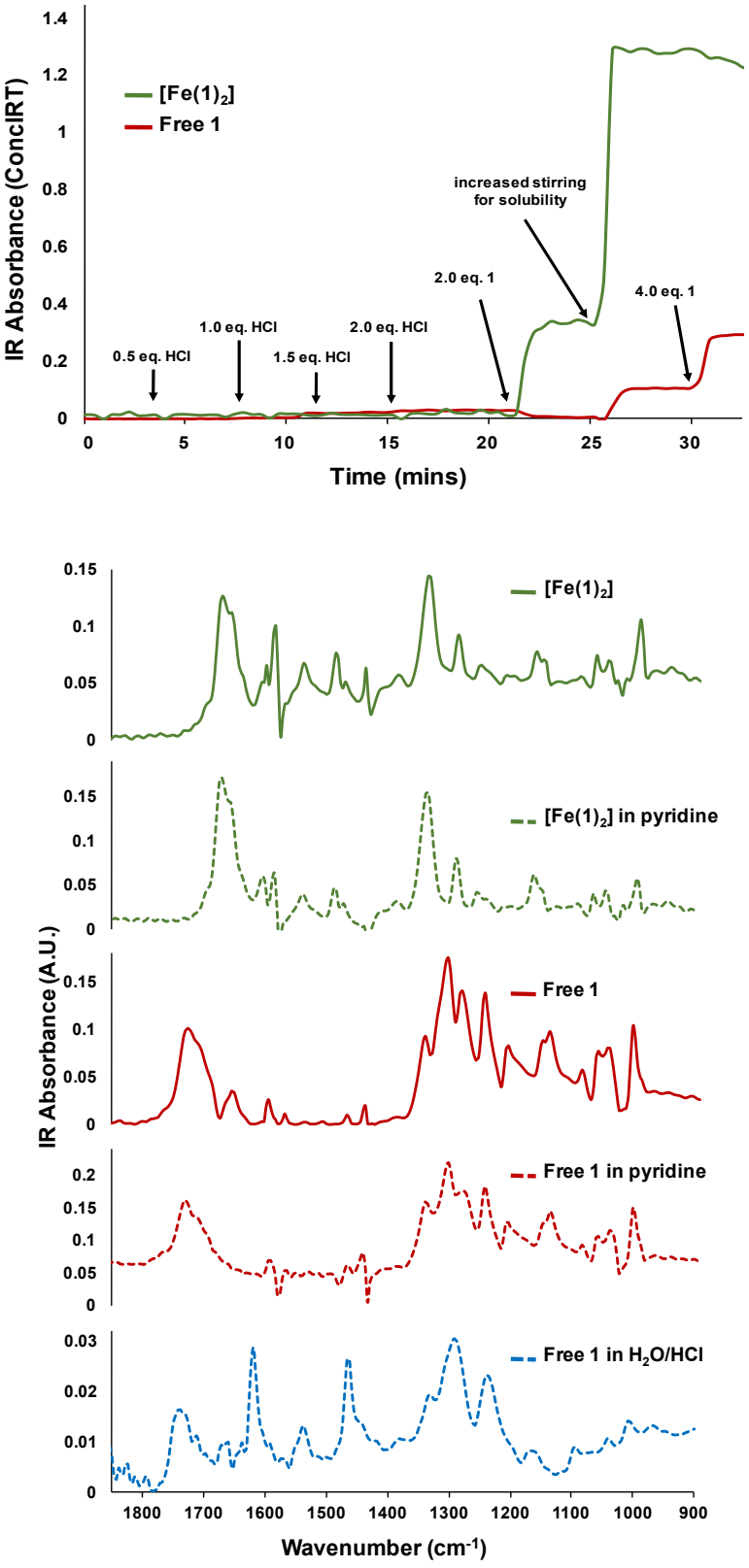

Figure S25: *in-situ* FTIR spectra (bottom) and Progression of Spectra Appearance for the Titration of HCl into $FeCl_3$ Solution in Pyridine, Followed by Picolinic Acid (1) Addition.

Reaction of $FeCl_3 \cdot 6H_2O$ with Pyridine in H_2O

To a 20 mL scintillation vial equipped with a Teflon-coated stirbar, pyridine (81 µL, 79 mg, 1.0 mmol, 1.0 equiv.) and 12 mL deionized H_2O were added. The solution was vigorously stirred (1500 rpm) at 25 °C. The ReactIR15 probe (see Materials and Methods) was inserted into the reaction vial and IR analysis was initiated. Subsequently, 250 µL aliquots (equivalent to 0.33 mmol, 0.11 equiv. $FeCl_3 \cdot 6H_2O$) of a standard solution of $FeCl_3 \cdot 6H_2O$ (1.19 g, 4.4 mmol) in 10 mL deionized H_2O were sequentially added in approximately 2 min. intervals (up to 0.99 equivs.). The resulting FTIR spectra and time course of the spectra upon pyridine additions were generated using the ConcIRT function of the iC IR software.

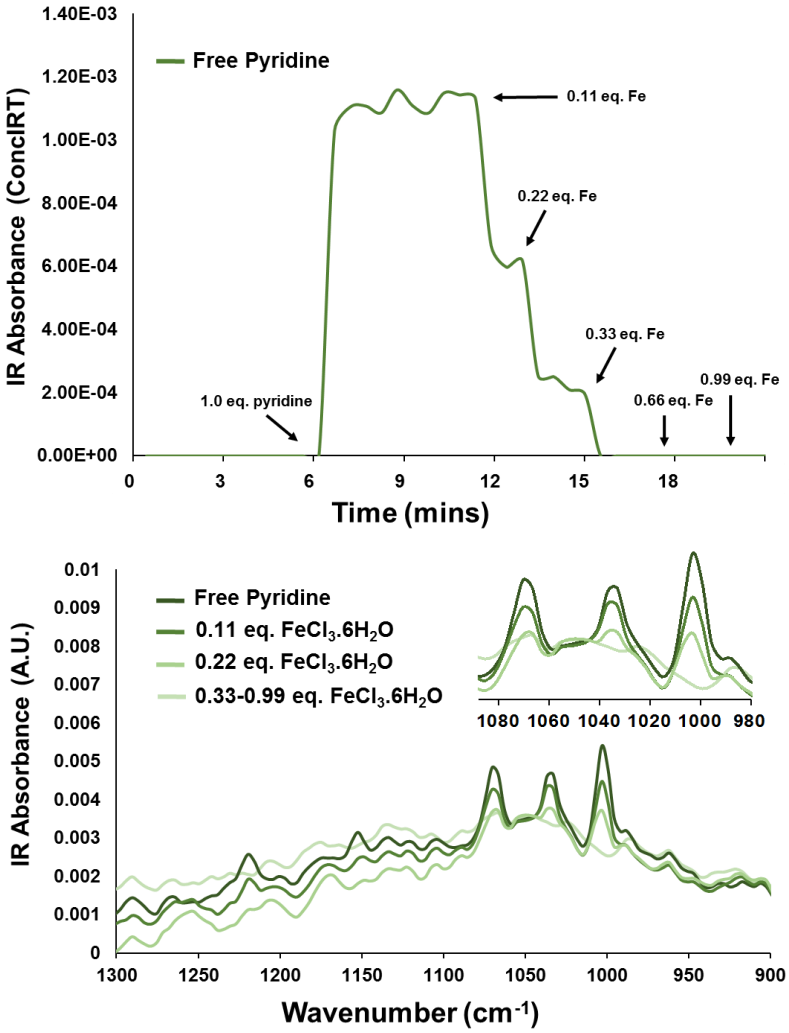

Figure S26: *in-situ* FTIR spectra (bottom) and Progression of Spectra for the Titration of Aliquots of a $FeCl_3$-Solution in H_2O into a Solution of Pyridine in H_2O.

Background Reaction of HCl with Pyridine in H_2O

To a 20 mL scintillation vial equipped with a Teflon-coated stirbar, pyridine (81 μL, 79 mg, 1.0 mmol, 3 equiv.) and 12 mL deionized H_2O were added. The solution was vigorously stirred (1500 rpm) at 25 °C. The ReactIR15 probe (see Materials and Methods) was inserted into the reaction vial and IR analysis was initiated. Subsequently, 8.0 μL aliquots of hydrochloric acid (37% w/w, 7.8 mg, 0.3 mmol) were sequentially added (up to 1.7 equiv) in intervals of approximately 2 minutes. The spectra were generated using the ConcIRT function of the iC IR software.

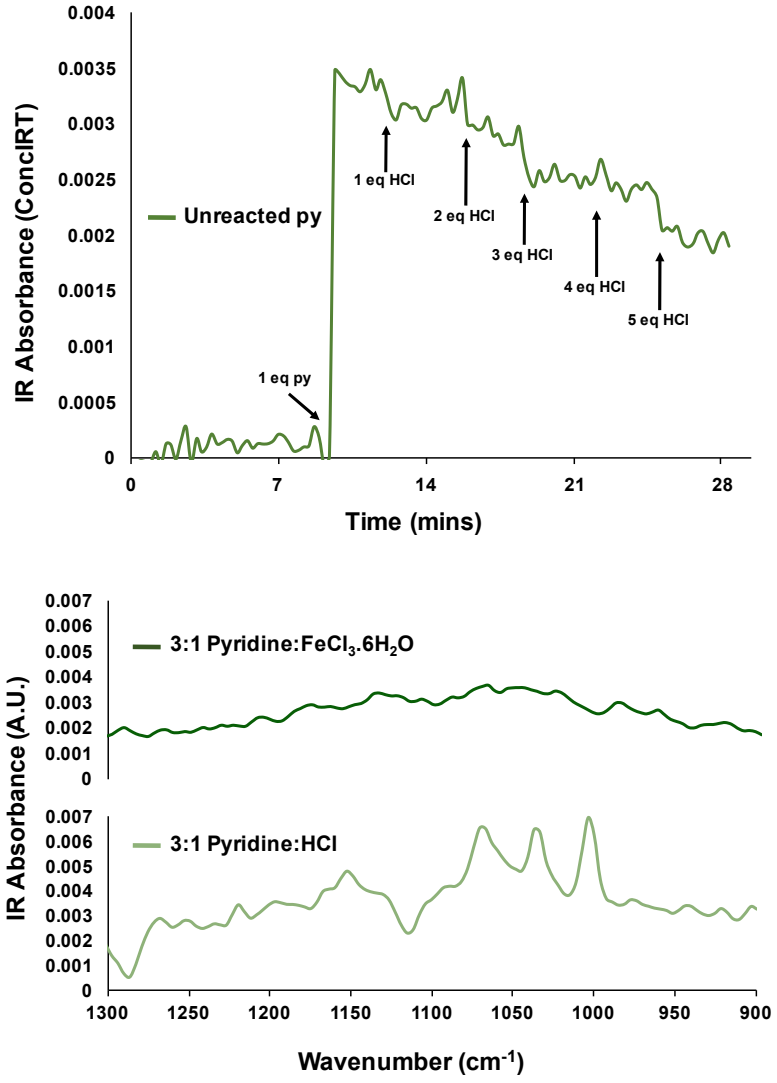

Figure S27: IR Absorbance for the Titration of HCl into Pyridine in Water.

Reaction of NPr_3 with $FeCl_3 \cdot 6H_2O$/2-Picolinic Acid (1:1) in Pyridine

To a 20 mL scintillation vial equipped with a Teflon-coated stirbar, $FeCl_3 \cdot 6H_2O$ (270 mg, 1.0 mmol), picolinic acid (123 mg, 1.0 mmol) and 20 mL pyridine were added. The solution was vigorously stirred (1500 rpm) at 25 °C. The ReactIR15 probe (see Materials and Methods) was inserted into the reaction vial and IR analysis was initiated. Subsequently, 95 μL aliquots (72 mg, 0.5 mmol, 0.5 equiv.) of NPr_3 were sequentially added in approximately 3 min. intervals (up to 5.0 equivs., see Figure S28, top). The spectra shown in Figure S28 (bottom) were generated using the ConcIRT function of the iC IR software.

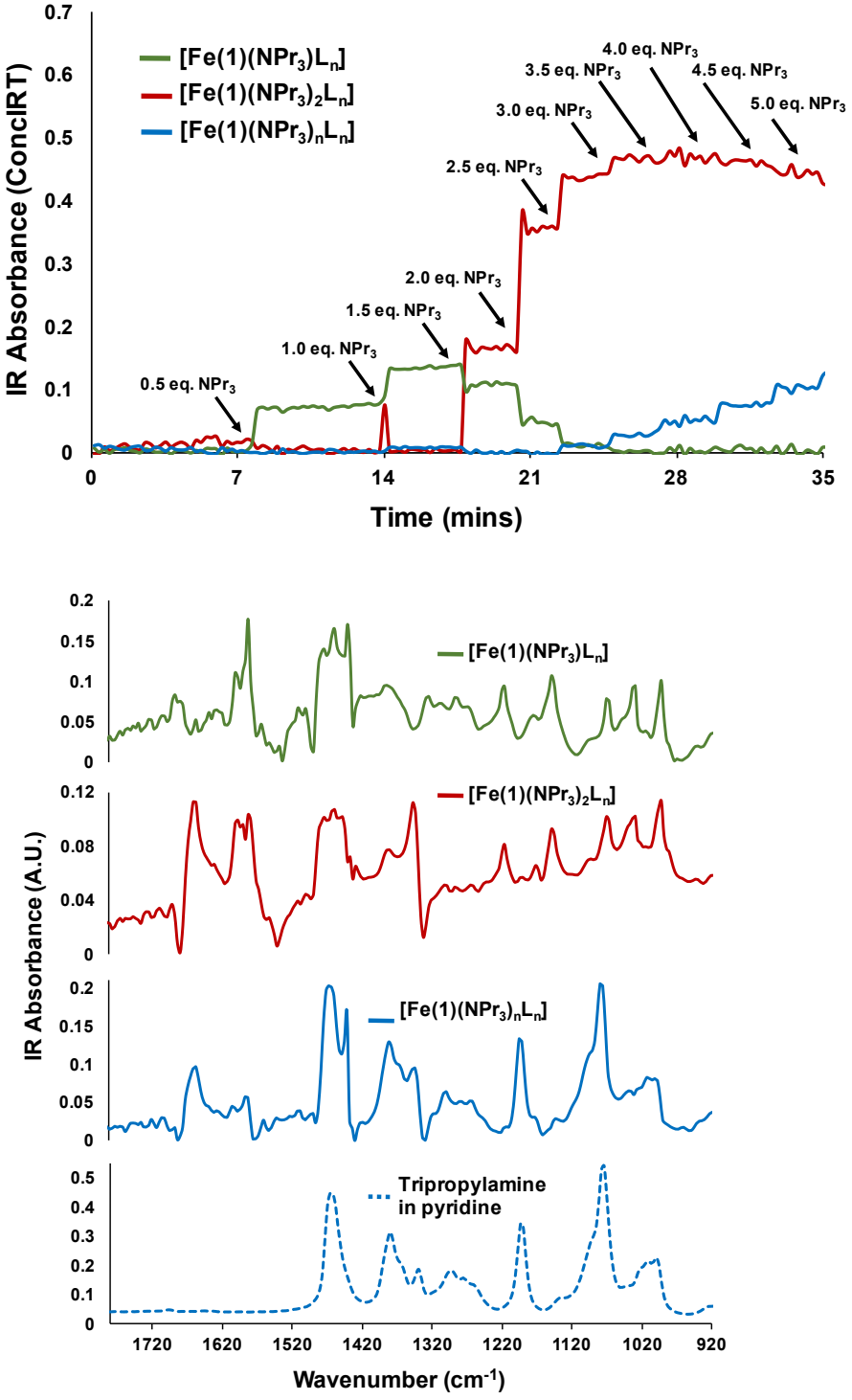

Figure S28: IR Absorbance for the Titration of NPr_3 into $FeCl_3$/Picolinic Acid (1:1) Pyridine.

Catalytic Relevance of 2-Picolinic Acid: Monitoring the Reaction Mixture for Catalytic Turnover Upon Addition of Reagents

By analogy with the general procedure for method of initial rates, $PhCO_3{}^tBu$ (1.4 mL, 1.5 g, 7.5 mmol) and pyridine (15 mL) were added to a 20 mL scintillation vial equipped with a microstirbar. The reaction mixture was heated to 50 °C on a pre-heated vial plate and vigorously stirred (1500 rpm). The ReactIR15 probe (see Materials and Methods) was inserted into the reaction vial and IR analysis was initiated. Subsequently, the following reagents were preheated to 50 °C and added, in order, in approximately 15 min. intervals (see Figure S29): (1) NPr_3 (476 µL, 358 mg, 2.5 mmol; 1.0 eq.); (2) deionized H_2O (406 µL, 406 mg, 22.5 mmol, 9 eq.); (3) $FeCl_3{\cdot}6H_2O$ (34 mg, 125 µmol, 5.0 mol %); and finally (4) picolinic acid (**1**; 15 mg, 125 µmol, 5.0 mol %). IR analysis was conducted for to generate the kinetic traces shown in Figure S29. The corresponding IR spectra generated by the Mettler Toledo iC IR software are shown in Figure S30.

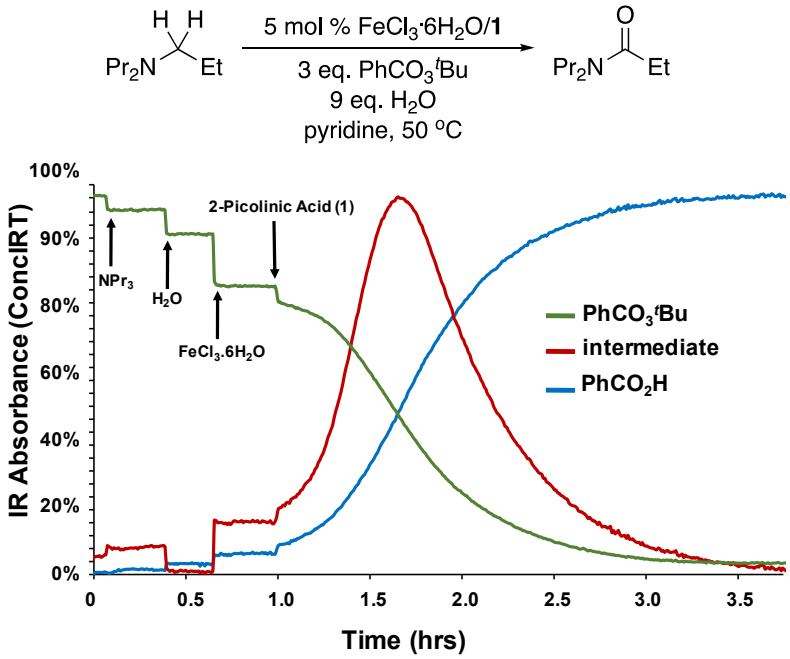

Figure S29: IR Absorbance for the Sequential Addition of Reagents in Fe-Catalyzed NPr_3 Oxidation.

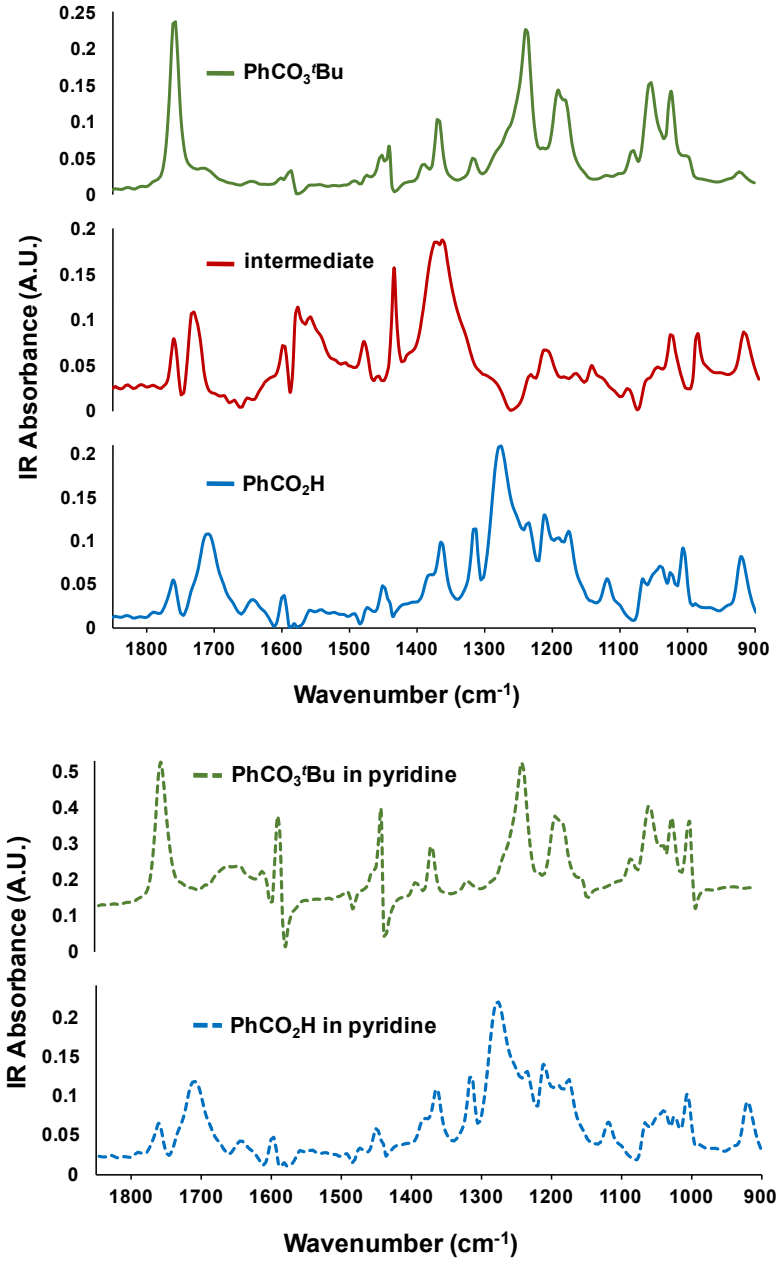

Figure S30. Top: IR Spectra generated via ConcertIR for $PhCO_3{}^tBu$ (green), Intermediate (red), and $PhCO_2H$ (blue), as obtained from measurements in Figure S29. Bottom: Comparison Spectra of $PhCO_3{}^tBu$ (green) and $PhCO_2H$ (blue), as measured independently in pyridine/H_2O (15 mL/406 µL) solvent mixture.

Probing Coordination of $PhCO_3{}^tBu$ To Catalyst Precursor ($FeCl_3 \cdot 6H_2O$/Picolinic Acid) in Pyridine/H_2O at Room Temperature

To a 20 mL scintillation vial equipped with a Teflon-coated stirbar, $FeCl_3 \cdot 6H_2O$ (270 mg, 1.0 mmol, 1 equiv.), picolinic acid (123 mg, 1.0 mmol, 1 equiv.), deionized H_2O (162 μL, 162 mg, 9.0 mmol, 9 eq.) and 15 mL pyridine were added at room temperature. The solution was vigorously stirred (1500 rpm) at 25 °C. The ReactIR15 probe (see Materials and Methods) was inserted into the reaction vial and IR analysis was initiated. Subsequently, 47 μL aliquots (49 mg, 250 μmol, 0.25 equiv.) of $PhCO_3{}^tBu$ were sequentially added in approximately 2 min. intervals (up to 3.5 equivs.). Finally, 187 μL aliquots (194 mg, 1.0 mmol, 1.0 equiv.) of $PhCO_3{}^tBu$ were sequentially added in approximately 2 min. intervals (up to 5.5 total equivs.). The spectra were generated using the ConcIRT function of the iC IR software.

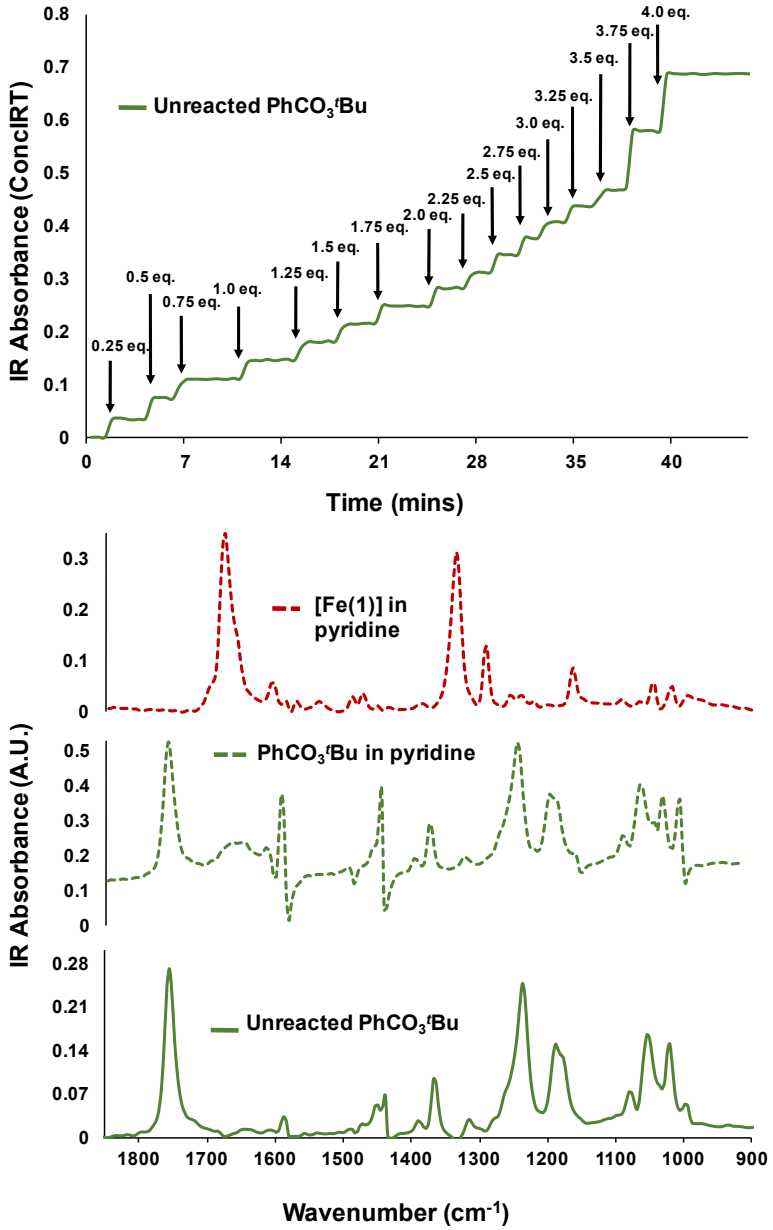

Figure S31. IR Absorbance for the Titration of $PhCO_3{}^tBu$ into $FeCl_3$/Picolinic Acid (1:1) Pyridine.

Probing Coordination of $PhCO_3{}^tBu$ To Catalyst Precursor ($FeCl_3 \cdot 6H_2O$/Picolinic Acid) in Pyridine/H_2O at 50 °C

To a 20 mL scintillation vial equipped with a Teflon-coated stirbar, $PhCO_3{}^tBu$ (280 μL, 291 mg, 1.5 mmol, 1 equiv.) and 5 mL pyridine were added. The solution was vigorously stirred (1500 rpm) at 50 °C. The ReactIR15 probe (see Materials and Methods) was inserted into the reaction vial and IR analysis was initiated. Subsequently, 250 μL of a standard solution of $FeCl_3 \cdot 6H_2O$ (808 mg, 3.0 mmol) and picolinic acid (368 mg, 3.0 mmol) in 2 mL pyridine [equivalent to 375 μmol, 0.25 equiv. $FeCl_3 \cdot 6H_2O$ (101 mg)/picolinic acid (46 mg)] was added. The spectra were generated using the ConcIRT function of the iC IR software.

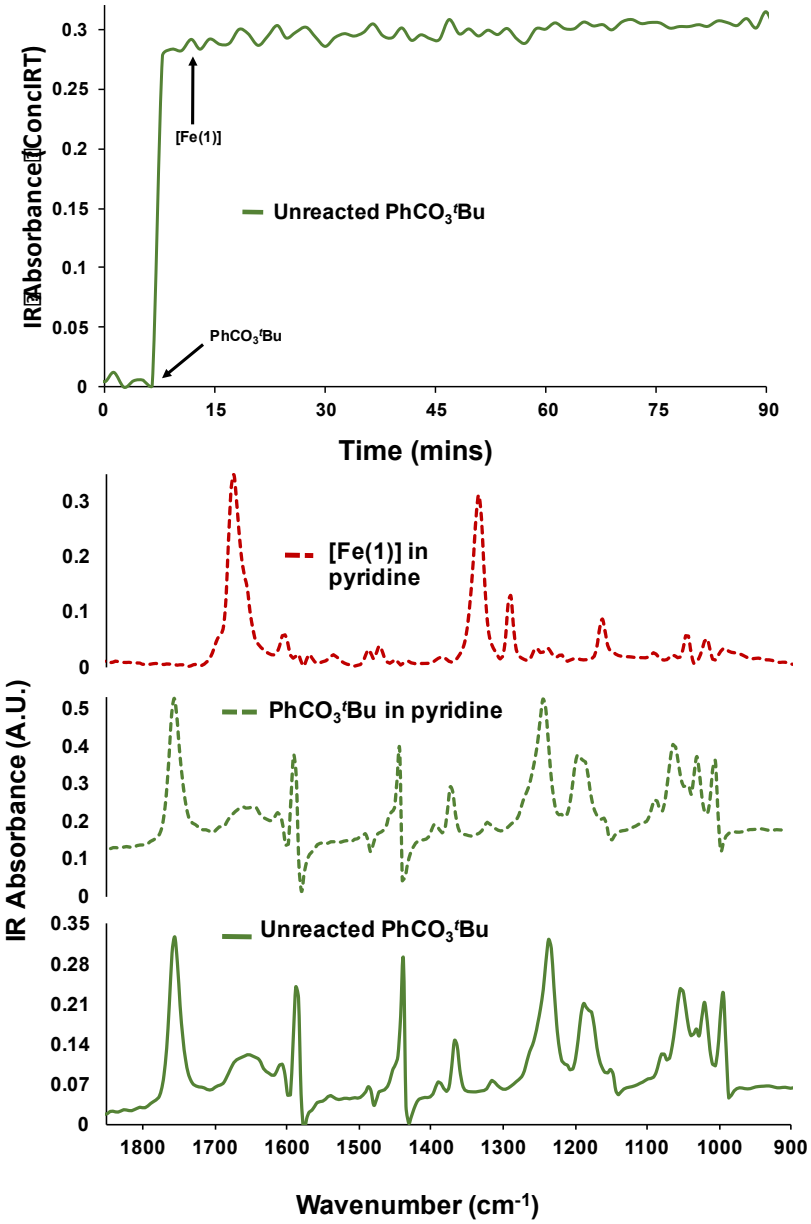

Figure S32. IR Absorbance for Reaction of $PhCO_3{}^tBu$ and $FeCl_3$/Picolinic Acid (1:1) Pyridine.

Probing Coordination of N,N-Dipropylpropionamide To Catalyst Precursor ($FeCl_3·6H_2O$/Picolinic Acid) in Pyridine/H_2O at Room Temperature

To a 20 mL scintillation vial equipped with a Teflon-coated stirbar, $FeCl_3·6H_2O$ (81 mg, 300 μmol, 1 equiv.), picolinic acid (37 mg, 300 μmol, 1 equiv.), deionized H_2O (50 μL, 50 mg, 2.7 mmol, 9 eq.) and 5 mL pyridine were added at room temperature. The solution was vigorously stirred (1500 rpm) at 25 °C. The ReactIR15 probe (see Materials and Methods) was inserted into the reaction vial and IR analysis was initiated. Subsequently, 14 μL aliquots (12 mg, 75 μmol, 0.25 equiv.) of N,N-dipropylpropionamide were sequentially added in approximately 2 min. intervals (up to 1.0 equivs.). Finally, 56 μL (48 mg, 300 μmol, 1.0 equiv.) of N,N-dipropylpropionamide was added. The spectra were generated using the ConcIRT function of the iC IR software.

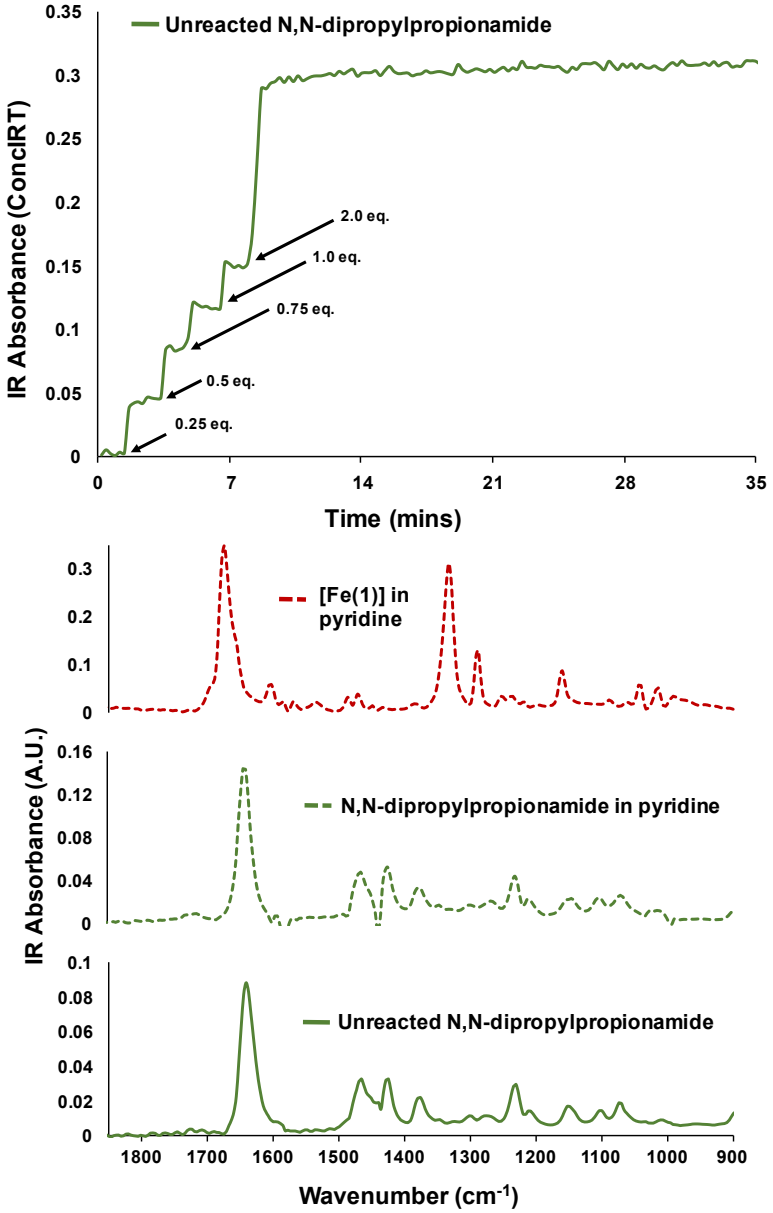

Figure S33. IR Absorbance for the Titration of N,N-dipropylpropionamide into $FeCl_3$/Picolinic Acid (1:1) Pyridine.

Kinetic Profiles of Reactions at Different Loadings of Fe/1

For the procedures to obtain the reaction profiles shown below, please see page 21, section Kinetic Order in $FeCl_3 \cdot 6H_2O$/Picolinic Acid (1:1).

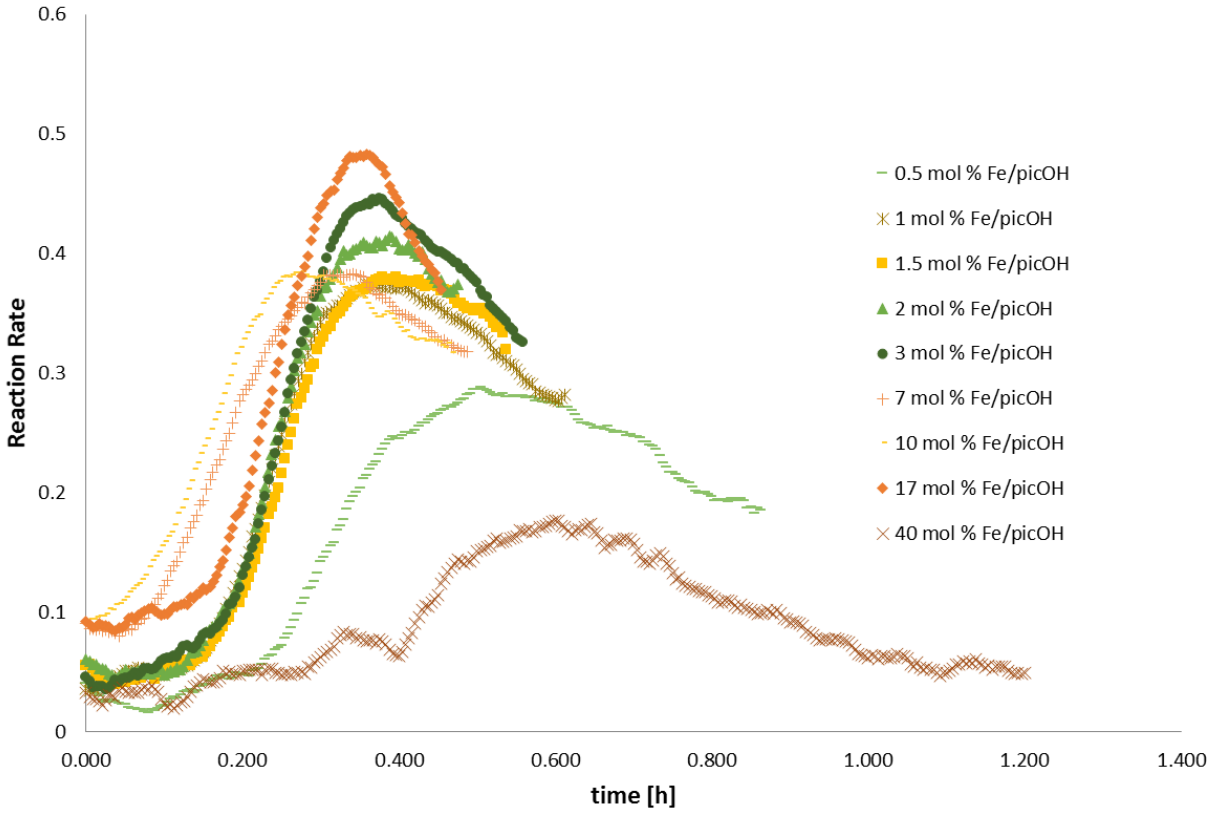

Figure S34. Dependence of Reaction Rate and Initiation Period on Catalyst Loading.

Procedure for ESI-MS Studies

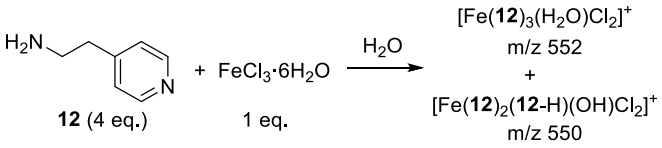

$FeCl_3 \cdot 6H_2O$ (3 mg, 10 μmol, 1 equiv.) and deionized H_2O (20 mL) were added to a 20 mL scintillation vial. The ligand 3-(pyridin-4-yl)propan-1-amine (5.5 μL, 5.5 mg, 40 μmol, 4.0 equiv.) was then added. The prepared solution was injected into a Finnigan LCQ DECA mass spectrometer (see Materials and Methods) and ESI-MS analysis was performed (negative ion mode; flow rate = 30 μL/min; capillary V = -36V; spray V = 5V).

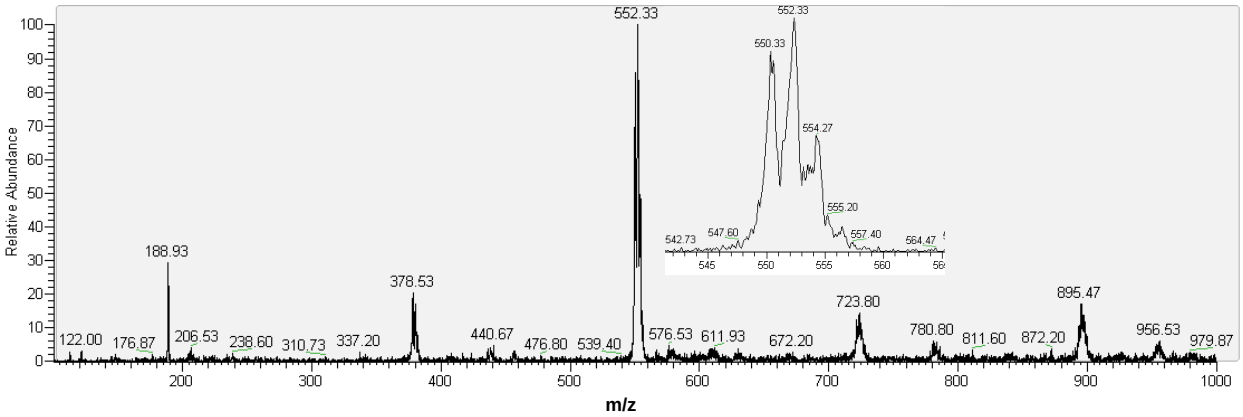

Figure S35. ESI-MS Spectrum Obtained from Spraying a Mixture of $FeCl_3 \cdot 6H_2O$ and 3-(pyridin-4-yl)propan-1-amine in deionized H_2O.

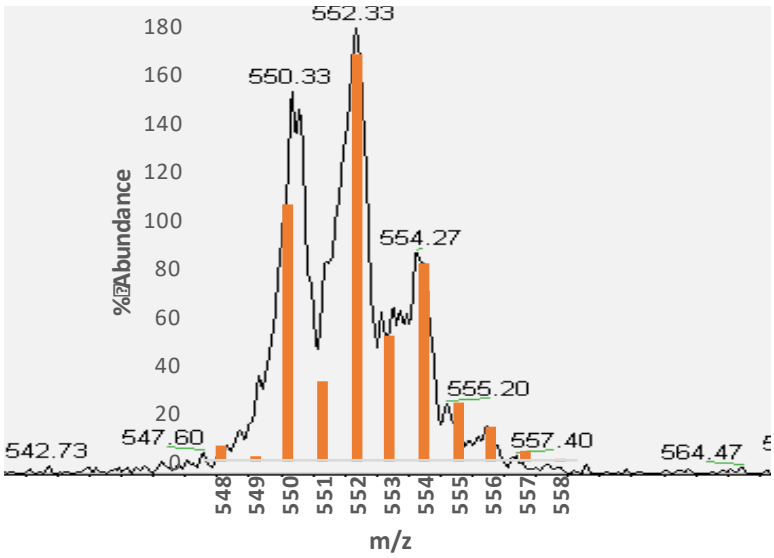

Figure S36. Overlay of MS peak at 548-558 m/z with mass prediction for complexes $FeCl_2(OH)(C_5H_4NCH_2CH_2CH_2NH_2)_2(C_5H_4NCH_2CH_2CH_2NH)$ and $FeCl_2(H_2O)(C_5H_4NCH_2CH_2CH_2NH_2)_3$. Conditions: Ligand (5.5 μL, 5.5 mg, 40 μmol, 4.0 equiv.), $FeCl_3{\cdot}6H_2O$ (3 mg, 10 μmol, 1 equiv.), H_2O (20 mL), negative ion mode, flow rate = 30 μL/min, capillary V = -36 V, spray V = 5V.

General Procedure for 2-Methyl-1-Phenylpropan-2-yl Benzoperoxoate Studies

$FeCl_3 \cdot 6H_2O$ (6.8 mg, 25 μmol, 5.0 mol %), picolinic acid (3.1 mg, 25 μmol, 5.0 mol %), pyridine (2 mL) and then deionized H_2O (81 μL, 81 mg, 4.5 mmol, 9 eq.) were added to a 4 mL scintillation vial equipped with a microstirbar. The reaction mixture was heated to 50 °C on a pre-heated vial plate and vigorously stirred (1500 rpm). Subsequently, preheated 2-Methyl-1-Phenylpropan-2-yl Benzoperoxoate (372 μL, 406 mg, 1.5 mmol) and then NPr_3 (95 μL, 71.6 mg, 500 μmol, 1.00 eq.) were added to the reaction. The reaction was stirred for 2 h and the reaction mixture was filtered through celite and activated charcoal to remove Fe. Quantitative ^{1}H NMR analysis was conducted (Figure S37).

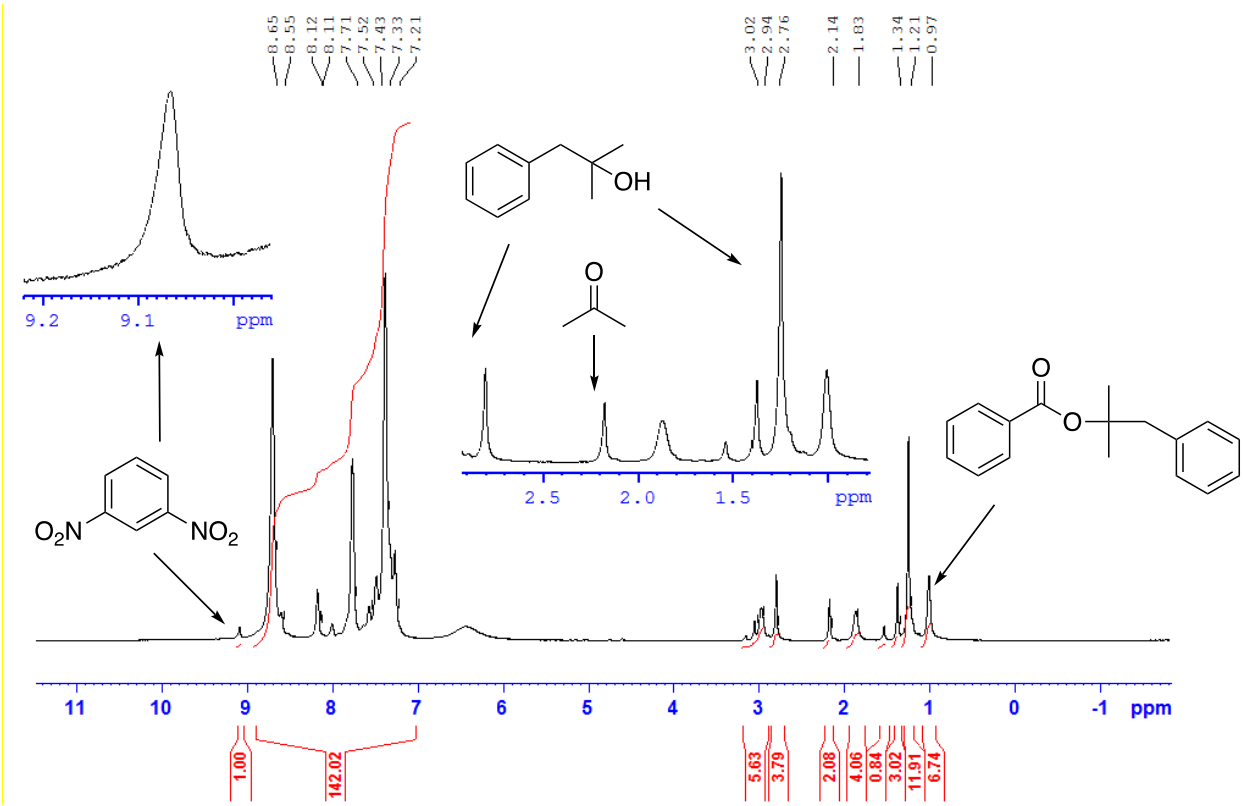

Figure S37: ^{1}H NMR spectrum of Reaction with 2-methyl-1-phenylpropan-2-yl benzoperoxoate**.**

Analogous filtration to the one conducted here had previously been shown to remove both secondary amines and other side products together with the formed amide product; therefore, Figure S37 does not show these compounds. In order to confirm that amides and and/or dealkylated amines are present in the crude reaction mixture, GCMS analysis was conducted (Figure S38).

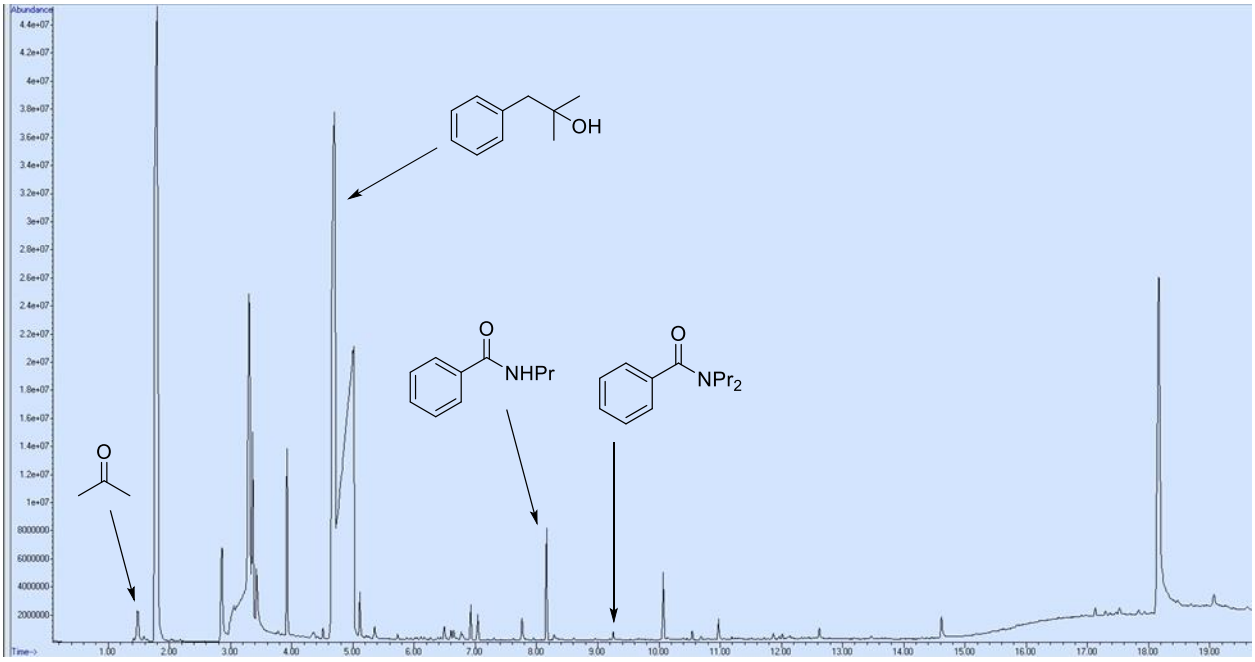

Figure S38. GCMS Chromatogram and Peak Assignments for Crude 2-methyl-1-phenylpropan-2-yl benzoperoxoate Oxidation Mixture.

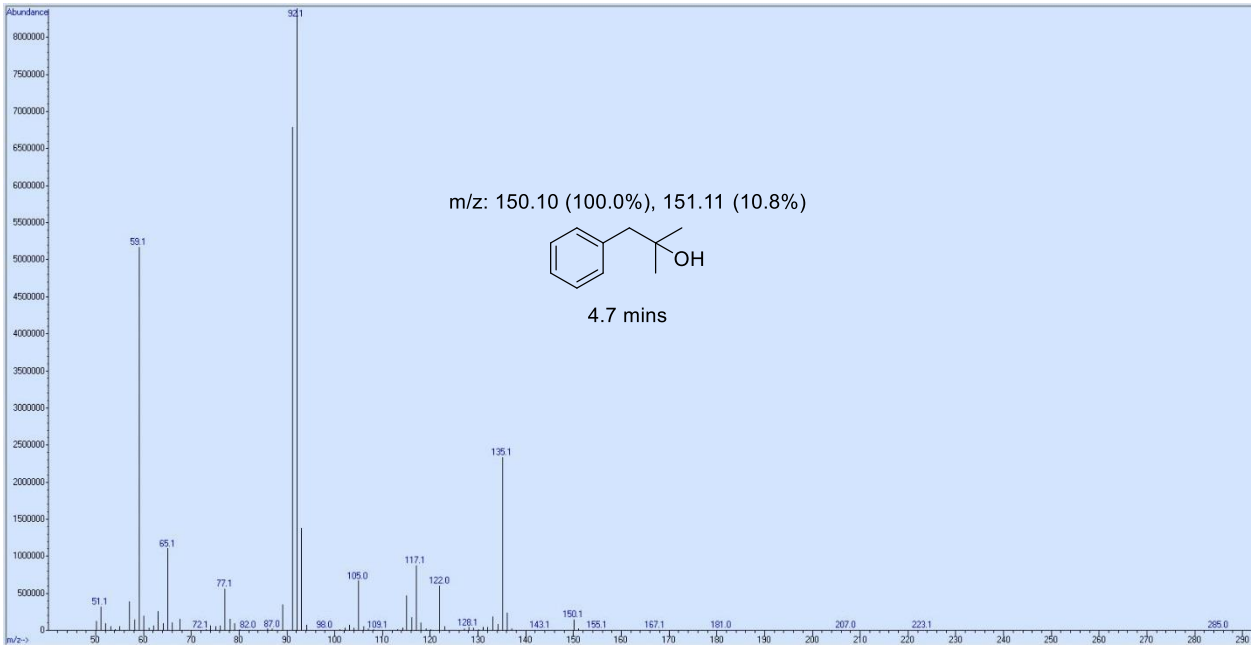

Figure S39. MS Spectrum derived from peak at 4.7 min.

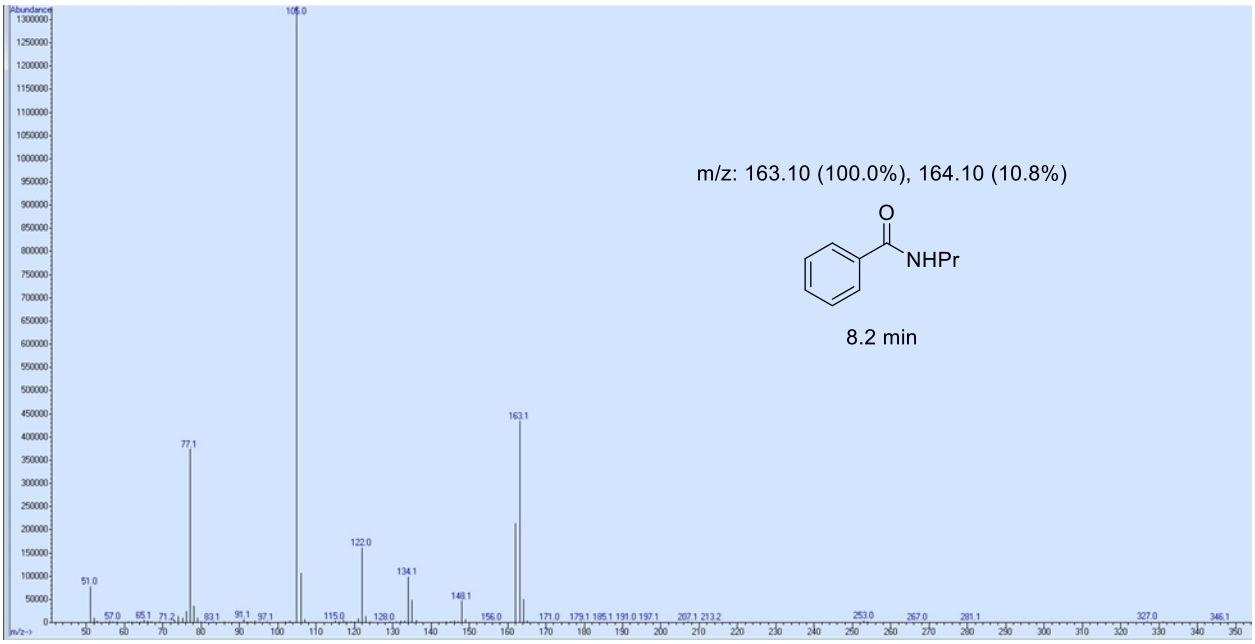

Figure S40. MS Spectrum derived from peak at 8.2 min.

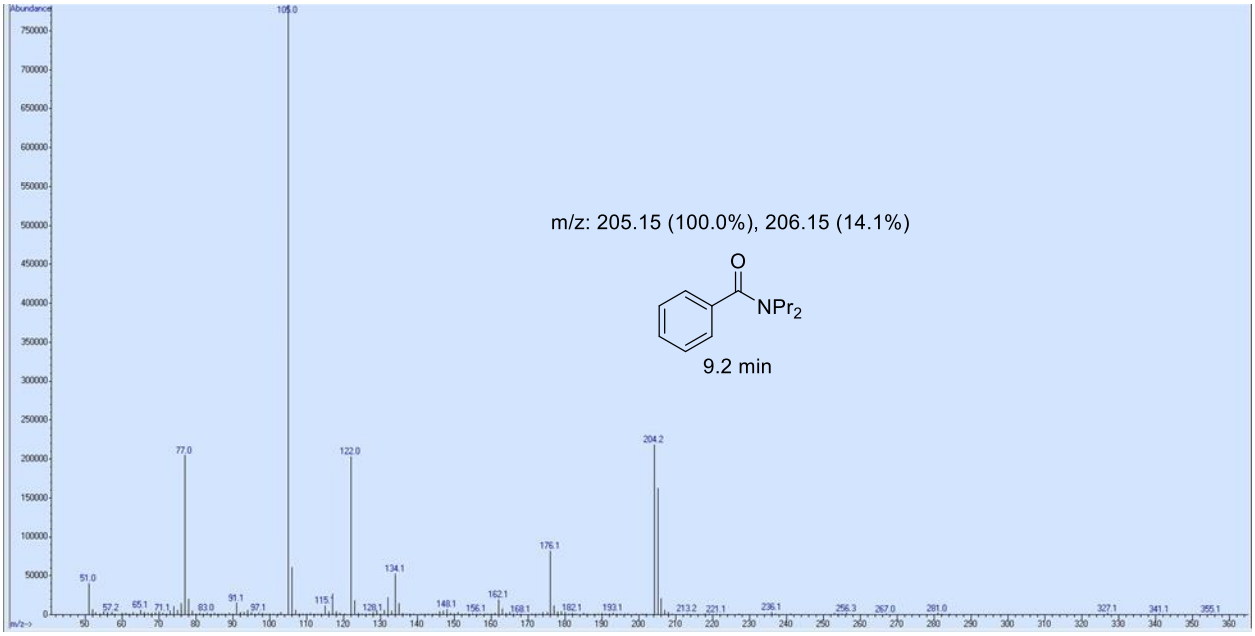

Figure S41. MS Spectrum derived from peak at 9.2 min.

EPR Studies
Studies of Free Radicals at Room Temperature

Room temperature EPR studies of liquid solutions were obtained using a microwave power of 2 mW and a modulation amplitude of 3 G after testing to ensure that there was no microwave saturation or modulation broadening of signals at these settings. The experiments showed no evidence for free radical formation in solutions containing ^{t}BuOOH or $PhCO_3{}^{t}Bu$ and other reagents (PicOH, NPr_3) in pyridine/water solutions in the absence of Fe(III). The possibility that short-lived radicals had decayed before observation was eliminated by carrying out the experiments in the presence of phenyl-*tert*-butylnitrone, PBN, when no trapped radicals were observed. However, upon the addition of Fe(III), a strong free radical signal with g = 2.0059 and ΔH_{pp} = 24 G was formed in solutions containing tBuOOH. The PBN-trapped radical (g = 2.0066, A(N) = 13.5 G, A(H) = 1.4 G) was identified as t-BuOO•[4] with a smaller amount of another trapped radical (g = 2.0065, A(N) = 13.6 G, A(H) = 2.8 G), likely tBuO• (Figure S42).

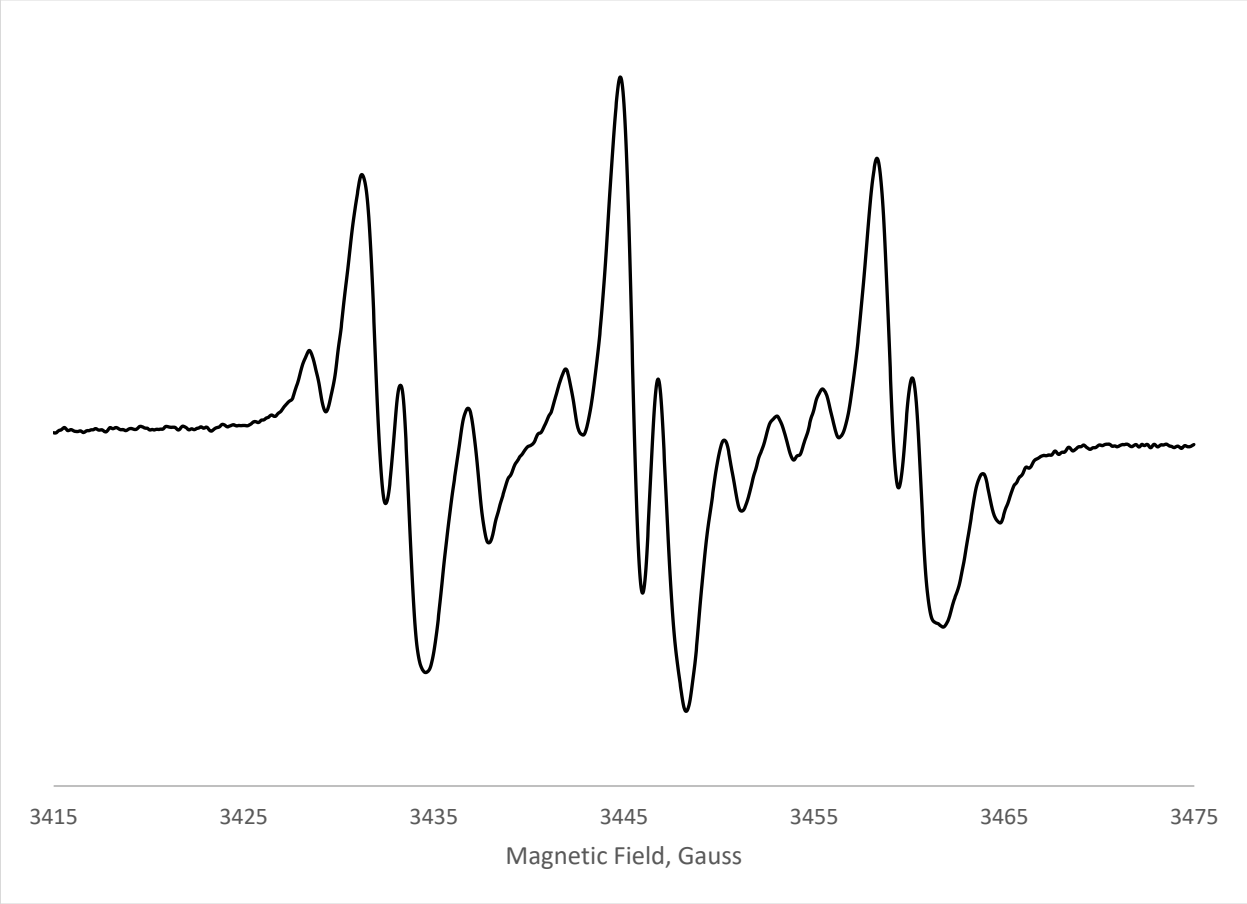

Figure S42. EPR Spectrum of PBN-trapped ^{t}BuOO• and ^{t}BuO•.

Solutions containing Fe(III) and the oxidant $PhCO_3{}^tBu$ showed no stable free radical signal in the absence of PBN, but a trapped signal with g = 2.0064, A(N) = 14.4 G, A(H) = 2.0 G, indicating a trapped alkyoxyl (RO•) radical.[4,5]

In the presence of NPr_3, the signal broadened, likely because of a change in tumbling rate (Figure S43). These results indicate a short-lived alkyloxy free radical.

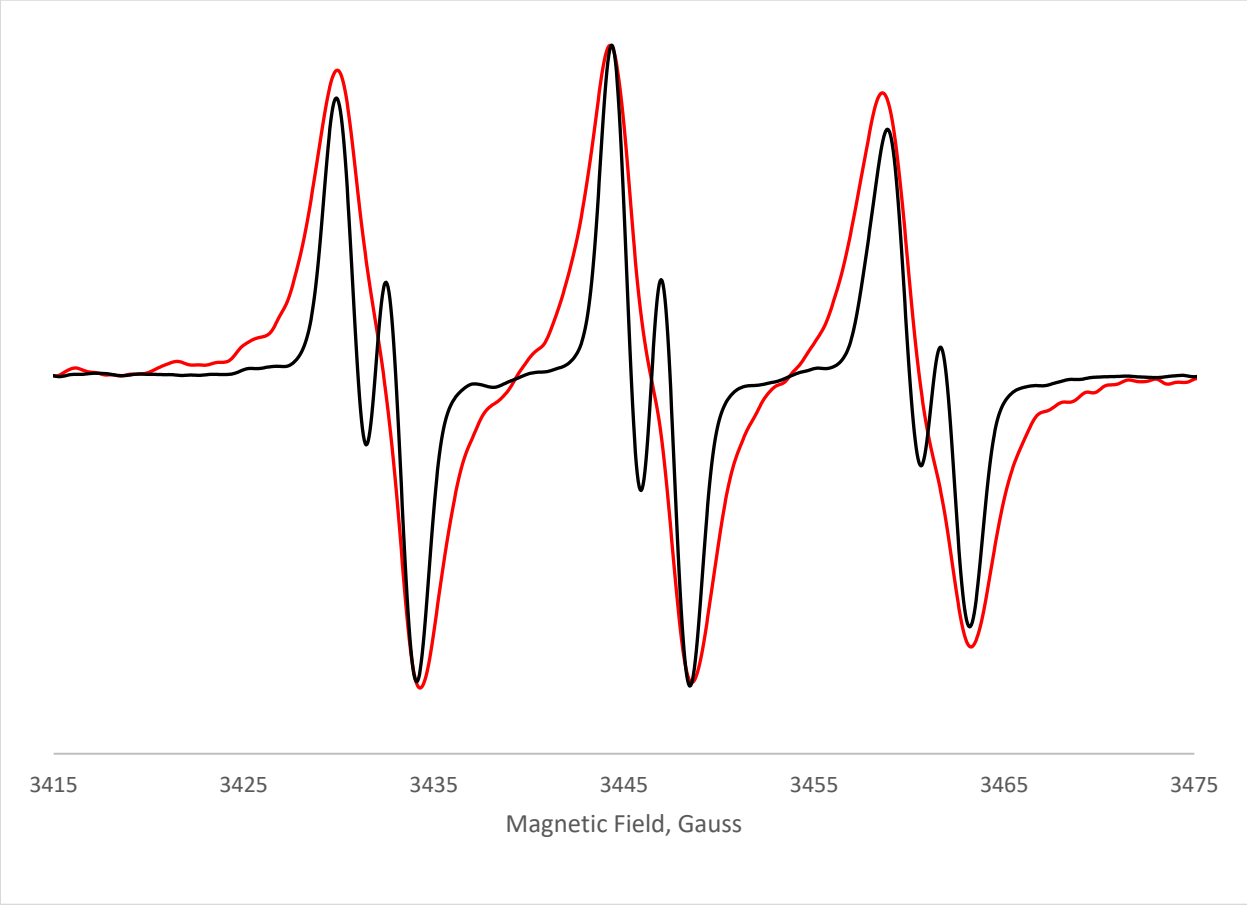

Figure S43. EPR spectra of Fe(III) TBPB in py/water with PBN. Red, with NPr_3, black, without NPr_3.

The results show that Fe(III) is required to form free radicals and that in the case of the oxidant TBPB alkyloxy but not alkylperoxy radicals are formed under the conditions of our reactions.

Studies of Iron Spin State

To investigate the spin state of the iron center, EPR experiments were recorded of solutions frozen in liquid nitrogen immediately after preparation. EPR spectra were obtained at 135 K using a microwave power of 21 mW and a modulation amplitude of 10 G.

Solutions of $FeCl_3$ in pyridine/water (150:4 v/v, corresponding to 9 equiv. H_2O) (Figure S44) show two signals, at $g \approx 4.3$ and at 2.003 with peak widths, ΔH_{pp} of ca 78 G and 23 G, respectively. The $g = 4.3$ signal is that commonly observed for "rhombic" high-spin ($S = 5/2$) Fe(III) in low symmetry sites, and was present only to the extent of about 5% of the other signal. A small amount of this form of iron was present in all EPR spectra that were obtained and likely has no significance. The $g = 2.003$ signal is due to a low-spin ($S = ½$) Fe(III) signal, likely because the Fe(III) has several pyridine ligands.

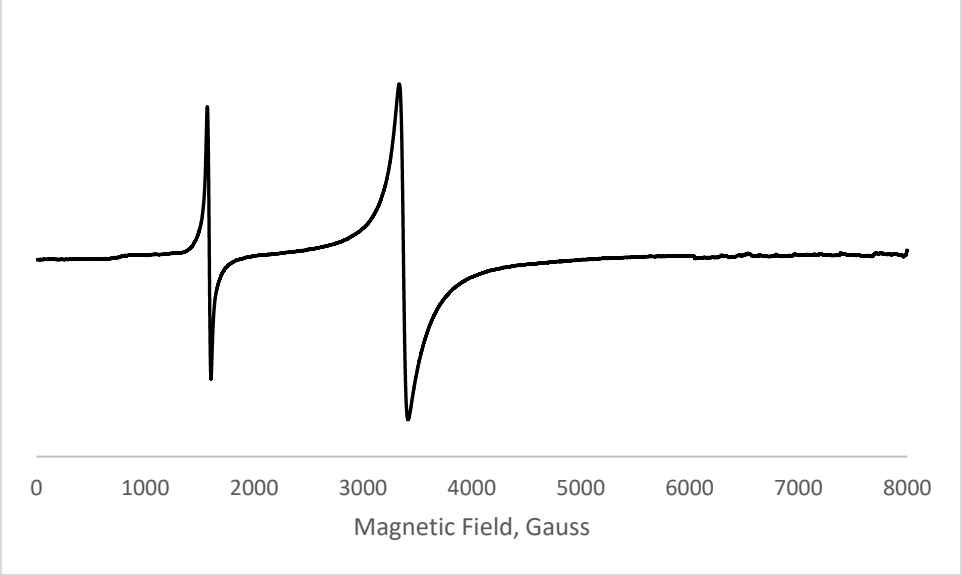

Figure S44. EPR spectra of frozen solutions of Fe(III) in 150:4 v/v pyridine-water.

Upon the addition of 2-picolinic acid to this solution to give a 1:1 molar ratio of picolinic acid to Fe(III), a small g = 2 signal remains and a new broader high-spin (S = 5/2) signal appears near g = 4.3 (in addition to the sharp "rhombic" signal, Figure S45). The results indicate that PicOH binds to the Fe(III), displacing some of the pyridine ligands resulting in a weaker ligand field, as anticipated for replacement of nitrogen ligand atoms by oxygen ligand atoms. This result supports the results of the IR titrations described on page 36, in the section Reaction of 2-Picolinic Acid With $FeCl_3 \cdot 6H_2O$ in Pyridine.

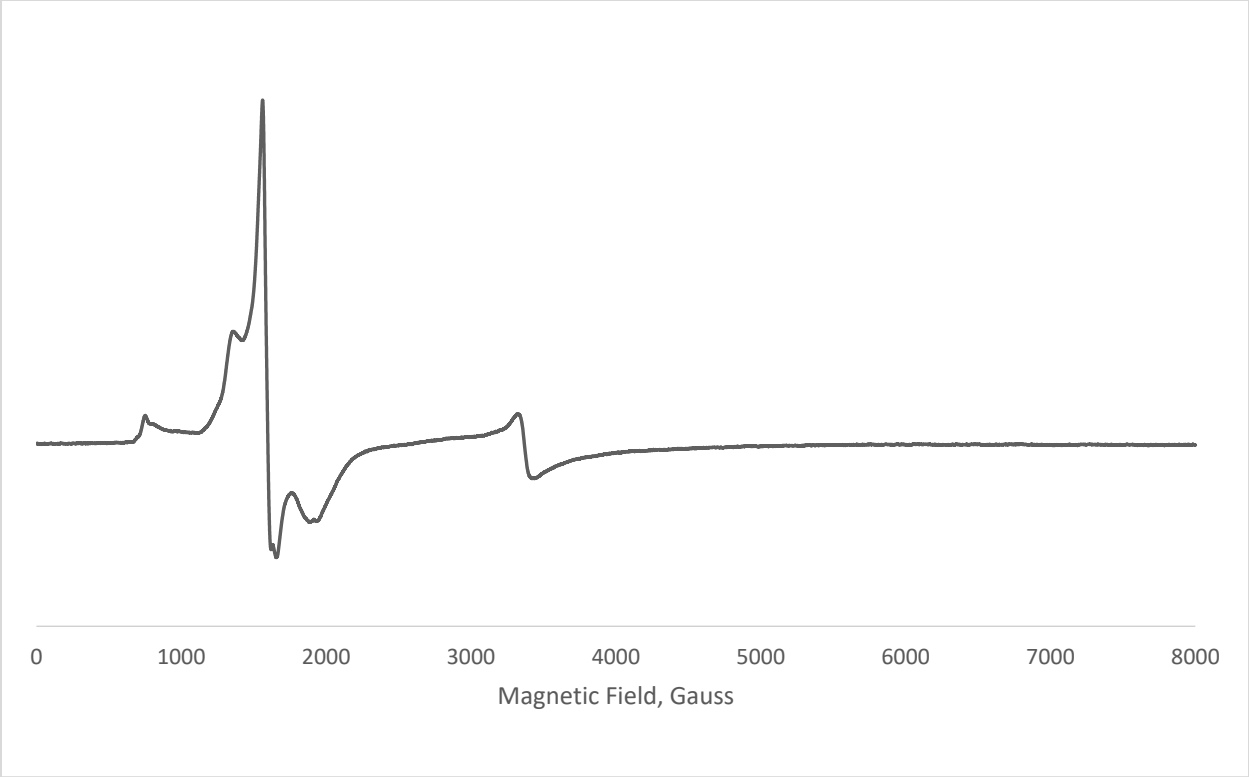

Figure S45. $FeCl_3$ + 2-picolinic acid (1:1 molar ratio) in pyridine-H_2O.

Upon the addition of NPr_3 to this solution, all of the iron was converted to low spin (S = ½) Fe(III) indicated by a very broad ($\Delta Hpp \approx 900$ G) signal at g = 2 (Figure S46). This indicates that NPr_3 binds to the Fe(III) converting it to low-spin Fe(III). This result supports the result from the IR titration described on page 42 in the section titled Reaction of NPr3 with FeCl3·6H2O/2-Picolinic Acid (1:1) in Pyridine.

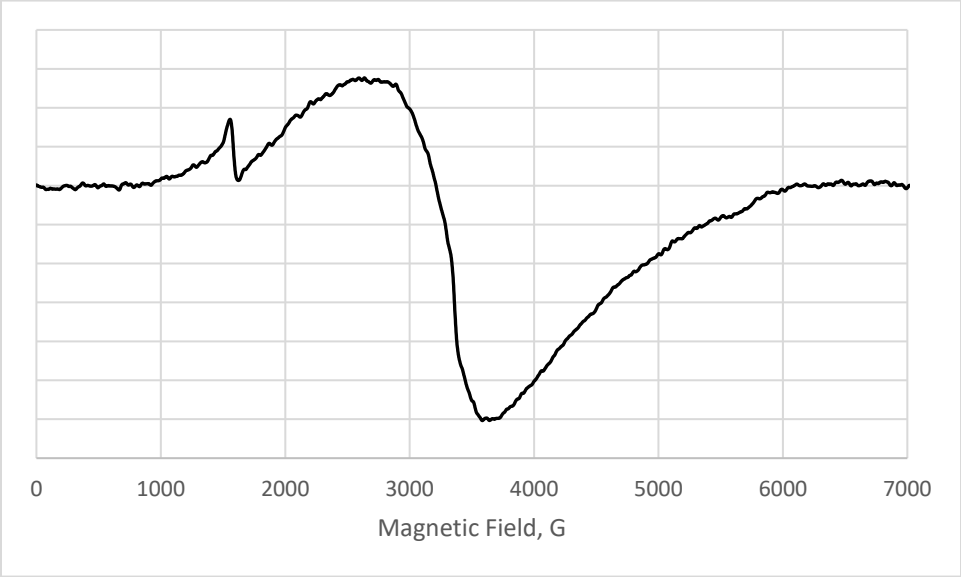

Figure S46. $FeCl_3$ + 2-picolinic acid + NPr_3 (1:1:1 molar equiv) in water/pyridine (150:4 /v) frozen solution.

EPR spectra of the mixture after addition of the oxidant, $PhCO_3{}^tBu$, to this solution resulted in a solution that had no metal- or radical-based EPR signal (except for a small amount of the g=4.3 peak, indicating an EPR-silent species is formed. This could be an Fe(IV) or a spin-coupled dimeric or polymeric Fe(III) species. However, the first order dependence on [Fe/2-picolinic acid] as established by initial rate kinetics suggests a monomeric Fe species as the catalyst species – suggesting that the EPR-silent species is indeed the active catalyst in an oxidation state +IV.

In contrast, using ^{t}BuOOH instead of $PhCO_3{}^tBu$ gave a very large free radical signal and a mixture of high- and low- spin Fe(III) (data not shown). As no amide product is formed under analogous, catalytic conditions, this suggests that the mixture obtained with tBuOOH is irrelevant for catalytic turnover.

Examining Product Inhibition via Kinetic Profile Analysis

By analogy with the general procedure for method of initial rates, $FeCl_3 \cdot 6H_2O$ (34 mg, 125 μmol, 5.0 mol %), picolinic acid (15 mg, 125 μmol, 5.0 mol %), pyridine (15 mL) and then deionized H_2O (406 μL, 406 mg, 22.5 mmol, 9 eq.) were added to a 20 mL scintillation vial equipped with a microstirbar. The reaction mixture was heated to 50 °C on a pre-heated vial plate and vigorously stirred (1500 rpm). The ReactIR15 probe (see Materials and Methods) was inserted into the reaction vial and IR analysis was initiated. Subsequently, preheated $PhCO_3{}^tBu$ (1.4 mL, 1.5 g, 7.5 mmol) and then NPr_3 (476 μL, 358 mg, 2.5 mmol) were added to the reaction. Once the maximum slope of the reaction was reached, $HNPr_2$ (171 μL, 126 mg, 1.25 mmol, 50 mol %), H_2NPr (103 μL, 74 mg, 1.25 mmol, 50 mol %) and *N*,*N*-dipropylpropanamide (182 μL, 196 mg, 1.25 mmol, 50 mol %) were added, as indicated by the red arrow in Figure S47.

IR analysis was conducted to generate the kinetic traces shown below (Figure S47). $-k_{obs}$ $[PhCO_3{}^tBu]$ was determined by determining the maximum slope of the reaction trace after the initiation period (red). Inhibition by side products would results by a significantly changed rate (slope) of the reaction as determined by measuring the slope before and after the addition of side products, within the range of maximum slope used to determine $-k_{obs}$. However, no change in slope and therefore, no product inhibition was observed with $HNPr_2$, H_2NPr, or $EtC(=O)NPr_2$.

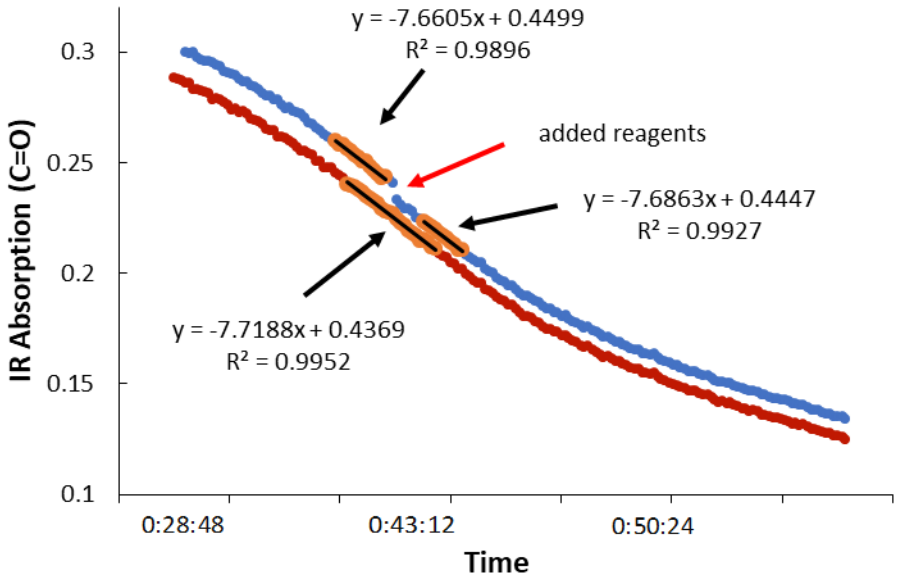

Figure S47. Decrease of $[PhCO_3{}^tBu]$ versus Time for standard reaction conditions (red) and upon addition of side products (blue).

GCMS Spectrum of Reaction Mixture from NPr_3 C_α-H Oxidation Reaction with 5 mol % ^{t}BuOOH added.

By analogy with the general procedure for method of initial rates, $FeCl_3 \cdot 6H_2O$ (34 mg, 125 μmol, 5.0 mol %), picolinic acid (15 mg, 125 μmol, 5.0 mol %), pyridine (15 mL), ^{t}BuOOH (70% in H_2O; 17 μL, 16 mg, 125 μmol, 5.0 mol %) and then deionized H_2O (406 μL, 406 mg, 22.5 mmol, 9 eq.) were added to a 20 mL scintillation vial equipped with a microstirbar. Subsequently, $PhCO_3{}^tBu$ (1.4 mL, 1.5 g, 7.5 mmol) and then NPr_3 (476 μL, 358 mg, 2.5 mmol) were added to the reaction. The reaction mixture was heated to 50 °C on a pre-heated vial plate and vigorously stirred (1500 rpm) for 12 h.

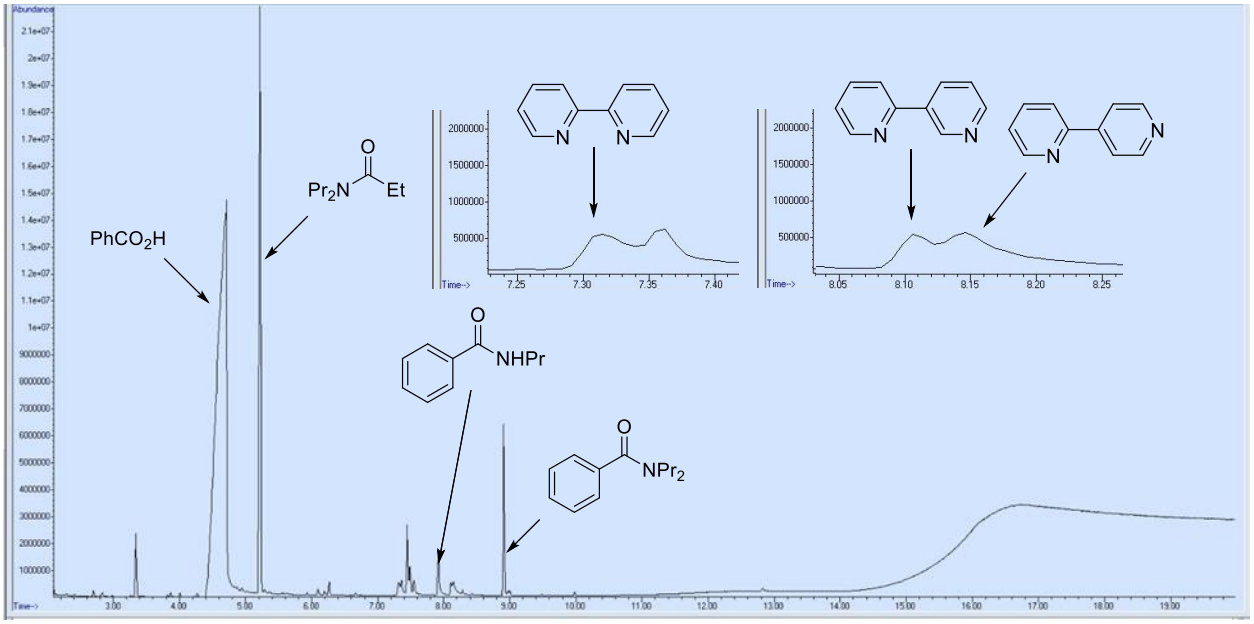

Figure S48. GCMS Chromatogram and Peak Assignments for Crude Tri(*n*-propyl)amine Oxidation Mixture.

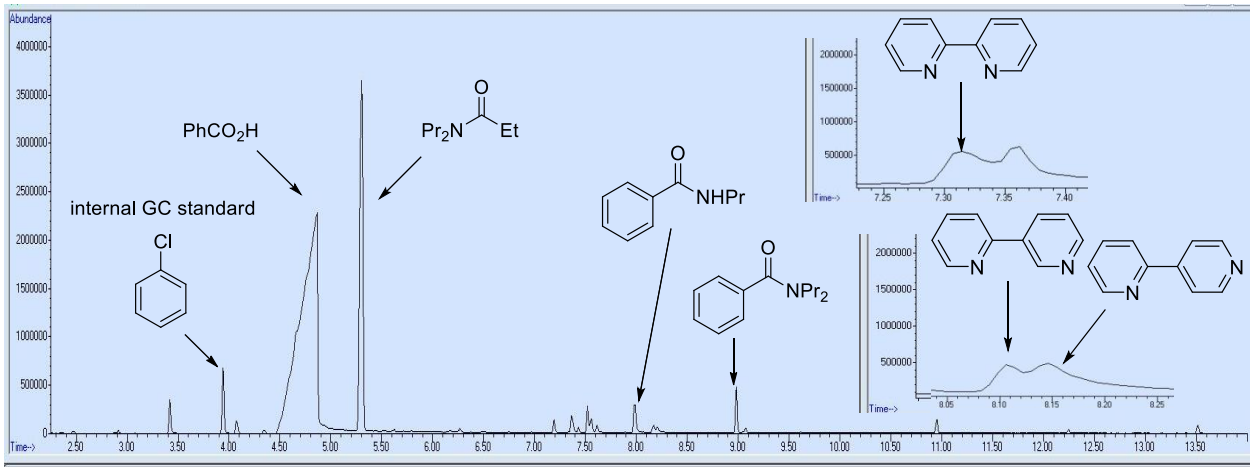

Figure S49. GCMS Chromatogram and Peak Assignments for Crude Tri(*n*-propyl)amine Oxidation Mixture with 5 mol % ^{t}BuOOH initially added.

References

(1) Hedaya, E.; Winstein, S. *J. Am. Chem. Soc.* **1967**, *1*, 89.

(2) Legacy, C. J.; Wang, A.; O'Day, B. J.; Emmert, M. H., Iron-Catalyzed Cα-H Oxidation of Tertiary, Aliphatic Amines to Amides under Mild Conditions. *Angew. Chem. Int. Ed.* **2015,** 54 (49), 14907-14910.

(3) Hansch, C.; Leo, A.; Taft, R. W. *Chem. Rev.* **1991**, *91*, 165.

(4) Merritt, M. V.; Johnson, R. A. *J. Am. Chem. Soc.* 1977, *99*, 3713.

(5) Howard, J. A.; Tate, J. C. *Can. J. Chem.* **1978**, *56*, 176.

Initial Rate Kinetics
Eyring Studies
Kinetic Isotope Effect
Hammett Study
Reaction Profile Kinetics
Oxidant Probe Study
EPR Studies

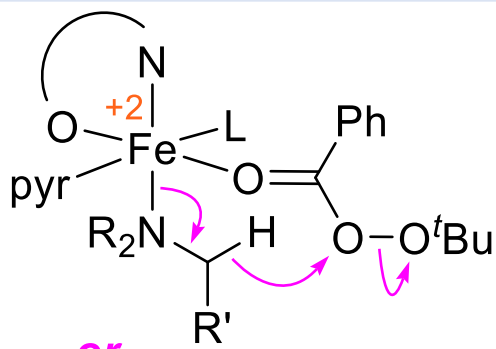

or